Experimental Study of a Tip Leakage Flow

Giovanni Caputi - Gennaro

University Roma Tre

Dissertation submitted to the Faculty of Engineering
in fulfillment of the requirements for the degree
of

Doctor of Philosophy
In
Mechanical Engineering

Roberto Camussi

Luigi Morino

Non ha l'ottimo artista alcun concetto
Che un marmo solo in se' non circoscriva col superchio.
E solo a quello arriva
la man ch'obbedisce a l'intelletto.

Michelangelo Buonarroti

Abstract

Experimental acoustic characterization of a tip leakage flow developing downstream of a single blade test rig has been performed via wavelet–based post–processing techniques. Hot–Wire Anemometer, far–field and wall–pressure signals were processed which have been measured on an instrumented airfoil installed within the anechoic wind tunnel available at the Laboratory of Fluid Mechanics and Acoustics of the Ecole Centrale de Lyon. The adopted airfoil is a NACA 5510 airfoil and the test rig has adjustable tip gap, which allows for tuning of the gap width: two flow configurations, with and without gap at the airfoil tip, are investigated. The Reynolds number, based on the airfoil chord, was $Re_c \sim 9.3 \cdot 10^5$.

In the experimental campaign, conducted by researchers of the Ecole Centrale de Lyon, measurements of the pressure both on the airfoil surface and in the acoustic field have been coupled with HWA and PIV acquisitions. The outcoming database provided a suitable characterization of the (strong unsteady) flow dynamics in the tip–gap region as well as the impact of the tip–gap turbulent interaction on to the measured acoustic emission.

In the present research activity, advanced post–processing procedures based on the wavelet transform are applied to the data measured by ECL in order to extract the most energetic non–periodic contributions, localized in time and in space, and to detect the fluid dynamic structures which may act as noise sources. The events tracking method is based on the computation of the time–frequency maps from which it is possible to select events, determine their time of appearance, and perform conditional averages.

The conditioning procedure has shown that the gap width plays a fundamental role in the noise generation mechanisms: the amplitude of the oscillations in the averaged wall–pressure signatures becomes larger for increasing width of the gap,

probably as an effect of a roll–up phenomenon occurring at the tip edge of the airfoil. This phenomenon is known to produce complex unsteady interactions within the flow. Arising turbulent mechanisms dominate the flow behaviour not only in the gap region. Vortex structures shed by the tip leakage flow convect downstream, interact with the trailing edge flow and strongly modify the flow dynamics and the scattering mechanisms.

Wavelet–conditioned HWA signals confirmed this features, as the averaged velocity fluctuations in the trailing edge region seem to be significantly affected by the gap width and statistically related to strong pressure energy fluctuations detected over the airfoil suction side close to the gap.

The pressure–velocity cross–analysis here presented evidenced the effectiveness of the tip leakage flow as a noise source and provided useful information about the turbulent mechanisms excited by its formation. Pressure/velocity wavelet–based correlation obtained by processing HWA/far–field pressure and PIV/far–field pressure measurements yielded, in a statistic sense, the location of the major fluid dynamic structure which may be related to the largest pressure fluctuations at the wall and in the far field.

A further step in the present research activity, has been the implementation of a boundary–to–field transfer function approach, as an attempt to model the acoustic phenomenon under investigation. The approach is based upon a theoretical formulation which uses the well-known concept of transpiration velocity and is devoted to the vorticity generated sound problem. Preliminary results were obtained by using this approach in a simple test–case, but the application to the configuration here analyzed is one of the future steps in the ongoing research activity.

Contents

List of Tables

List of Figures

Chapter 1

Introduction

1.1 The tip leakage flow and its influence on noise generation

Driven by environmental concern for noise exposure to airport community, noise reduction evidently becomes a priority of aircraft engine design. Owing to recent progress in turbomachinery noise reduction technologies, fan noise has become the major noise source for subsonic aircraft engines, and in many situations, as for take–off and landing flight sequences, the dominant noise sources overall are by–products of random and periodic gusts interacting with solid surfaces in the fan rig: periodic impinging of upstream disturbances and associated turbulences are a source of tonal and broadband noise respectively. The contribution of broadband noise to the overall noise level is certain, especially during the landing phase where it accounts for as much as 50% (see also Fig. 1.1). Among other broadband noise sources, rotor self noise is composed of two major components, the noise generated when the blade boundary layer disturbances interact with the trailing edge and the noise generated by the tip leakage flow interacting with the geometrical singularities of the blade tip. Whereas the physics of noise production at the trailing edge are nowadays quite well understood (see e.g. Rozenberg *et al.*, 2007), the tip leakage

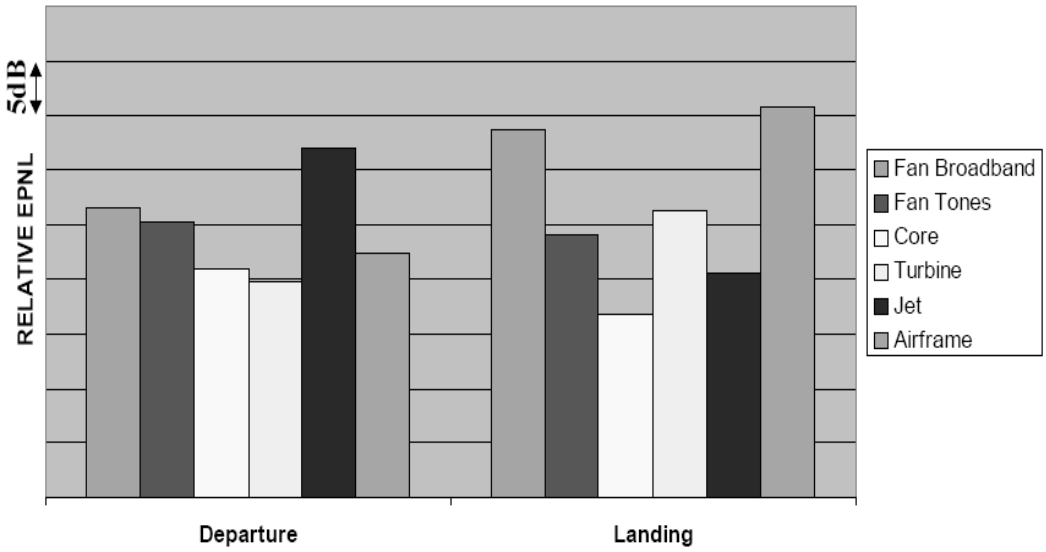

Figure 1.1: Noise component breakdown for modern aircraft.

area is a region where broadband noise sources are suspected but remain difficult to identify and quantify.

The tip clearance flow field is an extremely complex three-dimensional unsteady viscous flow phenomenon. It has been found (see e.g. Bindon, 1989; Storer & Cumpsty, 1991) that a high speed jet–like flow through the gap arises from the relative motion of the blade tip and the end–wall and from the pressure difference across the blade tip. This flow, shed to the adjacent blade passage, eventually rolls up, forming a vortex–like structure that convects downstream (Fig. 1.2). The resulting unsteady tip leakage vortex is a dominant feature on the flow field near the rotor blade tip region.

Known for its influence to aerodynamic efficiency, noise/vibration generation and even structure deterioration in the turbomachines, the tip leakage vortex and its unsteady characteristics has been carefully studied for over 50 years. To acquire a better understanding in the physics of the tip leakage vortex, many aerodynamic studies have successfully revealed the principles of its formation and flow structure. Noteworthy the recent experimental tests conducted by Intratep (2006); Muthanna

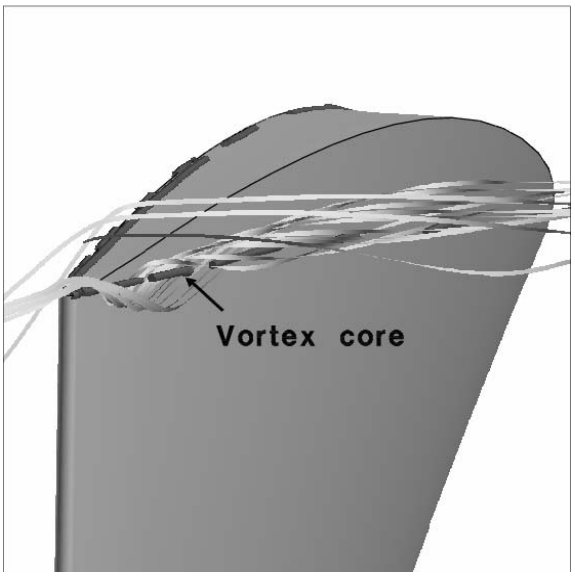

Figure 1.2: Fan tip clearance flow sketch.

(1998); Saha (1999); Tang (2004), which documented the influence of different parameters onto the structures of the tip clearance gap flow in compressor cascades. Nevertheless, few efforts have concentrated on the problem related to the associated broadband noise–generation mechanisms.

Until recent years, tip clearance noise was not very well documented in literature and besides the work of Dunne & Howe (1997), modeling efforts remained quite sparse for this difficult problem. There have been some studies about the magnitude of tip clearance noise in rotating rigs (Fukano & Jang, 2004; Fukano & Takamatsu, 1986) and some even tlacked to problem of tip flow control (Khourrami & Choudari, 2001; Corsini *et al.*, 2005). The careful study of Ganz *et al.* (1998) provides indications that the rotor blade tip interaction with the inlet boundary layer turbulence is a significant source of noise and is strongly affected by rotor tip clearance. However their study also illustrated that it is quite difficult to separate the various phenomena occurring in the blade tip region in a representative fan rig: wall boundary layer interaction with the blade tip, tip clearance flow, rotor tip wake/stator interactions. Because of the extremely complicated nature of these

mechanisms, understanding of their interaction in the tip leakage flow and their contribution to external noise level remains a challenging task for many researchers.

Experimental investigations conducted by Ma (2003) on a linear cascade configuration show that, although large periodic fluctuations occur in the tip leakage flow downstream of the cascade, larger aperiodic components contain most of the turbulence energy. Two point correlation measurements and linear stochastic estimation method were used to educe the structure of this aperiodic part: the velocity field associated with single point aperiodic velocity fluctuations has been found to consist of organized coherent structures in large scale. The presence of such coherent structures makes the estimated instantaneous velocity field significantly different from the phase averaged periodic flow. The intermittent fluctuations are so intense in the tip leakage vortex region that the phase averaged flow features are completely submerged by the aperiodic component. Microphone measurements also show that pressure mean square fluctuations downstream of the cascade are consistent with the behaviour of the velocity fluctuations, but the effectiveness of the identified coherent structures as acoustic sources was not investigated. By the way, intense velocity and vorticity non–periodic fluctuations with respect to both time and space exist in the tip leakage vortex region. As explained in Powell (1964) and Kambe (1986), acoustic radiations are directly related to temporal vorticity variations. Therefore, these so–called intermittent structures might be efficient acoustic sources and their effectiveness is presently explored by proper simultaneous velocity/pressure measurements.

1.2 Current research motivation and approach

This work has been funded by the European Community as part of the 6th Framework Project PROBAND n° AST4–CT–2005–012222. As mentioned above, in many attempts to address the question of tip clearance noise, difficulties arise from the fact that it could not clearly be distinguished among other noise sources in

a representative fan rig. In the present study, the problem has been simplified: an experimental investigation has been conducted on a single NACA 5510 airfoil installed within the anechoic wind tunnel available at the Laboratory of Fluid Mechanics and Acoustics of the Ecole Centrale de Lyon. Unlike the aforementioned cascade experiments, no relative motion between the airfoil and the tip–facing wall was achieved, since the airfoil was mounted between two horizontal plates. However, a significant clearance flow was obtained by selecting a highly cambered airfoil and loading it. The side flow remains free, which allows to carrying out far field sound measurements outside of the flow in the medium at rest (Jacob *et al.*, 2007). The advantage of this experimental approach consists of discarding periodic behaviour which is intrinsic in a typical turbomachinery working condition toghether with the tonal contribution to the overall noise level, while turbulence–acoustic interaction mechanisms which are responsible for the broadband noise generation are consequently isolated. A coupled acoustic and fluid dynamic characterization of the physical mechanisms involved in such configuration has been achieved by means of PIV, cross–HWA, LDA, and both steady and unsteady pressure measurements.

The main task of the present research activity is the analysis of the correlation between the dynamics of the unsteady intermittent structures forming in a tip leakage flow of a single airfoil and both wall–pressure fluctuations and acoustic emission. As mentioned above, intermittency is related to the presence of rare but strong velocity gradients, that are generated by highly coherent structures (see e.g. She *et al.*, 1991; Benzi *et al.*, 1993; Douady *et al.*, 1991). Owing to the intermittent nature and to the singular shape of such structures, wavelet transform decomposition appears an optimal tool for their eduction.

During the last decades, wavelet analysis has been extensively used to analyze random data obtained from both numerical simulations and experimental investigations conducted in turbulent flows. Comprehensive reviews about the wavelet theory and their applications can be found in many reference papers or books (e.g. see among many Mallat, 1989; Farge, 1992). Conditional sampling techniques

based on the wavelet transform have been applied to turbulence data (Camussi & Guj, 1997) and to pressure/velocity measurements (Guj *et al.*, 2003) in order to extract the most energetic contributions of the original signals.

In the present work, a convenient wavelet–based post–processing technique is applied to experimental data permitting us to extract the most energetic non–periodic contributions to the pressure fluctuations, localized in time and in space and hidden in the original chaotic signals.

Peaks in the far–field noise and wall–pressure are then used as a trigger to perform a conditional statistics of both pressure and velocity data delivered by the experimental campaign, in order to recover the most probable shape of the most energetic pressure events and to obtain a statistical correlation between the flow dynamics (described by either single probe hot–wire anemometer and PIV measurements) and the largest wall–pressure and acoustic–pressure fluctuations (extracted from the wavelet treatment of single point pressure signals).

In addition, the technique allows tracking of the phase of both the pressure events and the corresponding noise–producing structures. In this way, it is possible to analyze their temporal statistics by computing the probability distribution functions (PDF) of the time delay between successive conditional samples. As shown in several previous works (Abry *et al.*, 1994; Camussi & Verzicco, 2000), this is a powerful tool for determining whether the educed events have an intermittent character. Indeed, if the events generating noise are intermittent in time and uncorrelated with each other, strongly non–Gaussian PDFs with exponential–like distributions are expected.

Once the major noise–producing structures are identified and characterized, the acoustic phenomena involved in the investigated problem may be modeled by means of a transpiration–velocity power–spectral–density approach. This would allow to retrieve the acoustic power spectra related to the fluid dynamic structures educed by the wavelet conditioning.

1.3 Dissertation layout

This dissertation reports many of the experiments performed to document the acoustic and fluid dynamic phenomena under investigation. The experimental campaign was conceived to achieve a deeper understanding of the complex mechanisms responsible for broadband fan noise contribution imputable to the tip leakage flow formation.

Chapter 2 provides a description of the facility, apparatus and techniques used in this study. The main features of the LMFA high–speed wind tunnel, the experimental set–up, the pressure and velocity measurements techniques, and the investigated flow conditions are described. Details on the experimental test rig may be found in (details in Jacob *et al.*, 2007).

In Chapter 3 the wavelet technique is outlined toghether with some basic features of the wavelet analysis and the main differences with respct to the standard Fourier transform. In addition the concept of LIM is addressed in order to provide the reader the full potential of a wavelet–based analysis in detecting sharp variation in the processed signal

Chapter 4 deals with the wavelet–based technique here adopted for tracking events. Conditional averaging procedure based on this technique is described both for auto–conditioning and cross–conditioning purpose, the latter showing how possible physical correlation between two intermittent phenomena may be evidenced.

Results pertaining the aerodynamic and acoustic characterization of the tip leakage flow are discussed in Chapter 5. Turbulent intermittent typical phenomena are detected in terms of pressure and velocity average fluctuations. The gap influence on to the fluid dynamics and noise generation mechanisms is addressed and physical interpretation of the outcomes is proposed both for acoustics and fluid dynamics topics.

Chapter 6, the final chapter, summarizes the outcomes of the whole research activity and concludes the dissertation.

Finally, a boundary–to–field formulation has been implemented as an attempt to model the acoustic phenomenon under investigation. The theoretical and numerical formulation, as described in Caputi–Gennaro *et al.* (2006), is reported in Appendix A.

Chapter 2

Experimental set–up

2.1 Flow set–up

The experiment was carried out in the anechoic room (10 m $\times$ 8 m $\times$ 8 m) of the Laboratoire de Mécanique des Fluides et d'Acoustique (LMFA), a joint CNRS–ECL–UCBLyon–I laboratory located at the Ecole Centrale de Lyon. The airflow is guided 2.5 m into the room by a square 0.56×0.56 m^2 and 2 m long duct with a 7.5° angle with respect to the room inlet–outlet axis. The purpose of this flow duct is to allow for upstream propagation and to compensate flow deviations due to the airfoil (that might damage the anechoic coating of the room). Air was supplied by a high–speed subsonic anechoic wind tunnel with a 0.45×0.20 m^2 rectangular nozzle at Mach numbers ranging up to 0.3. For practical reasons however (mechanical forces onto the airfoil support, vibrations, etc.) and for numerical reasons (chord–based Reynolds number $Re_c < 10^6$), the Mach number was maintained below 0.27 and the main (or reference) configuration was at $M_0 \sim 0.2$. The jet is flanged by two horizontal plates on the upper and lower side of the jet. An initial gap between each of the plates and the nozzle lip provides a passive suction device that allows to tuning the boundary layer thickness.

The experimental set–up is shown in Figure 2.1. A NACA 5510 profile with a

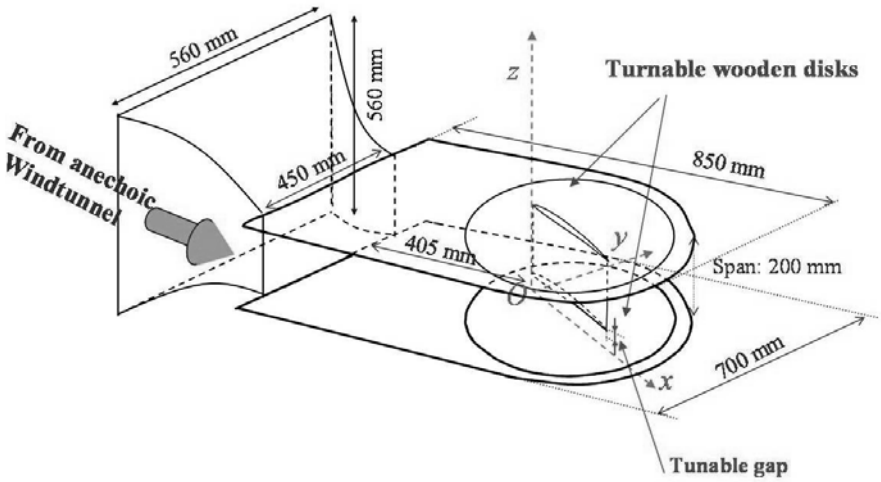

Figure 2.1: Sketch of the experimental set–up.

200 mm chord and 200 mm span is placed in the potential core region of the jet, between the two horizontal plates (Fig. 2.2). The airfoil is mounted onto a turnable wooden disk attached to the upper plate, which allows to tuning the angle of attack. Another disk is mounted onto the lower plate. Two disk have been designed: one contains a square glass window for PIV and LDV measurements, whereas the other is equipped with remote microphone probes and a flush mounted microphone for wall–pressure measurements in the gap region. The disk allows to rotating the measurement devices independently of the airfoil. The gap is also adjustable, the total height (gap + span) remaining equal to 200 mm.

2.2 Airfoil and reference configurations

The airfoil is a NACA 5510 wing (chord $c = 200$ mm; span $l = 200$ mm; thickness $e = 20$ mm; 5 % camber). It is located $\sim$ 1.5 chords downstream of the jet nozzle. There are two reference configurations: for both of them the geometrical angle of attack is $\alpha = 15°$, the flow is uniform within 0.6 %, its speed at the nozzle outlet is $U_0 = 70$ m/s, the turbulence level is $u'/U_0 \sim 0.7$ %, and the

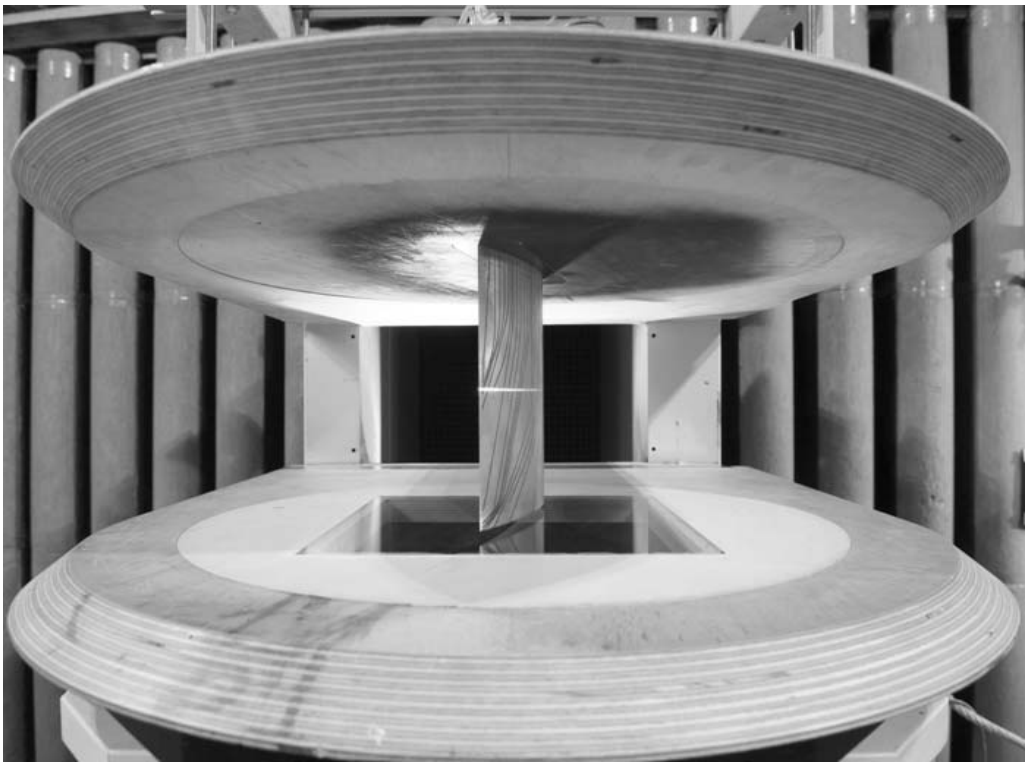

Figure 2.2: Tip clearance configuration.

Airfoil		NACA 5510
Chord c	[mm]	200
Span l	[mm]	200
Distance from nozzle	[mm]	300
Gap h	[mm]	0, 10
Angle of attack α	[deg]	15
Inflow velocity U_0	[m/s]	70
Turbulence level u'/U_0		0.7%
BL 99% thickness δ	[mm]	~ 18
BL displacement thickness δ^*	[mm]	~ 1.4
Ambient pressure	[kPa]	98.7
Ambient temperature	[K]	293

Table 2.1: Parameters of the reference configurations

Reynolds number based on the chord is $Re_c \sim 9.3 \cdot 10^5$. Moreover, the initial plate–to–nozzle gap (governing the passive boundary layer suction device) is common for all measurements resulting in a $\delta \sim 18$ mm thickness half a chord upstream of the airfoil that corresponds to $\delta^* \sim 1.4$ mm displacement thickness; the two configurations only differ by the size of the gap, one having an $h = 10$ mm gap, the other having no gap at all. Unless mentioned otherwise, the former will be referred to as "reference gap configuration" or "reference configuration with gap", whereas the latter will be the "no–gap reference configuration". The various parameters of the reference configurations are summarized in Table 2.1.

Since the two end plates and the airfoil remain motionless, the gap flow is only induced by the high camber (5 %) and angle of attack ($\alpha = 15°$). This results in a high load and a subsequently significant gap flow.

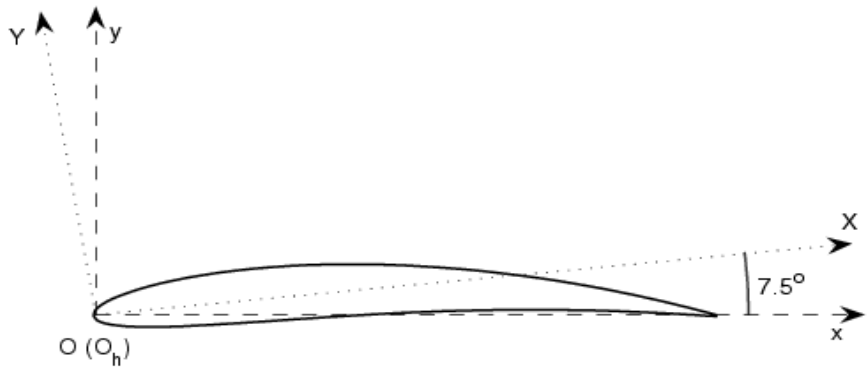

Figure 2.3: Co–ordinate systems.

2.3 Co–ordinates

Two different coordinate systems are used to evaluate the position of any point in the flow (see Figures 2.1 and 2.3). The first one is linked to the inflow, the projection of the airfoil's leading edge on the lower plate being the origin O: the X axis is aligned with the jet axis, i.e. the main inflow direction, and oriented from the wind tunnel's exit to the airfoil; the Z axis follows the span–wise direction from the gap to the upper plate; the cross–stream Y axis is defined such that the coordinate system is direct (from right to left, looking downstream). This coordinate system is well suited for describing the incident flow. The second coordinate system is bound to the profile, and is particularly useful to locate the wall pressure probes. The origin O_g is located at the tip of the leading edge: the x axis is following the aerodynamic chord pointing from the leading edge to the trailing edge; the z axis is the same as the above introduced Z axis, the coordinate z being shifted by one gap height $z = Z - h$, and the y axis is normal to the chord, pointing from the pressure to the suction side.

2.4 Investigated parameters

From the reference configurations cited above, various parameters have been varied within a range of values during the measurement campaigns. They are summarized in Table 2.2. The flow speed, the gap width, and the angle of attack are varied from 20 to 90 m/s, 0 to 10 mm, and 0° to 18° respectively during the experiment. Note that not all parameter values have been investigated with each measurement technique or measurement set–up. The atmospheric pressure was 98.7 ± 0.8 kPa. The ambient temperature is 296 ± 6 K. In these conditions, the chord–based Reynolds number is $Re_c \sim 9.3 \cdot 10^5$ in the two reference configurations and the corresponding Mach number is $M_0 \sim 0.2$.

2.5 Measurements

Measurements undertaken during the experimental campaign are:

- PIV in the (X, Y)–planes, around the airfoil and in the gap region;
- HWA profiles in the (X, Y)–planes (except for one lower plate boundary layer profile);
- LDA profiles in the (X, Y)–planes at fixed chord–wise locations;
- Aerodynamic static pressure on the airfoil;
- Aerodynamic unsteady pressure (including time series, spectra, and coherence) on the airfoil surface and on the lower plate;
- Acoustic pressure in the far field (including time series, spectra, and directivity).

Most pressure spectra and coherence measurements are obtained with a sampling frequency of 64 kHz that is an effective frequency range of 25 kHz ($1/2.56^{\text{th}}$ of

PIV measurement parameters

U_0	[m/s]	$40, 70, 90$
α	[deg]	$5, 10, 15, 18$
h	[mm]	$0, 3, 5, 7, 10, 15$
Z	[mm]	$3, 5, 7, 9.5, 12, 15, 20, 50, 100, 150$

HWA measurement parameters

U_0	[m/s]	$40, 70, 90$
α	[deg]	$10, 15$
h	[mm]	$0, 10$
Z	[mm]	$5, 10, 100$

Pressure measurement parameters

U_0	[m/s]	$20, 30, 40, 50, 60, 70, 80, 90$
α	[deg]	$0, 5, 10, 15, 18$
h	[mm]	$0, 1, 2, 3, 5, 10$

Acoustic measurement parameters

U_0	[m/s]	$20, 30, 40, 50, 60, 70, 80, 90$
α	[deg]	$0, 5, 10, 15, 18$
h	[mm]	$0, 1, 2, 3, 5, 10$
R	[m]	1^a, 1.5^b, 1.7

[a] with wall–pressure and single HWA
[b] with PIV, LDA

Table 2.2: Aerodynamic and acoustic measurement parameters

the sampling frequency). The frequency resolution is 7.8125 Hz (with 8192 points per FFT). The results are computed by averaging 500 FFT's unless mentioned otherwise. HWA spectra are obtained at a 45 kHz to 64 kHz sampling rate. Additionally, a 10 kHz sample is stored at each mean velocity measurement point. LDA spectra are obtained at variable sampling rates: typically 8–12 kHz but lower for some measurements.

Some joint pressure–velocity measurements have been also carried out:

- joint pressure–single HWA;
- joint pressure–LDA;
- joint pressure–PIV.

Unsteady pressure measurements on the airfoil, both in the mid–span region and in the tip edge region were combined with far–field and single probe HWA measurements.

In addition, simultaneous PIV and single point pressure measurements were carried out both around the airfoil and in the gap region. Of particular interest here are the PIV–pressure data measured on the reference gap configuration. In this case, the measurement plane was located in the mid–gap plane (5 mm away from the tip edge of the airfoil) and the laser source was placed on the pressure side. Two near field pressure probes were placed on the airfoil tip face, along the mid line of the profile at 6 mm and 155 mm far from the leading edge. A third pressure probe was placed in the far field (see Table 2.2), on the suction side in the mid–span plane. The measurements were divided into 10 acquisition series. During each acquisition, 60 PIV snapshots were taken at a frequency of 1 Hz (which means 60 s per acquisition), while the pressure signals were sampled at 20 kHz. This yield a total of 600 PIV snapshots and 10 pressure time series resulting from the experimental measurements.

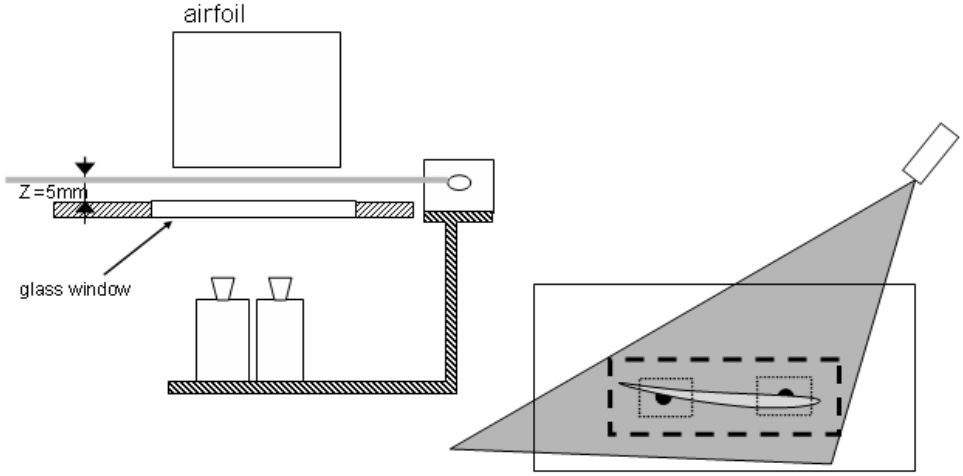

Figure 2.4: Sketch of the PIV experimental set–up.

2.5.1 PIV measurements

A *LaVision* system is used with two CCD cameras and controlled by the *LaVision*'s software *Davis*. A LASER sheet is generated in a plane parallel to the lower plate (that is, at fixed z or Z position) via two LASER Yag cavities which are mounted onto a common support and coupled by a cylindrical lens. The two cavities emit successive light pulses which are directed onto a same plane measurement region. A view of the LASER sheet is shown on Figure 2.4. The two cameras are placed beneath the lower plate which is equipped with a glass window. The cameras are located next to each other in order to provide pictures from the whole airfoil with a good resolution.

As sketched on Fig. 2.4, the LASER and the cameras are fitted on a common support that can be moved up and down: thus measurements at any span–wise position (Z coordinate) can be performed without tuning the LASER–camera system. The measurement area is a rectangle of 250×105 mm^2 having an angle of $6.2°$ with the (O, X) direction. Each camera has a 1280×1024 pixels resolution, and the velocity fields are computed using a 32×32 pixels interrogation window

that corresponds to a 1.5×1.6 mm^2 area in the image with 50% overlap. Since the flow is highly 3D in the gap region, the delay between 2 images is kept very short (between 5 and 15 μs in the gap region and up to 40 μs in quieter flow regions like the mid–span plane) to keep track of as many particles as possible. The seeding material is obtained from heated paraffin oil that is injected upstream of the wind–tunnel fan.

In the present case, a shadow zone due to the airfoil appears in planes that are above the gap. Therefore, in order to reach the pressure and the suction side with the LASER sheet in planes located at $Z > h$, the LASER source has to be placed successively on each side of the airfoil, slightly upstream of the airfoil for the pressure side measurements and slightly downstream of the airfoil for the suction side measurements. Thus, no shadow region from the airfoil remains and a complete flow picture around the airfoil can be reconstructed. However, since the resulting PIV fields are obtained from different measurements, the pressure and suction side fields can not be correlated.

2.5.2 LDA measurements

The LDA measurements are carried out with a *Dantec* dual–beam, backscatter Laser Doppler Anemometer (LDA) system. Two pairs of beams are used for two–dimensional velocity measurements. They are supplied by the green line (515 nm) and the blue line (488 nm) of a Spectra Physics 4 W argon–ion Laser source. The beams of each pair undergo a relative frequency shift of 40 MHz in a Bragg cell. The four beams are guided to the flow with an optical fiber which is terminated by a focusing lens with a focal length of 250 mm for the gap region and 400 mm for the mid–span plane. The beams of each pair have a mutual angle of 9°. For a measurement of the stream–wise and cross–stream velocity components, each Laser beam makes a 4.5° angle with the z–direction in the plane of the corresponding velocity component. The same window as for PIV measurements is used. A photo of the set–up is shown on Figure 2.5. In the gap region (resp. in the mid–span

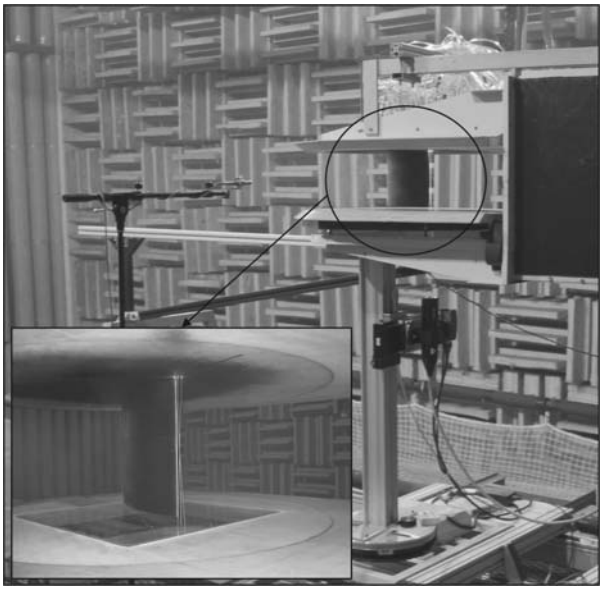

Figure 2.5: Photo of the LDV experimental set–up.

plane) the size of the measurement volume (spatial resolution) is about 70–75 μm (resp. 110–120 μm), whereas its length in the span–wise direction is 0.9 mm (resp. 2.3–2.5 mm). The fringe spacing is about 3 μm (resp. 5.0–5.3 μm). The backscatter beams are focused by the same lens and sent through an optical fiber onto photomultipliers. The signals are then treated by two *Dantec* real–time signal analyzers and post–processed on a personal computer. The seeding material is the same used for the PIV measurements. LDA measurements are carried out in the same regions as the PIV measurements for the reference configurations, that is, around the airfoil at mid–span and in the gap region. They provide a useful validation of the PIV measurements as well as spectral informations.

2.5.3 Hot–wire measurements

The hot–wire measurements are performed using a *Dantec* anemometer with a *Dantec* 55P51 cross–wire. The signals are recorded with a 10 kHz sampling frequency for mean flow and rms measurements and 45 kHz frequency for velocity

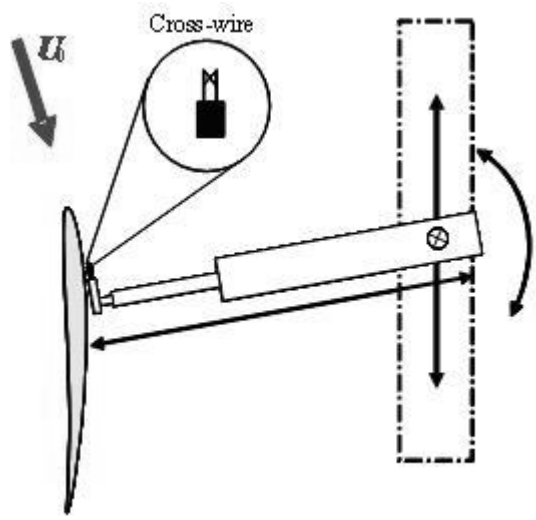

Figure 2.6: Sketch of the HWA experimental set–up.

spectra. The probe support is mounted onto a system that allows moving the probe normal to the airfoil or the flow at any stream–wise location (see Fig. 2.6). The cross–wires measure the velocity components in the (X, Y) plane at any span–wise position.

The purpose of the HWA–measurements is to characterize the oncoming flow, the far wake and the outflow (not covered by the PIV measurements), to measure velocity spectra at given points, and to provide comparison points for the PIV in the vicinity of the airfoil. Thus, measurements are carried out upstream and downstream of the airfoil as well as around it. Additional measurements are taken near the gap region. A vertical profile is measured half a chord upstream in order to characterize the oncoming boundary layer.

2.5.4 Mean and unsteady wall pressure measurements

Steady and fluctuating wall pressure is measured in several points of the airfoil's surface and the lower plate. Probes are placed on the airfoil mainly at two z–locations: the mid–span plane ($z = 100$ mm $= l/2$) and above the airfoil tip–edge

($z = 1$ mm). Additional probes are placed in the span–wise direction at the trailing edge in order to get correlation length data, and under the airfoil tip in the gap region. Other probes are placed on the lower plate around and in the gap area. Figure 2.7 gives a qualitative overview of the unsteady pressure probe locations. A specific technique is used to mount the microphones on the airfoil (see Figure 2.8). Little pinholes ($\varnothing = 0.5$ mm) are manufactured at the measurement locations and connected to capillary tubes into which the microphones are flush–mounted at a remote position outside of the airfoil as described in Roger & Perennes (1998). Outside of the airfoil, the rigid tubes open into 3 m long flexible tubes which act as anechoic terminations of the probes. The same tubes can be connected to a Furness manometer via a *Scanivalve* system that allows the remotely controlled acquisition of 48 mean pressure signals. Fluctuating pressure is measured using 4935 ICP B&K microphones. The unsteady pressure is measured at 35 locations. These microphones are pre–amplified using a PXI system for data acquisition and analysis.

The remote microphone technique requires an appropriate calibration that takes into account the transfer function of the capillary tubes (as discussed by Arguillat, 2006).

2.5.5 Far field measurements

Two 1/2" 4191 B&K microphones are placed at each side of the airfoil in the mid–span plane. Directivity measurements are carried out by mounting the microphone supports onto a turning table at a distance $r = 1.7$ m from its center. For practical reasons the device rotates around a point located at $x = -0.075\,c$, $y = 0$, that is -15 mm away from the (O, Z) axis. The observation angle is expressed with respect to the airfoil chord and varies within the range $\pm 50°$ to $\pm 130°$.

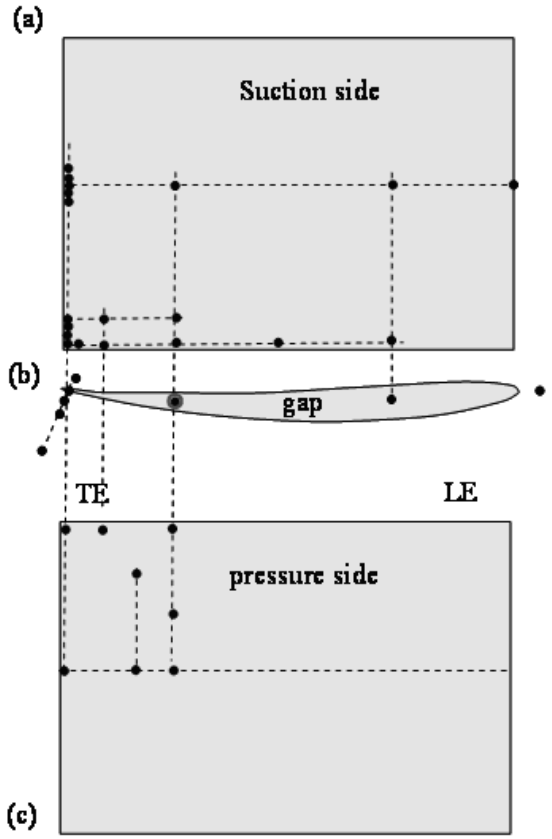

Figure 2.7: Overview of the unsteady pressure probe locations: (a) and (c) on suction and pressure side respectively, (b) on airfoil tip and on the lower plate (the circled one represents 2 probes, one on the tip facing and a second one on the plate).

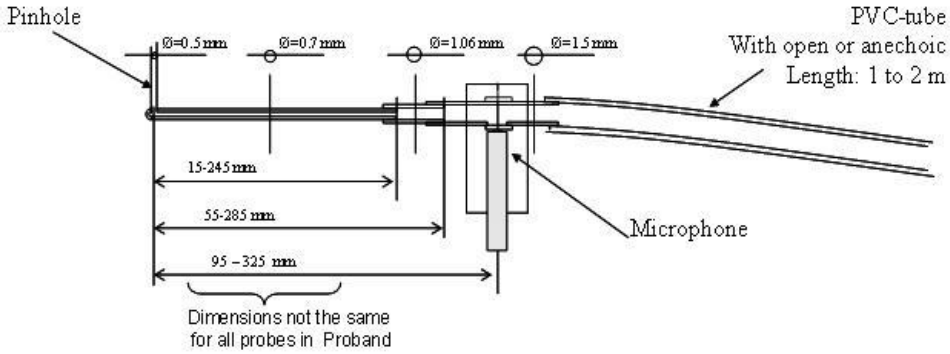

Figure 2.8: Sketch of remote microphone probes.

Chapter 3

Wavelet analysis

3.1 Wavelet transform overview

The fundamental idea behind the wavelets is to analyze according to scale. In wavelet analysis the scale that we use to look at data plays a special role. Wavelet algorithms process data at different scales or resolutions. In fact, if we look at a signal with a large window, we would notice gross features. Similarly, if we look at a signal with a small window, we would notice small features.

The wavelet analysis approach is to adopt a wavelet prototype function, called *analyzing wavelet* or *mother wavelet*, which has to be localized in both time domain and transformed (scale/frequency) space. The time–scale (or time–frequency) domain is then spanned by contracted/dilated and translated version of this prototype. Hence, good time resolution is achieved by means of contracted low–scale wavelet functions, while large–scale wavelets provide resolution in the transformed (scale/frequency) space.

As a consequence, a wavelet decomposition permits to represent a generic signal simultaneously in terms of a translation time (t) and a resolution time scale (r), whose inverse corresponds to the frequency (f). This is accomplished by projecting the acquired signal over the basis of compact support function $\Psi(t)$ obtained by

dilation and translation of the mother wavelet. Formally, the wavelet transform of the signal $p(t)$ at the resolution time scale r is given by the following expression

$$w(r,t) = C_{\Psi}^{-1/2} \int_{-\infty}^{+\infty} \Psi^* \left(\frac{t-\tau}{r} \right) p(\tau) \mathrm{d}\tau \tag{3.1}$$

where $C_{\Psi}^{-1/2}$ denotes a coefficient which accounts for the mean value of $\Psi(t)$, and the integral represents a convolution between $p(t)$ and the dilated and translated complex conjugate counterpart of $\Psi(t)$.

The most interesting dissimilarity with respect to the classical Fourier transform is obviously that individual wavelet functions are well localized in the time–scale domain. We note that in the Fourier decomposition the projection is performed over trigonometric functions, so that the physical information is spread over a theoretically infinitely extended time domain. Localized events are therefore missed by the Fourier decomposition while they are correctly retrieved by the wavelet transform through the representation of the signal over a two dimensional map in the time–frequency domain.

One way to see the time–frequency resolution differences between the windowed Fourier transform and the wavelet transform is to look at the basis coverage of the time–frequency plane. Fig. 3.1 shows a windowed Fourier transform, where the window is simply a square wave. The square wave window truncates the sine or cosine function to fit a window of particular width. Because a single window is used for all the frequencies in the windowed Fourier transform, the resolution of the analysis is the same at all locations in the time–frequency domain. The projection is not adaptive, so to speak.

The advantage of the wavelet transform is that the windows vary. In order to isolate signal discontinuities or sharp variations, on would like to have some very short basis functions. At the same time, in order to obtain detailed frequency analysis, one would like to have some very long basis functions. This is exactly the way the wavelet transform covers the time–frequency plane (Fig. 3.2). Thus, wavelet analysis provides immediate access to information that can be obscured

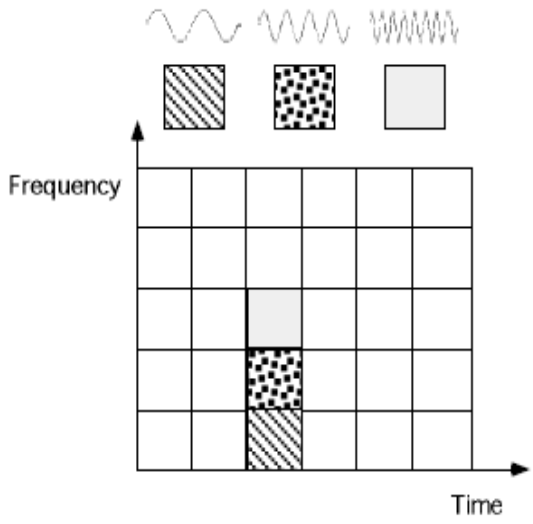

Figure 3.1: Fourier basis function and coverage of time–frequency plane.

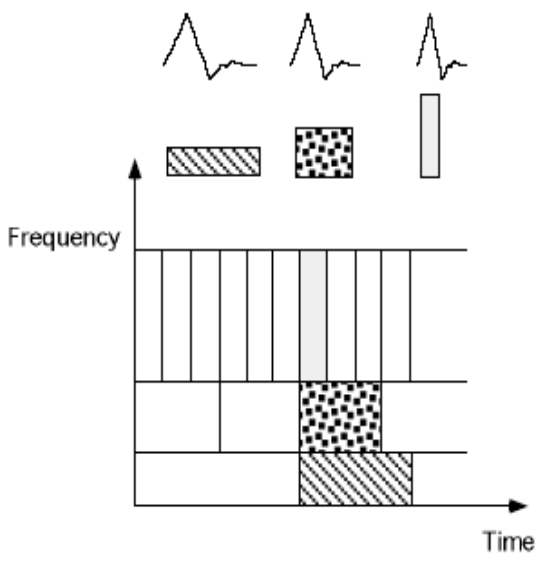

Figure 3.2: Wavelets basis function and coverage of time–frequency plane.

or hidden by other standard time–frequency projection like the windowed Fourier transform.

3.2 The Local Intermittency Measure concept

The post–processing procedure adopted therein is based on the wavelet transform of a pressure signal. As stated in § 1, the scope of the procedure is to extract from the wall–pressure and far–field pressure signals the most energetic non–periodic contributions localized in time and in space and to detect the fluid dynamic structures responsible for such strong pressure fluctuations.

In fact, as pointed out by Vassilicos (1996), the wavelet coefficients $w(r,t)$ have the property of enhancing singularities in the signal. As explained in the following, this feature may be exploited to detect strong non–periodic energy bursts characterizing turbulent flows.

The event tracking method used therein is based on the computation of the so called Local Intermittency Measure (Farge, 1992) defined as

$$\mathrm{LIM}(r,t) = \frac{w(r,t)^2}{\langle w(r,t)^2 \rangle_t} \tag{3.2}$$

where the symbol $\langle \bullet \rangle_t$ denotes a time average. This function enhances non–uniform distributions of energy in time, since the quantity $w(r,t)^2$ may be interpreted as the energy contained in the signal at the scale r and at the instant t. Therefore, the LIM distribution in the time–scale domain is a good indicator of the intermittency and magnitude of the energy fluctuations. Figure 3.3 shows an example of LIM distribution computed from a portion of pressure signal recorded on the wall.

In addition, it is worth noting that the numerator of Eq. (3.2), i.e. the square of the wavelet coefficients, represents the localized counterpart of the standard Fourier spectrum that can be recovered by simple time integration. An example of the Fourier spectrum recovered from the square of the wavelet coefficients plotted against the standard power spectrum is reported in Figure 3.4. Similar results have

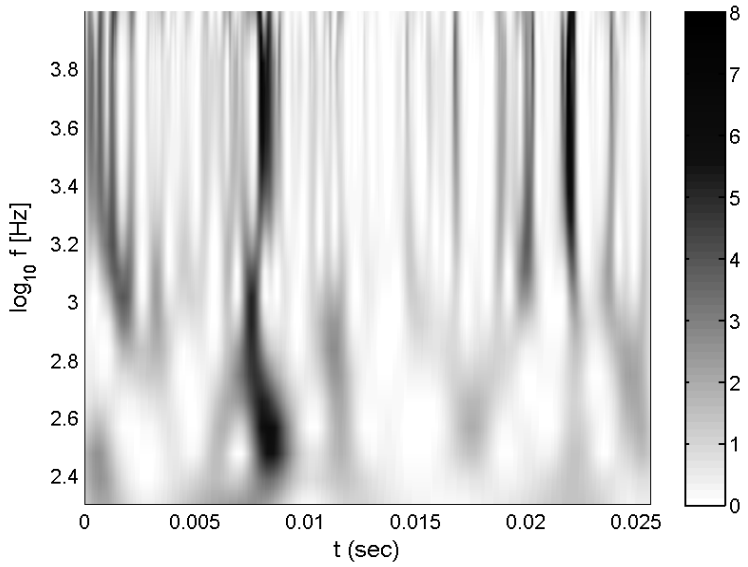

Figure 3.3: Example of LIM distribution computed for a portion of pressure signal recorded on the airfoil surface.

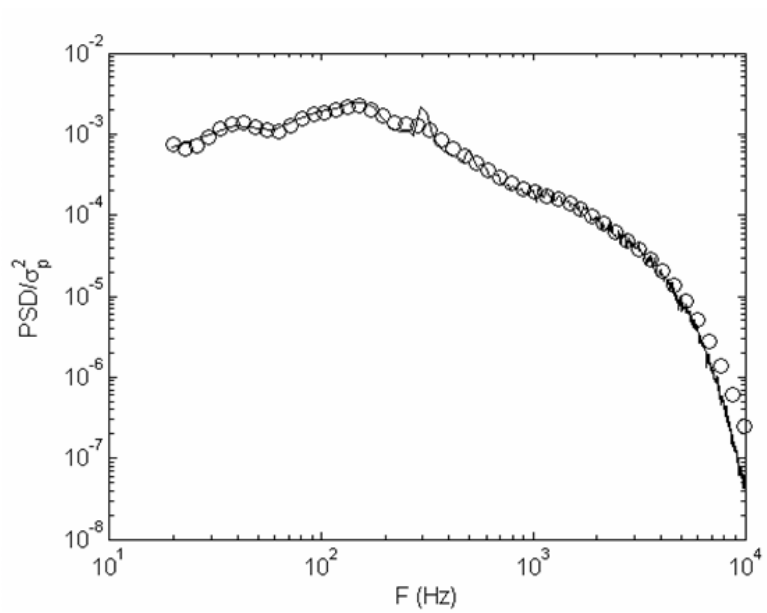

Figure 3.4: Power spectrum obtained from the wavelet transform ○, compared with a standard Fourier spectrum ——.

been obtained by using different wavelet kernels, demonstrating that the choice of the wavelet type does not influence the achieved results. It has been also checked that the results are independent from the use of orthonormal discrete or continuous complex wavelets. Examples elucidating these comparisons are not presented here for the sake of brevity.

In the following analyses, unless mentioned otherwise, the convolution in Eq. 3.1 is performed on single point pressure signals by means of a Fast–wavelet–transform algorithm. In particular the Battle–Lemarie Mother wavelet is used, and the wavelet expansion is performed over segments of 4096 samples, that is for a range of 12 degrees of resolution (scales).

Chapter 4

Event tracking procedure and conditional statistics

A wavelet–based post–processing procedure is presented in this section, which allows for educing strong non–periodic pressure fluctuations generated in turbulent flows. Using the peaks detected in the pressure signal as a trigger, phase average of pressure and velocity data may be performed in order to reconstruct shape, energy, and time–space correlation of the most energetic pressure fluctuations and of the suspected fluid dynamic noise–producing structures. The wavelet transform is indeed well suited to recover the phase of the largest intermittent fluctuations in the signal.

The phase is a random non–periodic and strongly non–Gaussian variable and the averaged signature, whenever is non–zero, helps to clarify the physical nature of the educed non–periodic contributions. The original method was introduced by Camussi & Guj (1997) and successively applied to pressure signals and validated by Guj *et al.* (2003), while applications to wall pressure data were presented in Camussi, Guj, & Ragni (2006).

The wavelet treatment of a pressure signal and the computation of the corresponding LIM distribution provide a suitable time–frequency representation of the

energy content of the pressure fluctuations (§ 3). Note that peaks of LIM represent large contribution of pressure variations to the overall SPL. Stated in different terms, a peak in the pressure LIM distribution may be associated with the occurrence of a pressure "event", in that the pressure fluctuations locally exhibit an energy content exceeding the observed overall value.

Therefore, the LIM amplitude at a selected scale r, can be thresholded in order to select events responsible for the largest pressure fluctuations and to determine how their appearance is distributed in time: for a given scale $r = r^*$, LIM as a function of time can be analyzed and a proper trigger threshold level T can be fixed. When, for $t = t_0$, $LIM > T$, it may be assumed that a particular type of pressure event has been detected at the time instant $t = t_0$ at the scale $r = r^*$. By varying the trigger level, one can select events of different levels of energy, whereas for $r > r^*$ one can observe fluctuations corresponding to smaller resolutions (or larger scales).

4.1 Auto–conditioning method

Once the pressure events have been selected and well localized in the time domain, one may perform a conditional average of the original pressure signal. The time signature of the pressure events can be recovered by ensemble averaging the pressure signals centred at the instants $\{t_0\}$ when energy overcomes the trigger threshold (Figure 4.1). If t_0 is an instant when an energy burst is detected for a certain trigger level T, we can define $p^{(T)}(t, t_0)$ as the portion of the original pressure signal centred in t_0 and extending for a time interval of proper width (Figure 4.1). The ensemble averaging procedure is then taken over all t_0 when the energy is above the trigger level, and may be written (in the continuous form) as

$$\langle p \rangle (t - t_0) = \langle p^{(T)}(t, t_0) | \{t_0\} \rangle_{t_0} \tag{4.1}$$

which indicates that the procedure leads to a statistical averaging conditioned on the events $\{t_0\}$. By varying the resolution where the peaks' detection is performed,

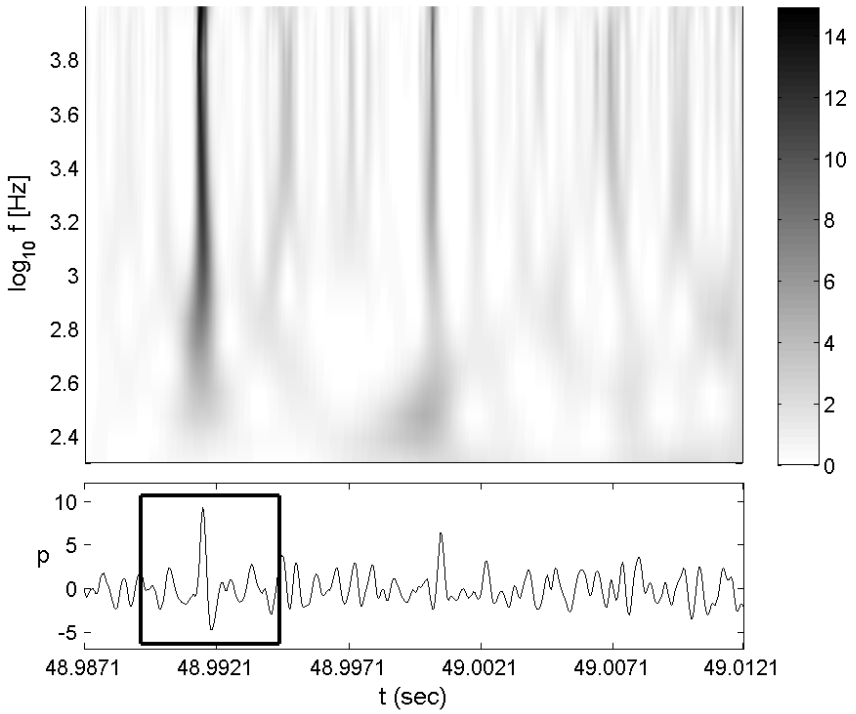

Figure 4.1: Example of selection procedure: the large value of LIM in the upper panel indicates that an event occurs at the probe location in $t_0 \sim 48.992$ s. Once the event is detected the portion of pressure signal centered in t_0 is extracted to perform the conditional average.

it is possible to observe structures of different size.

This auto–conditioning procedure leads to an ensemble averaged time signature of the fluctuating pressure, which represents the most probable shape of the most energetic structures which are hidden in the original chaotic signal.

4.2 Averaged cross–conditioned structures

The conditioning method explained above may be applied to a couple of signals acquired simultaneously in order to explore their statistical space–time correlation and to find whether a connection exists between the events tracked from the trigger signal and the coherent structures in the conditioned one. The relevance of this cross–analysis is evident, as it permits to investigate the space–time correlation between the largest pressure fluctuations measured at different positions on the airfoil surface. Consider, for example, the typical case of a wall–pressure perturbation which is convected downstream by the flow: the cross–conditional analysis performed on a suitable set of wall–pressure signals could help to estimate the convection velocity within the boundary layer.

Moreover, a pressure/velocity cross–analysis with the pressure signal used as a trigger, is an effective tool for understanding physical mechanisms underlying the generation of noise: it allows for extracting from velocity data the aerodynamic structures correlated to large localized pressure peaks on the wall and in the far field. In fact, whenever a strong pressure fluctuation occurs at a particular position in the region of interest (far field or airfoil surface), one may infer that it might physically correspond to any hydrodynamic effect (as the passage of a coherent vortex), or that instead it might be caused by any local acoustic perturbation (due to a noise–producing phenomenon, occurring elsewhere and radiating in the surrounding field).

In details: once the set $\{t_0\}$ of the selected time instants is available, the conditional average can be performed either on the single point velocity time series

(HWA signals) or on the set of PIV snapshots available, provided that the velocity measurements are acquired simultaneously with the pressure signal used as trigger. The velocity signal is ensemble averaged to eliminate random fluctuations and to educe the coherent contribution to the signal, should it exist. If the time signature of the noise–generating structures has a basic form in the recorded velocity signal, this "template" is revealed by the averaged signal. As a result, in the case of joint HWA/pressure measurements, the outcome of the cross–conditional procedure analysis should be an averaged time–signature of velocity, representing the most probable fluid dynamic structure correlated to the pressure fluctuations on the wall of the airfoil. A PIV/pressure conditional statistics allows for a more reliable topological interpretation about the nature of the fluid dynamic events generating noise. In that case, the outcome of the procedure should be the averaged PIV field showing the turbulent velocity field statistically correlated to the measured largest pressure fluctuations.

Besides, an interesting point is the possibility of individuating, statistically, the position where noise has been radiated. According to Guj *et al.* (2003), we can define Δt as the total time delay obtained as a difference between the time instant characterizing the averaged time signature (which can be deduced from its maximum) and the reference time corresponding to the peaks in the far–field pressure. Taking into account the local convection velocity and the speed of sound c (the pressure perturbations propagation velocity), it is possible to determine the spatial location of the noise emitting events. As an example, assuming for simplicity the sound propagation velocity (c) to be infinite, the acoustic time may be set equal to zero. Thus, for $c = \infty$, three possibilities can be encountered: $\Delta t = 0$ for a noise emission at the same position as the probe, $\Delta t < 0$ for a noise emission downstream, and $\Delta t > 0$ for a noise emission upstream. For finite c, the effect of the acoustic propagation is always a negative delay to be accounted for. Accounting also for the local convection velocity, which is evaluated by a proper aerodynamic characterization of the flow, and the measured Δt magnitude, it is therefore possible

to retrieve the spatial location of the averaged noise source. We point out that the magnitude of the time delays and of their spatial counterpart as extracted from the averaged structures plays a fundamental role in the interpretation of the results presented in § 5.

Chapter 5

Results

5.1 Wall–pressure auto–processing

The ensemble averaging procedure described in § 4 is applied to the whole set of measured wall–pressure signals thus allowing for the spatial evolution of the most energetic averaged pressure time-signatures to be analyzed. As will be shown in the following, this could help to clarify the nature of the events responsible for the largest pressure fluctuations over the airfoil surface.

The auto–conditioning method provides the wall–pressure averaged signatures in several positions over the airfoil surface. In the no–gap reference configuration, significant results are obtained only with the probes placed in the mid–span region. As clarified below, in this region the effect of the chord–wise position seems to be relevant. An overall summary of results obtained considering probes located at mid–span ($z = Z = l/2$) for the no–gap reference configuration is given in Figure 5.1. It is shown that the shape of the averaged signatures significantly changes with the x/c parameter. The behaviour obtained close to the leading edge seems to indicate that acoustic effects are dominant with respect to hydrodynamic perturbations. This is an expected result since in the leading–edge region the boundary layer is very thin and not yet developed so that acoustic perturbations,

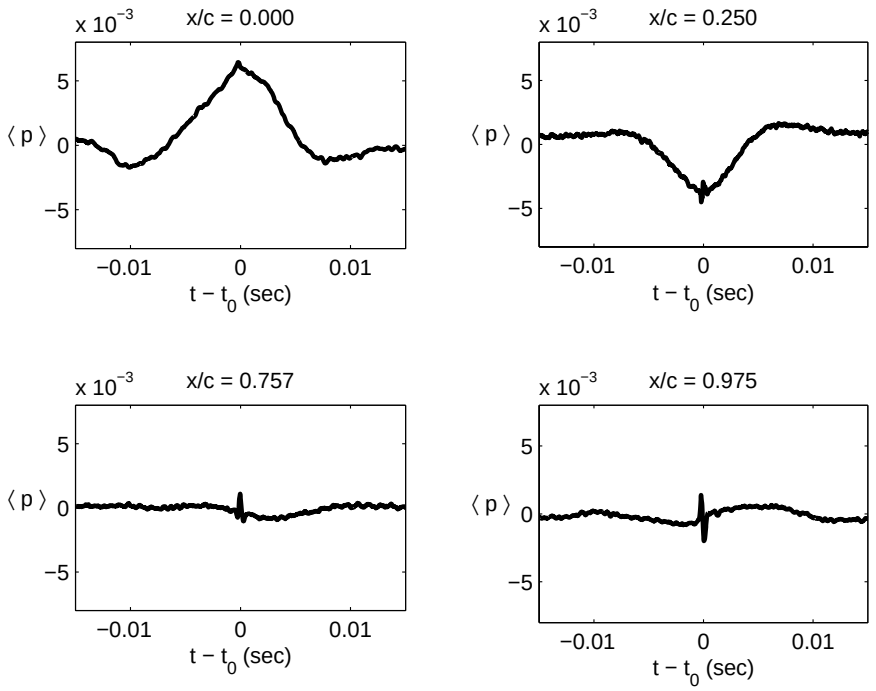

Figure 5.1: Averaged pressure time signatures obtained for several chord–wise positions at mid span on the suction side for the no gap reference configuration.

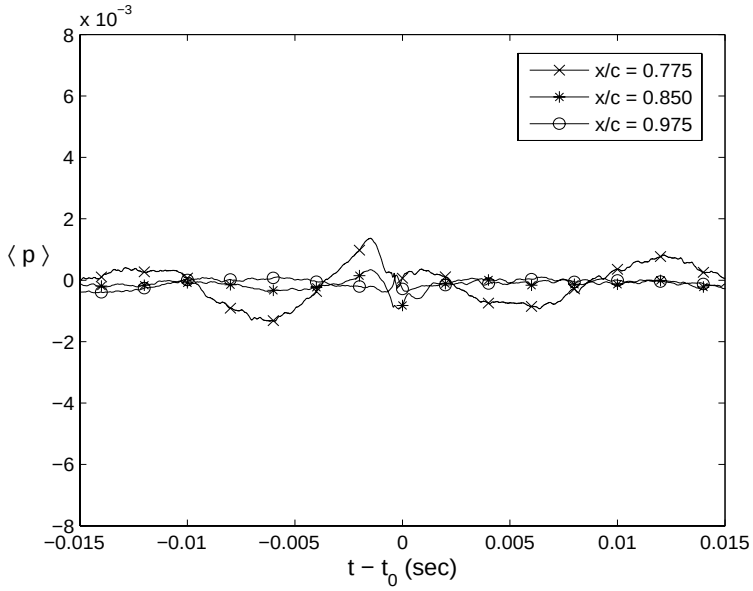

Figure 5.2: Averaged pressure time signatures obtained from several transducers at mid span in the pressure side of the airfoil for the no gap reference configuration.

generated by the impact of the incoming unsteady flow against the airfoil surface, are the main sources of noise.

When we move towards the trailing edge, a different behaviour is observed, as shown in the case $x/c = 0.25$ of Figure 5.1. Here a pressure drop is observed, thus suggesting that, in a statistical sense, the pressure fluctuations are generated mostly by vortical structures passing close to the pressure probe position.

In the region close to the trailing edge no significant results are obtained as an effect of the back–ground disturbance and the signal–to–noise ratio of the averaged pressure signatures is too low for any physical interpretations to be addressed.

No significant results are obtained also in the pressure side confirming that being the boundary layer very thin, the hydrodynamic perturbations induced by vortical structures are very weak and, from a statistical viewpoint, are uncoherent. An example of results obtained in the pressure side for the no–gap reference configuration is given in Figure 5.2. The presence of a gap leads to pressure oscillations

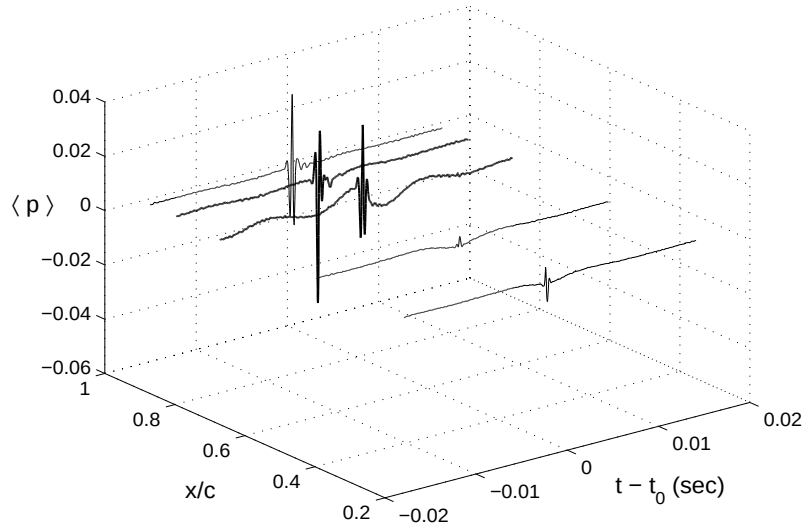

Figure 5.3: Averaged pressure time signatures obtained for several chord–wise positions in the tip region for the reference gap configuration.

in the averaged signatures, as evidenced in Figures 5.3–5.5 for the reference gap configuration. In Figs. 5.3 and 5.4 one may note that the oscillations are more pronounced close to the trailing edge and at the airfoil tip in correspondence of the gap. Figure 5.5 shows that the amplitude of the oscillating averaged pressure signature becomes larger for increasing width of the gap, with both the angle of attack and the inflow speed kept fixed at their reference values. The observed behaviour is due, probably, to vortex shedding from the side edge of the airfoil but, being such an effect not evident in the pressure power spectra, it has to be attributed to intermittent unsteady events which are not revealed when the signal is projected onto the Fourier basis. The physical nature of the observed phenomenon could be found into the mechanism of roll up of the vortical structures shed from the lower side of the airfoil and further insights would be inferred from the cross–analysis of the next sections.

Finally, a statistical analysis of the waiting time between consecutive wall–

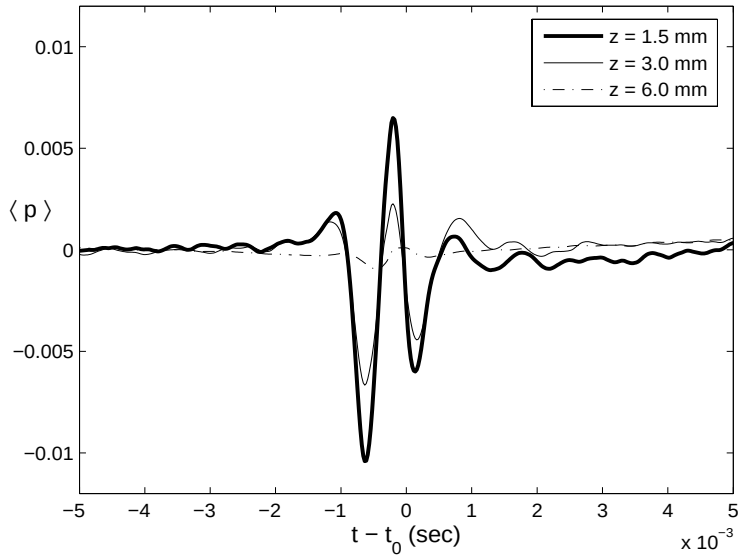

Figure 5.4: Averaged pressure time signatures obtained in the trailing edge region for the reference gap configuration: effect of the distance from the gap (z).

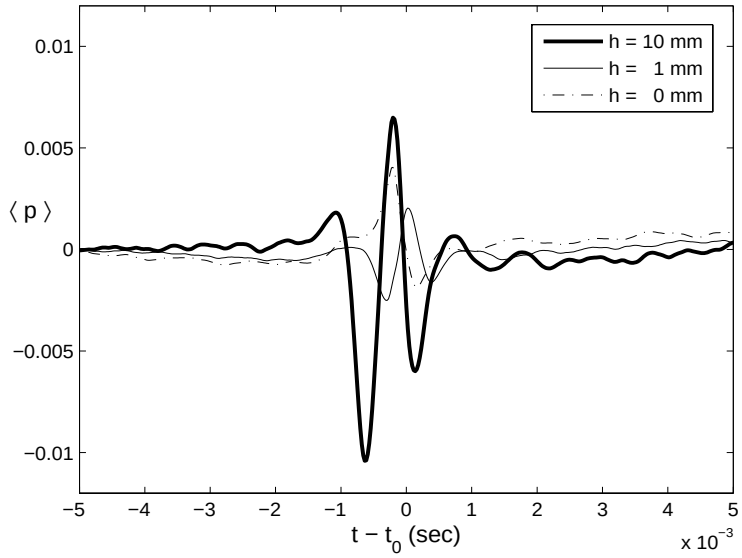

Figure 5.5: Averaged pressure time signatures obtained in the trailing edge region at the tip edge: effect of the gap width, with U_0 and α kept fixed at their reference values.

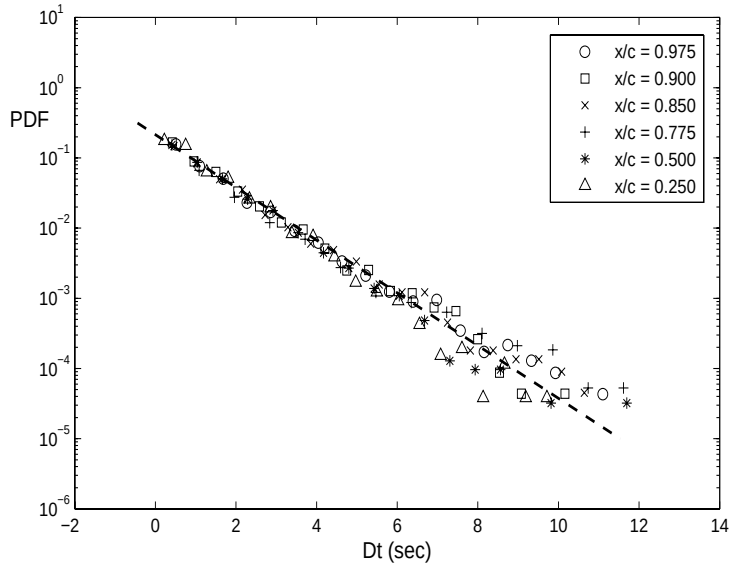

Figure 5.6: PDF of the time delay Δt between consecutive pressure events. The dashed line represents a pure exponential decay of the form $y = e^{-0.98x}$.

pressure events has been performed by computing the PDF of the time delay $\Delta t^i = t_0^i - t_0^{i-1}$, $\{t_0\}$ being the set of time instants corresponding to the peaks in the wall–pressure LIM. As stated in § 1, this study may be useful in giving more insight into the events selected for the averaging procedure performed above and, in particular, for the evaluation of a possible correlation between them. The PDF of the elapsed time between successive pressure events detected in the tip region is reported in Figure 5.6. As known from previous works the PDFs exhibit exponential tails that appear linear on the semilog plot. The exponential distribution of the waiting time is characteristic of Poisson statistics of uncorrelated events. From a physical viewpoint the exponential decay indicates that the selected pressure events may be considered statistically independent from each other. A satisfactory collapse of the PDFs can be appreciated, suggesting that such behaviour is an intrinsic property of the random variables analyzed.

The results in Figure 5.6 yield a further confirmation of the reliability of the

adopted identification method, which allows for separating the coherent intermittent fluctuations from the background.

5.2 Wall–pressure cross–conditional statistics

As mentioned in § 4, a wall–pressure cross–conditional analysis permits to inspect whether a physical process drives the most energetic pressure perturbations throughout the turbulent region developing over the airfoil surface. In fact coherent pressure fluctuations detected in different locations on the wall might either be generated by independent fluid dynamic/acoustic perturbations or might stem from the same perturbation which convects or radiate in the position where they are detected.

The cross–conditional procedure performed on the wall–pressure signals provides the space–time correlation between the largest pressure fluctuations in the turbulent region. Figure 5.7 shows the results of the cross analysis conducted on the pressure signals in the tip region: the pressure signal recorded at $x/c = 0.775$ is used to trigger the time series provided by the pressure probes along the tip. It may be seen that the averaged pressure signatures preserve the same shape. but a time shift is revealed moving downstream. This is compatible with the hypothesis that the coherent pressure bursts somewhat consists of the same perturbation retrieved in $x/c = 0.775$, which is transported downstream by the turbulent boundary layer.

In account of the pressure taps location, the resulting time shift permits to evaluate the convection velocity within the boundary layer in the tip region. The value computed from results in Figure 5.7 is $U_c \sim 50$ m/s.

5.3 Far–field/wall–pressure conditional statistics

A first attempt to localize the position at which acoustic noise is generated consist of triggering the wall–pressure signals with the LIM peaks detected in the far

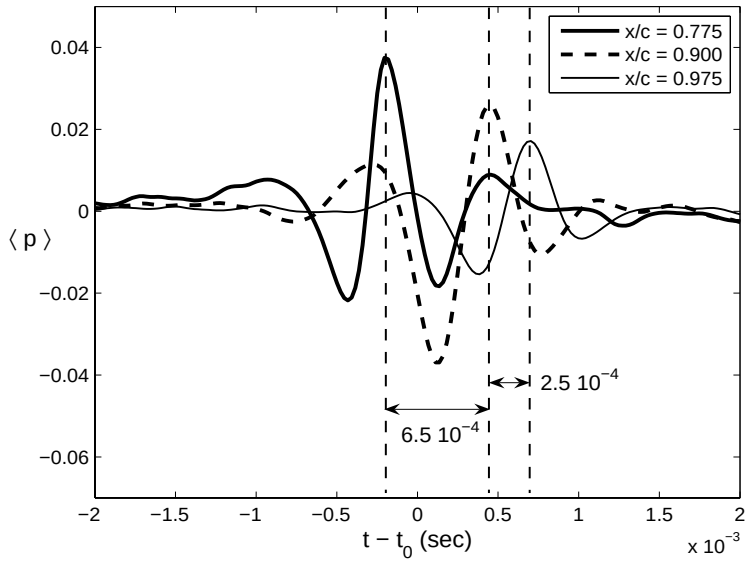

Figure 5.7: Pressure cross–conditional correlation in the tip region for the reference gap configuration.

field. As explained in § 4, the outcome of such cross–analysis is a statistics of the time delay between the coherent wall–pressure fluctuations and the largest acoustic perturbations in the far field. A wall–pressure signal recorded in the region where noise is generated should provide, once conditioned by the far–field trigger, an averaged time signature whose time delay approximate the time need for the speed of sound to cover the distance from the wall to the far–field microphone location.

In the present analysis a pressure signal is recorded by a far–field microphone placed at about 1 m away from the airfoil surface in the suction side. The peaks detected by the wavelet treatment of the acoustic pressure are then used to trigger the wall–pressure signals acquired simultaneously in the tip region for the reference gap configuration. Note that the distance of 1 m is expected to be covered by the isoentropic speed of sound ($c_s \sim 340$ m/s) in $\sim 3 \cdot 10^{-3}$ s. Therefore in the following considerations, we will assume $\Delta t_0 = 3 \cdot 10^{-3}$ s as a reference value by which one may identify the most probable location on the airfoil surface where

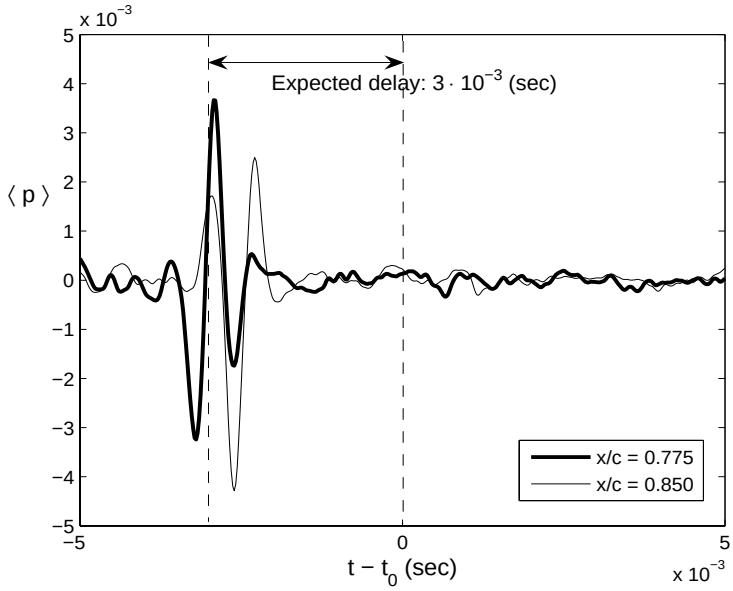

Figure 5.8: Averaged wall–pressure time signature for transducers in the tip region of the reference gap configuration and with the far field signal used as trigger.

acoustic perturbations originate.

Significant correlation has been retrieved only in the tip region downstream of half chord, as shown in Figures 5.8 and 5.9. It may be noticed that the (negative) time shift exhibited by the averaged pressure signal at $x/c = 0.775$ falls quite close to the reference value, while moving downstream, the correlation appears weaker and the time delay decreases.

From the results described above the following physical interpretation may be argued: the most effective acoustic source locates approximately just upstream of the pressure tap at $x/c = 0.775$. The corresponding perturbation radiates in the far field, being perceived by the microphone after $\sim 3 \cdot 10^{-3}$ s, and besides it is convected downstream by the turbulent boundary layer. On the basis of such interpretation, the discrepancy between Δt_0 and the time shift exhibited by the pressure probes considered downstream of $x/c \sim 0.7$ is to be attributed to the convection process from the noise source location to the pressure tap position. In fact,

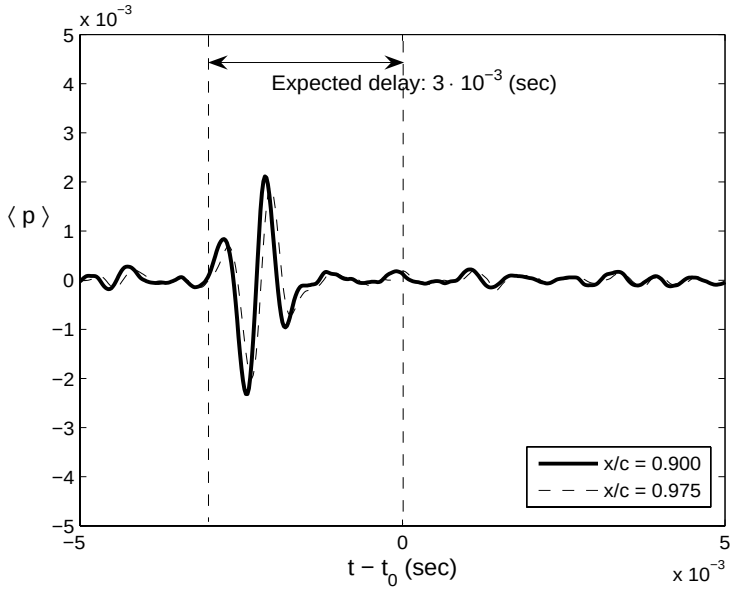

Figure 5.9: Averaged wall–pressure time signature for transducers in the tip region of the reference gap configuration and with the far field signal used as trigger.

accounting for the convection velocity evaluated in § 5.2, the spatial counterpart of the time shift between the averaged pressure signatures in Figures 5.8 and 5.9 is consistent with the actual position of the pressure probes along the tip.

5.4 Pointwise–velocity/wall–pressure conditional statistics

As discussed in § 2, simultaneous velocity/pressure measurements have been performed by placing a single hot wire probe close to the airfoil trailing edge at a mid–span location. These experimental investigations provided useful data to perform a statistical analysis, which gives further clarifications on the physical nature of the fluid dynamic structures in the noise generation phenomenon. The conditioning method explained in § 4 has been applied to the HWA/wall–pressure data, in order to extract aerodynamic events correlated to large localized pressure peaks

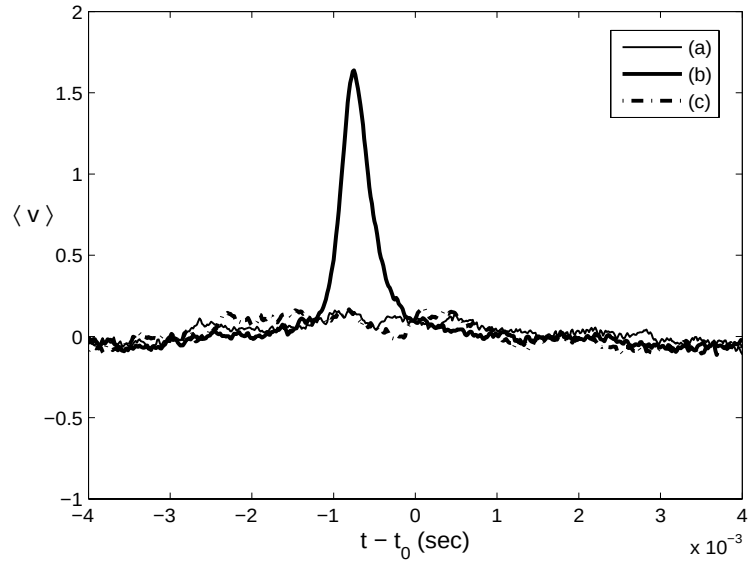

Figure 5.10: Pointwise pressure–velocity correlation in the trailing edge region for the no gap reference configuration: (a),(b), and (c) represent the averaged hot–wire velocity time signature with the pressure signal at $z = 88, 100, 106$ mm respectively used as trigger.

on the wall of the airfoil. The results obtained from the cross–conditioning procedure for both the reference configurations are presented. In Figures 5.10 and 5.11 the averaged velocity signatures for the no–gap reference configuration are depicted: the HWA signal has been conditioned by extracting the pressure events in several locations along the trailing edge and in the mid–span region. A relevant pressure–velocity correlation can be evidenced only close to the trailing edge at the mid–span location ($x/c = 0.975; z = 0$).

Then, introducing a finite gap, it is evident from Figure 5.12 that no relevant gap effects occur in the mid–span region. However, as shown on Figure 5.13, the auto–conditioned velocity signature exhibits a drop, whose amplitude significantly grows for increasing width of the gap. The cross–correlation between the observed velocity drop and the pressure peaks detected along the tip has been then explored

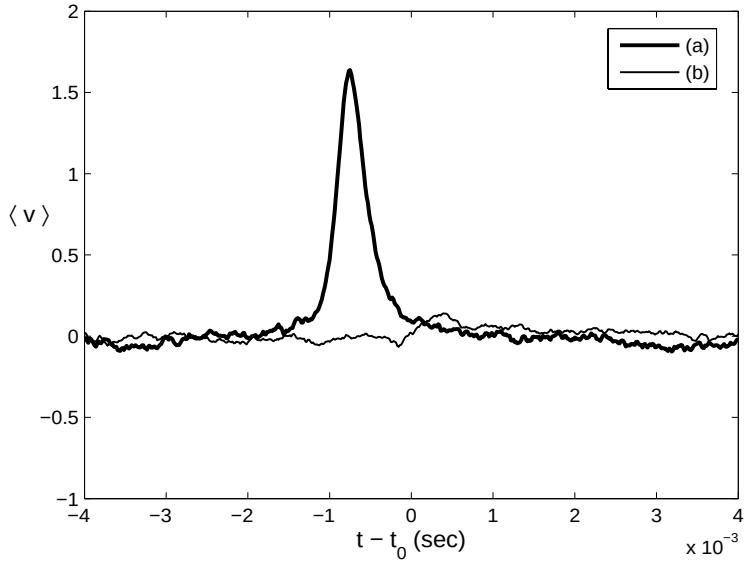

Figure 5.11: Pointwise pressure–velocity correlation in the mid span region for the no gap reference configuration: (a) and (b) represent the averaged hot–wire velocity time signature with the pressure signal at $x/c = 0.975$ and $x/c = 0.775$ respectively used as trigger.

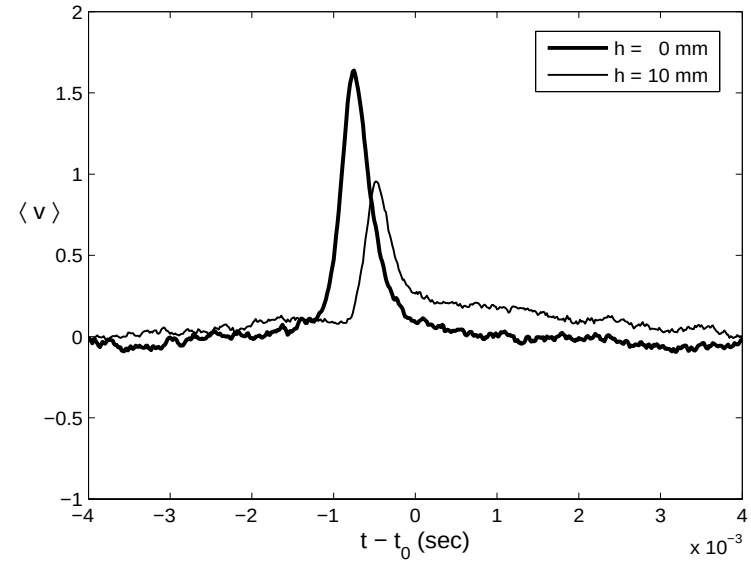

Figure 5.12: Pointwise velocity–pressure correlation in the mid–span region at the trailing edge ($x/c = 0.975$): effect of the gap.

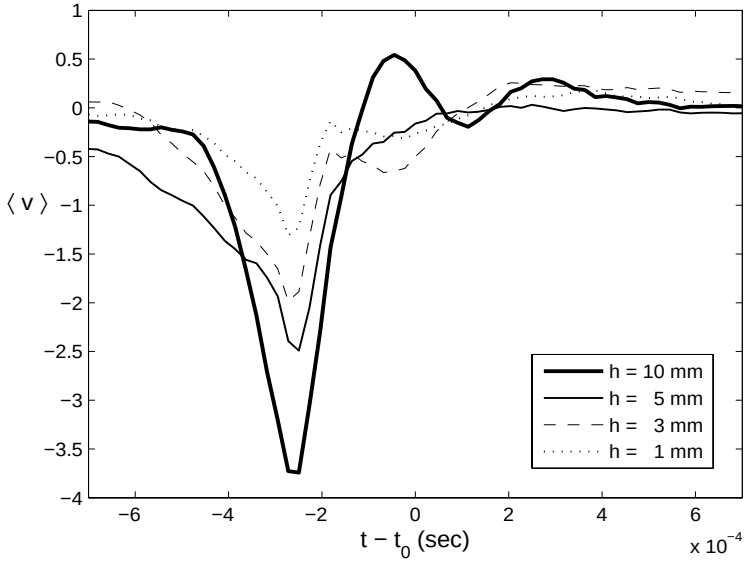

Figure 5.13: Pointwise velocity auto–correlation in the tip edge region at the trailing edge ($x/c = 0.975$): effect of the gap.

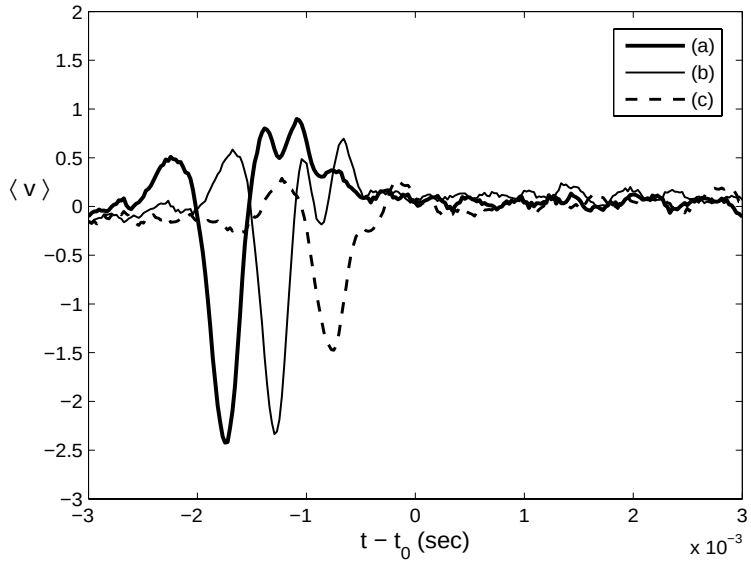

Figure 5.14: Pointwise pressure–velocity correlation in the tip edge region for the reference gap configuration: (a),(b), and (c) represent the averaged hot–wire velocity time signature with the pressure signal at $x/c = 0.975,\ 0.900,\ 0.775$ respectively used as trigger.

for the reference gap configuration. The achieved results are reported in Figure 5.14 for different pressure probe positions. Note that the shape of the velocity signature completely changes with respect to the one obtained by triggering the HWA signal with the pressure in the mid–span region (see Figs. 5.10 and 5.11). It is shown that moving along the tip, the phase of the signature changes. The non–zero time delay indicates that the fluid dynamic events (hot wire) associated to the emission of noise (pressure events) is not located spatially at the same position as the pressure probe. The location of the major fluid dynamic structure (which may act as a sound source) is upstream of the pressure taps. In fact, the phase delay increases as the distance between the pressure probe and the hot wire probe decreases. In account of the mean velocity and the velocity of sound, the phase shift of the signatures can be converted into a spatial delay and the resulting position of the

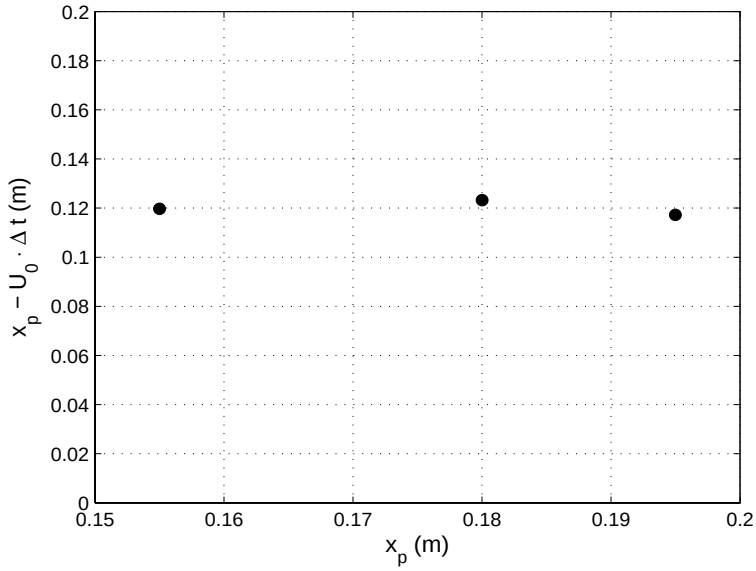

Figure 5.15: Reference gap configuration: spatial delay vs pressure tap position (x_p), computed by the time delay resulting from the pointwise pressure–velocity correlation in the tip region.

noise source, even though qualitatively, can be determined. The results reported in Figure 5.15 show that such a location is upstream of the trailing edge at about $x = 140$ mm from the leading edge.

5.5 PIV/wall–pressure conditional statistics

The joint analysis of PIV measurements (discussed in § 2) and of single point pressure measurements is performed only for the reference gap configuration. Figure 5.16 shows the location of the pressure taps mounted on the tip side of the airfoil. A third microphone was placed in the far field on the suction side of the airfoil. On the basis of the HWA/wall–pressure analysis presented in § 5.4, we may expect the pressure signals recorded by the probe B placed at $x/c = 0.75$ (see Fig. 5.16) to provide the most useful data for the conditional PIV/wall–pressure

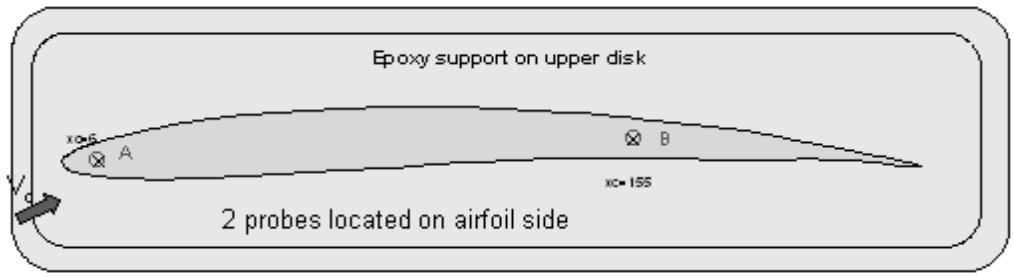

Figure 5.16: Side view of the tip edge of the airfoil: position of the two pressure taps in the joint PIV/pressure measurements.

analyses. Thus, in the present investigation we concentrate primarily on this pressure signal that, once treated with the wavelet method, provides the set of instants from which the corresponding PIV velocity fields are selected.

Contrary to the previous analyses, in this phase the pressure signal is processed by using a continuous complex wavelet expansion, so as to achieve a more accurate time–frequency resolution. Once the pressure events are extracted at the wall, the conditional analysis has been carried out by averaging together the PIV snapshots corresponding to the selected timing of the wall–pressure events. The LIM threshold criterion can be restricted to specific frequency bands in order to select wavelets of a given scale. Examples are shown in Figures 5.17 and 5.18 for both low and high frequency containing events. The corresponding flow patterns are identified with the method described above.

As stated in § 2, 60 PIV snapshot are available from each 60 sec acquisition series. This represents a basic constraint to take into account, as it is evident that only some of the instantaneous velocity fields captured by these 60 snapshots could be selected. Thus, the wavelet transform is performed over segments of 256 samples, that is[1] $1.2 \cdot 10^{-2}$ s, centered on the time instants corresponding to the PIV acquisition timing (see e.g. Figs. 5.17 and 5.18). Therefore, the selection of a

[1]Recall that the sampling frequency for the pressure acquisition was 20 kHz in this phase of the experimental campaign.

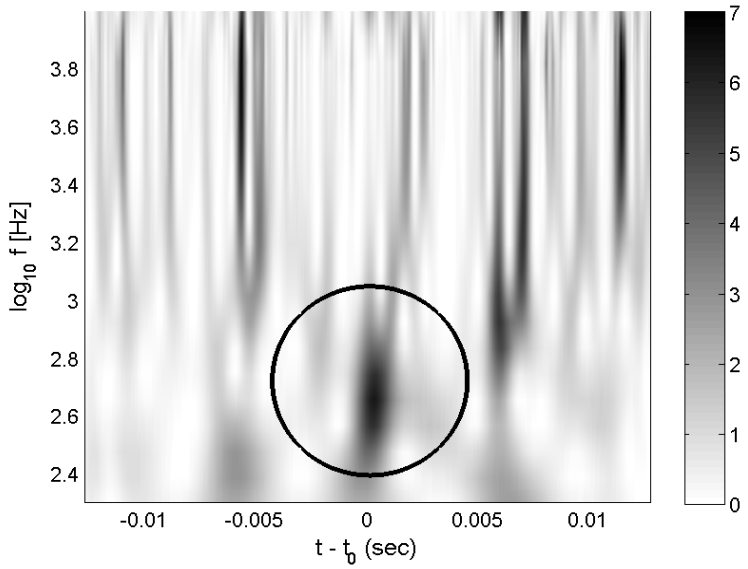

Figure 5.17: An example of a low–frequency pressure event (evidenced by the black circle) detected in the wavelet time–frequency domain from the pressure probe located at $x/c = 0.75$.

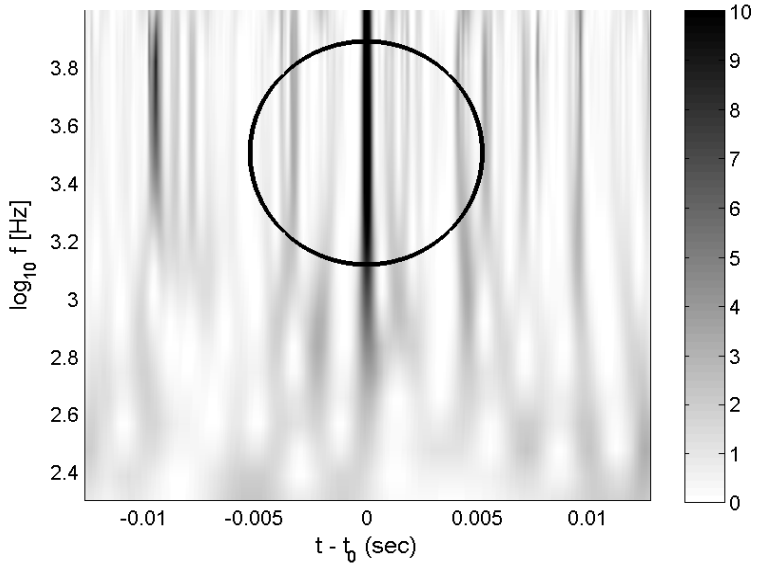

Figure 5.18: Same as previous plot but evidencing a high–frequency event.

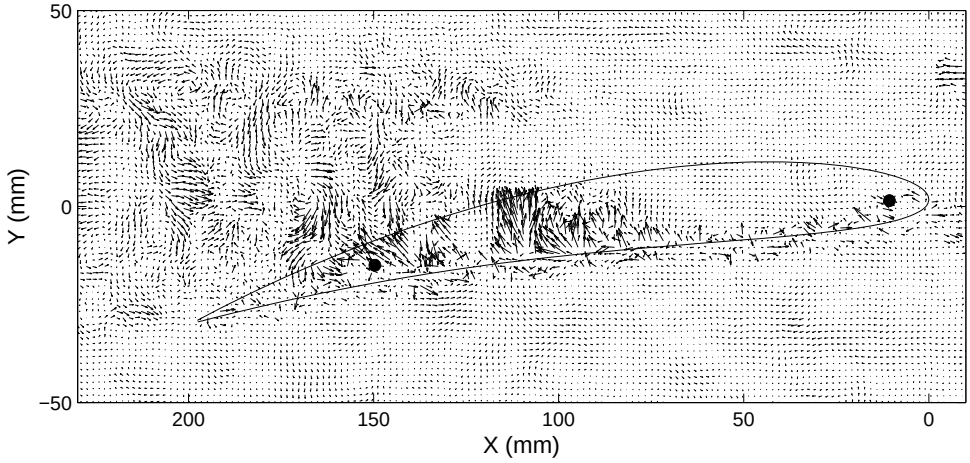

Figure 5.19: Averaged tip–flow field statistically related to the largest high–frequency pressure fluctuations on the wall. The black circles denotes the pressure probes mounted on the tip facing of the airfoil at $x/c = 0.05$ and $x/c = 0.75$.

PIV field occurs only when the LIM peak is located in correspondence of the origin of the time axis which results in a very small number of selected events.

The set of selected velocity fields are eventually averaged together leading to a non–zero averaged tip–flow structure which, should it exist, evidences the most probable fluid dynamic event responsible for the observed large pressure peaks. The selection procedure, applied to all the 10 acquisition series, provided a total of 119 pressure events. Furthermore, as shown on Figures 5.17 and 5.18, the LIM peak frequency localization can vary from one case to another. Therefore a distinction has been also considered according to the frequency content of the pressure events (low or high frequencies). Among the 119 events selected, 18 presented a low–frequency behaviour, whereas 75 were prevalently associated to high–frequency fluctuations. The remaining 31 fields evidenced events with a broadband frequency content.

The achieved ensemble averaged field corresponding to high–frequency events is shown in Figure 5.19. No relevant differences have been evidenced neither when

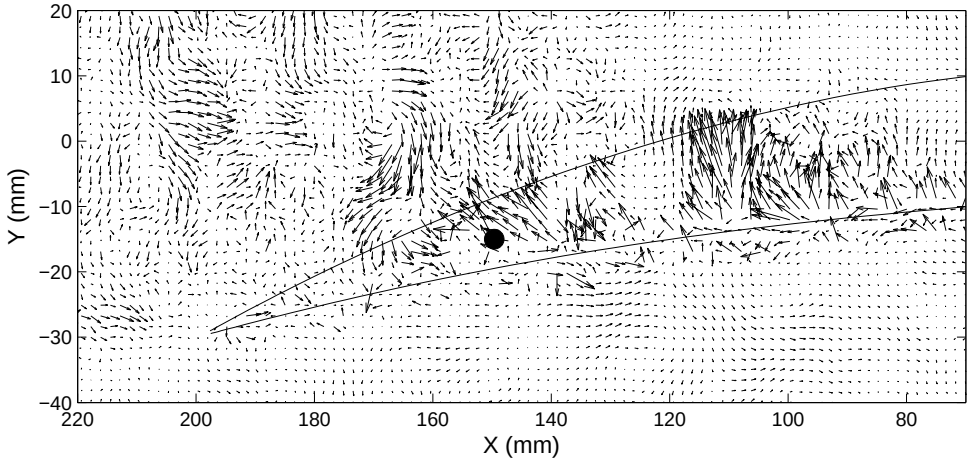

Figure 5.20: Detail of previous plot.

no distinction between high and low frequency events is performed nor when the low–frequency events are considered. In the latter case a lower signal–to–noise ratio is documented due to the limited number of samples selected. In any case, in the region upstream of the pressure probe position, thus very close to the region where the source was supposed to act, a non–zero fluid dynamic structure is revealed. A detail is shown on Figure 5.20. From the physical viewpoint, this event seems to consist of a motion of the fluid from the pressure side of the airfoil towards the suction side. Actually, since the PIV snapshots are taken in the mid–gap plane, the figure shows the corresponding 2D cut of a 3D turbulent structure. One may assume such a structure to be associated to a roll–up phenomenon occurring at the tip edge of the airfoil, but an exact interpretation can not be proposed unless a cross section analysis of the flow is performed.

5.6 PIV/far–field conditional statistics

The PIV/far–field pressure conditional analysis has been performed in order to definitely identify coherent structures in the gap flow which behave like noise sources.

The physical conjecture underlying the present investigation is that coherent fluid dynamic structures developing in the gap region, independent of their phase, generate large pressure fluctuations in the far field, that can be used for triggering and selecting instants of noise emission.

On the basis of the same arguments reported in § 5.3, and accounting for the limitation on the number of PIV snapshots available (see § 5.5), the selection procedure consists of finding whether the LIM of the far–field signal exhibits a peak for $t - t_0 = \Delta t_0$, where $\{t_0\}$ represents the PIV timing and Δt_0 is the acoustic reference time, that is the acoustic time counterpart of the distance from the wall to the far–field microphone. In fact, in a statistical sense, whenever a PIV field corresponds to a noise generating turbulent structure, a pressure perturbation should reach the far–field microphone after $3 \cdot 10^{-3}$ s.

An important issue to be addressed in this phase is the need for a specific frequency band investigation. In fact, as demonstrated by Grilliat *et al.* (2007), the tip leakage flow seems to contribute significantly to the far–field sound level in the frequency range between 3 kHz and 7 kHz, while for lower frequencies the far–field power spectra for the two reference configurations almost coincide, which means that the noise field radiated from the gap is ruled out by the trailing edge noise in such frequency band. Therefore only the pressure events detected in the 3–7 kHz range should correlate statistically with the coherent structures in gap flow.

Figure 5.21 shows the averaged tip–flow field obtained by tracking the far–field pressure events within the range 3–10 kHz. The result evidenced the presence of a fluid dynamic structure at half chord. The considerations reported at the end of § 5.5 still apply in this case. The PIV/far–field conditional statistics definitely confirms that the tip flow affect significantly the noise energy level within the frequency band analyzed.

Finally the PIV/far–field cross–analysis has been repeated for the frequency spanning from 200 Hz to 3 kHz. The resulting averaged gap flow is shown on Fig-

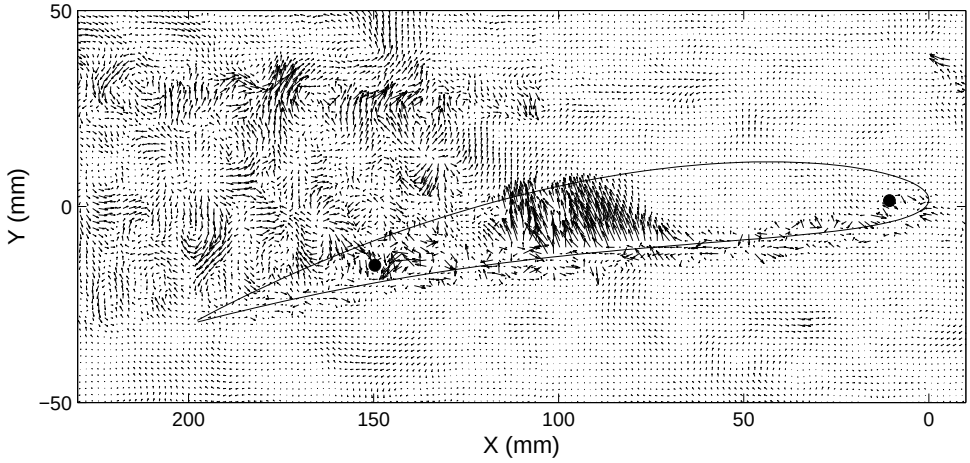

Figure 5.21: Averaged tip–flow field statistically related to the largest high–frequency pressure fluctuations in the far field.

ure 5.22. It may be observed that the correlation between the peaks in the far field and the tip–gap flow is quite weak, which is in agreement with the aforementioned experimental investigations (Grilliat *et al.*, 2007).

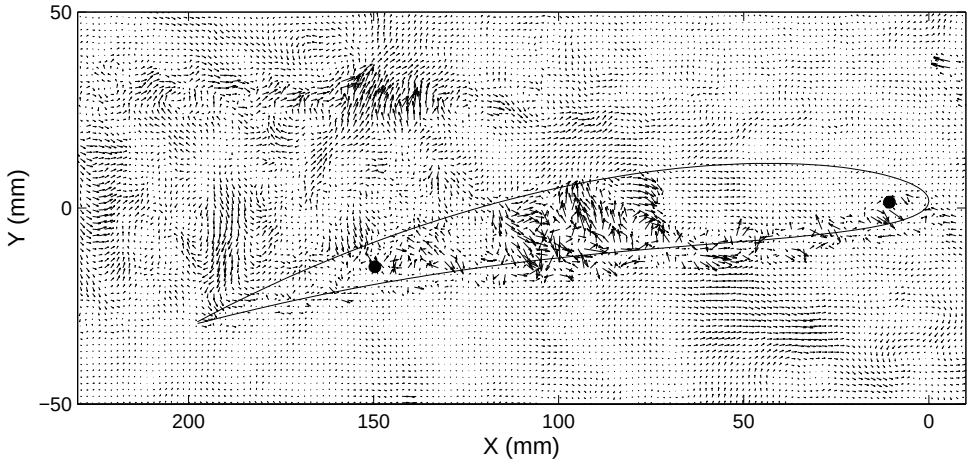

Figure 5.22: Averaged tip–flow field statistically related to the largest low–frequency pressure fluctuations in the far field.

Chapter 6

Conclusions

A detailed analysis of wall–pressure and Hot Wire/PIV velocity data measured around an airfoil with and without a tip leakage has been presented. The post–processing procedure was based on the application of the wavelet transform to the wall–pressure signals and the computation of conditional averages of both the pressure and the velocity data. In the self noise configuration, hydrodynamic wall–pressure fluctuations have been shown to be mostly related to the boundary layer separation of the suction side near the trailing edge. The presence of the gap leads to quite different behaviours since the most probable fluid dynamic event causing wall–pressure peaks is found to be associated to a roll–up phenomenon occurring around the tip at 50–60 % the chord from the leading edge. The location of the source has been determined from the conditional analysis of the Hot Wire data leading to an averaged structure exhibiting a phase shift with respect to the pressure timing. This result has been definitely confirmed by the conditional analysis of the PIV fields providing a 2D view of the most probable wall–pressure source.

Appendix A

Power-spectral-density boundary-to-field transfer function

A.1 Introduction

A turbulent boundary layer generates broadband noise as an effect of the scattering of vortical disturbances into acoustic waves. The noise due to this mechanism may be predicted either from the vortical velocity field surrounding the surface, or from the induced pressure field on the surface. The first approach – that based upon the velocity field – was outlined by Ffawcs Williams & Hall (1970), and may be easily connected to computational results, provided for instance by large eddy simulations, to be used as input (see, for instance, Moin, 2000). The second approach, that based upon the induced wall pressure, has been developed for instance in Amiet (1976) for the case of the trailing edge noise of an airfoil, and provides a prediction of the far field power spectral density of the acoustic pressure. The method has been supported by several experimental analyses (see, for instance, Roger & Moreau, 2002); however it has the disadvantage that a connection with

computational results is more difficult to address.

The objective of the paper is to present new developments regarding a formulation for the evaluation of the power spectral density of the acoustic pressure at any given point in the field in terms of the power spectral density of the transpiration velocity (this is a quantity defined in terms of the vorticity and is closely related to the *equivalent source* concept introduced by Lighthill (1958). Specifically, the formulation used allows one to obtain, in the frequency domain (Fourier transform), a matrix relationship between the transpiration velocity at a number of points on the surface of the object (those arising from the boundary–element discretization) and the pressure at given points in the irrotational region. From this, the relationship between the corresponding power spectral densities is easily obtained using the Wiener-Khintchine theorem.

The approach used here is based upon a decomposition for the analysis of the effects of the vorticity, which was introduced for aerodynamics in Morino (1990), and refined in Morino *et al.* (1999) and Morino & Bernardini (2002). The commonality between aerodynamics and aeroacoustics is addressed in Morino (2003) (which provides a synthesis of all the preceding work), and is exploited here. For incompressible flows, the formulation under consideration was presented in Morino *et al.* (2007), along with some preliminary numerical results; the comparison with experimental data is encouraging.

Here, the formulation is extended to compressible flows. For the sake of clarity, in the main body of the paper, the formulation is presented for the limited case of incompressible flows. The formulation for compressible flows, based upon that in Morino (2003), is outlined in Section A.8.

A.2 The decomposition

For the sake of completeness, in this section, we present the decomposition introduced in Morino (1990), and refined in Morino *et al.* (1999) and Morino & Bernar-

dini (2002). This formulation falls within the general class of potential–vorticity decompositions for the velocity field of the type

$$\mathbf{v} = \nabla\varphi + \mathbf{w}, \tag{A.1}$$

where $\mathbf{w}$ is any particular solution of the equation

$$\nabla \times \mathbf{w} = \boldsymbol{\zeta}. \tag{A.2}$$

with $\boldsymbol{\zeta} := \nabla \times \mathbf{v}$ denoting the vorticity field. The decomposition given in Eq. A.1 is valid for any vector field and Eq. A.2 is a necessary and sufficient condition for the validity of Eq. A.1. Indeed, Eq. A.2 is necessary, as it is easily seen by taking the curl of Eq. A.1; *vice versa*, if Eq. A.2 is satisfied, then $\nabla \times (\mathbf{v} - \mathbf{w}) = 0$ and therefore there exists a potential function φ, such that $\mathbf{v} - \mathbf{w} = \nabla\varphi$, in agreement with Eq. A.1.

The decomposition given in Eq. A.1 is quite general. Classical decompositions used in fluid dynamics, such as those by Helmholtz and Clebsch (see, e.g. Serrin, 1959), are included in Eq. A.1. The decomposition of Morino (1990) used here differs from these and has the distinguishing feature that the rotational–velocity contribution vanishes in much of the irrotational region (in all of it, for many of the cases of practical interest, in particular, for the application to attached flows of interest here). Specifically, the decomposition falls within the class of direct–integration decompositions, in which Eq. A.2 is solved by direct integration. Using the expression for the curl in curvilinear coordinates, Eq. A.2 may be rewritten as

$$J\zeta^1 = \frac{\partial w_3}{\partial \xi^2} - \frac{\partial w_2}{\partial \xi^3} \qquad J\zeta^2 = \frac{\partial w_1}{\partial \xi^3} - \frac{\partial w_3}{\partial \xi^1} \qquad J\zeta^3 = \frac{\partial w_2}{\partial \xi^1} - \frac{\partial w_1}{\partial \xi^2}, \tag{A.3}$$

where J is the Jacobian of the transformation $\mathbf{x} = \mathbf{x}(\xi^\alpha)$, ζ^j are the contravariant components of $\boldsymbol{\zeta} = \zeta^j \mathbf{g}_j$, whereas w_k are the covariant components of $\mathbf{w} = w_k \mathbf{g}^k$. This equation may be solved by choosing, arbitrarily but legitimately,

$$w_3(\xi^1, \xi^2, \xi^3) = 0. \tag{A.4}$$

Hence, recalling that $\boldsymbol{\zeta} = \mathbf{0}$ at infinity, the first two equations in Eq. A.3 may be integrated to yield the following particular solution for Eq. A.2:

$$\begin{aligned} w_1(\xi^1, \xi^2, \xi^3) &= -\int_{\xi^3}^{\infty} J\, \zeta^2(\xi^1, \xi^2, \breve{\xi}^3)\, \mathrm{d}\breve{\xi}^3 \\ w_2(\xi^1, \xi^2, \xi^3) &= \int_{\xi^3}^{\infty} J\, \zeta^1(\xi^1, \xi^2, \breve{\xi}^3)\, \mathrm{d}\breve{\xi}^3 \\ w_3(\xi^1, \xi^2, \xi^3) &= 0. \end{aligned} \tag{A.5}$$

Equation A.5 is the *key* of formulation used here.

Next, consider the direction of integration ξ^3. In the scheme used in Morino (1990), the direction of integration is somewhat aligned with the direction of the flow. On the other hand, in Morino *et al.* (1999), using a three–dimensional extension of a $C-$grid, the direction of integration ξ^3 is taken along the normal to the body surface $\mathcal{S}_{\mathsf{B}}$ and the wake mid–surface, $\mathcal{S}_{\mathsf{W}}$.[1]

It is apparent that, in either approach, for attached high–Reynolds–number flows (for which the rotational region is a very thin layer around the surface of the body), $\mathbf{w}$ obtained from Eq. A.5 vanishes in the whole irrotational region, that is, the volume $\mathcal{W}$ where $\mathbf{w} \neq \mathbf{0}$ coincides with the rotational region. Thus, recalling Eq. A.1, we have, in the whole irrotational region, $\mathbf{v} = \nabla\varphi$. Hence, the Bernoulli theorem may be used to evaluate the pressure there.

In the remainder of the paper, following Morino *et al.* (1999), we assume that the lines of integration are along the normal to the body surface $\mathcal{S}_{\mathsf{B}}$ and the wake mid-surface, $\mathcal{S}_{\mathsf{W}}$. In addition, for simplicity we assume that the ξ^3–line be normal to the surfaces $\hat{\xi}^3(\mathbf{x})$ =constant.

For instance, let $\mathbf{x} = \mathbf{p}(\xi^1, \xi^2)$ describe the surface for $\xi^3 = 0$ (specifically, a closed surface composed of the body surface $\mathcal{S}_{\mathsf{B}}$ and the two sides of the wake mid-surface, $\mathcal{S}_{\mathsf{W}}$). Choosing the coordinate ξ^3 to coincide with η (arclength along the

[1] Also, with either scheme some problems arise; these are addressed in Morino & Bernardini (2002) and Morino (2003), where a formulation that provides a compromise between the two approaches is presented.

normal, $\mathbf{n}$, to the surface $\mathbf{x} = \mathbf{p}(\xi^1, \xi^2))$, we have[2]

$$\mathbf{x}(\xi^1, \xi^2, \eta) = \mathbf{p}(\xi^1, \xi^2) + \eta \mathbf{n}(\xi^1, \xi^2). \tag{A.6}$$

Then, $\mathbf{g}_3 = \mathbf{n}$, whereas $\mathbf{g}_\alpha$ $(\alpha = 1, 2)$ is perpendicular to $\mathbf{n}$. In addition, we have $\mathbf{g}^3 = \mathbf{n}$ and $J = \|\mathbf{a}_1 \times \mathbf{a}_2\| =: \sqrt{a}$.

The fact that $\mathbf{g}_3 = \mathbf{g}^3 = \mathbf{n}$ yields that Eq. A.4 $(w_3 \xi^1, \xi^2, \eta = 0)$ implies

$$w^3(\xi^1, \xi^2, \eta) = 0. \tag{A.7}$$

In particular,

$$w^3(\xi^1, \xi^2, 0) = \mathbf{w} \cdot \mathbf{n}|_{\eta=0} = w_3(\xi^1, \xi^2, 0) = 0. \tag{A.8}$$

A.3 Incompressible–flow formulation for φ

In this section, we consider the formulation for φ (potential of the irrotational velocity contribution introduced by Eq. A.1). As mentioned above, here, for the sake of simplicity, we assume that the flow field is incompressible. In this case, we have

$$\nabla \cdot \mathbf{v} = 0. \tag{A.9}$$

Combining with Eq. A.1, one obtains

$$\nabla^2 \varphi = \Theta, \tag{A.10}$$

where, using Eq. A.7 (and hence the assumption on the coordinates used to obtain it), we have

$$\Theta := -\nabla \cdot \mathbf{w} = -\frac{1}{J} \frac{\partial}{\partial \xi^\alpha} \left(J w^\alpha \right) \tag{A.11}$$

Note that according to this equation, $\Theta = 0$ in the irrotational region $\mathbb{R}^3 \backslash \mathcal{W}$.

[2]Problems arise if the layer thickness is larger than the curvature of the surface (this is in particular true at the trailing edge. For these issues the reader is referred to Morino *et al.* (1999).

Next, consider the boundary conditions for φ over the surface of the body and at infinity. For viscous flows, the boundary condition over $\mathcal{S}_{\mathsf{B}}$ is $\mathbf{v} = \mathbf{v}_{\mathsf{B}}$, where $\mathbf{v}_{\mathsf{B}}$ is the velocity at $\mathbf{x} \in \mathcal{S}_{\mathsf{B}}$. For the potential φ, we use the normal component of this equation, $\mathbf{v} \cdot \mathbf{n} = \mathbf{v}_{\mathsf{B}} \cdot \mathbf{n}$. Thus, combining with Eq. A.1 and recalling Eq. A.8, one obtains

$$\frac{\partial \varphi}{\partial n} = \chi \qquad (\mathbf{x} \in \mathcal{S}_{\mathsf{B}}), \tag{A.12}$$

with

$$\chi := \mathbf{v}_{\mathsf{B}} \cdot \mathbf{n} \tag{A.13}$$

Note that this is formally identical to the boundary condition for potential flows, Eq. A.42.

In addition, in a frame of reference connected with the undisturbed air, we have

$$\varphi = \mathcal{O}\left(\|\mathbf{x}\|^{-1}\right), \qquad \text{at infinity.} \tag{A.14}$$

The boundary integral representation for the Poisson equation, Eq. A.10, is (see, e.g. Kress, 1989)

$$E(\mathbf{x})\varphi(\mathbf{x}) = \oint_{\mathcal{S}_{\mathsf{B}}} \left(\frac{\partial \varphi}{\partial n} G - \varphi \frac{\partial G}{\partial n} \right) \mathrm{d}\mathcal{S}(\mathbf{y}) + \int_{\mathcal{W}} \Theta \, G \, \mathrm{d}\mathcal{V}(\mathbf{y}), \tag{A.15}$$

where $G = -1/4\pi\|\mathbf{x} - \mathbf{y}\|$, whereas – we recall – $\mathcal{W}$ is the region where $\mathbf{w} \neq 0$, and finally

$$\begin{aligned} E(\mathbf{x}) &= 1 \;\; \text{for } \mathbf{x} \in \mathcal{V}_{\mathsf{F}} \\ &= \frac{1}{2} \;\; \text{for } \mathbf{x} \in \partial\mathcal{V}_{\mathsf{F}} \qquad \text{(smooth point)} \\ &= 0 \;\; \text{for } \mathbf{x} \in \mathbb{R}^3 \backslash \mathcal{V}_{\mathsf{F}}. \end{aligned} \tag{A.16}$$

Equation A.15 allows one to evaluate φ anywhere in the field, if φ and $\partial\varphi/\partial n$ over $\mathcal{S}_{\mathsf{B}}$ and Θ in $\mathcal{W}$ are known.

However, φ on $\mathcal{S}_{\mathsf{B}}$ is not known. Thus, first one must obtain an equation for evaluating φ on $\mathcal{S}_{\mathsf{B}}$. This may be obtained in the limit, as $\mathbf{x}$ tends to the surface

of the body. In this case, Eq. A.15 yields a compatibility condition between φ and $\partial\varphi/\partial n$ over $\mathcal{S}_{\mathsf{B}}$ and Θ in $\mathcal{W}$, that is, an integral equation relating φ over $\mathcal{S}_{\mathsf{B}}$ to $\partial\varphi/\partial n$ over $\mathcal{S}_{\mathsf{B}}$ and Θ in $\mathcal{W}$.

Hence, provided that $\partial\varphi/\partial n$ over $\mathcal{S}_{\mathsf{B}}$ and Θ in $\mathcal{W}$ are known, the solution for φ in the field, is obtained in two steps. In the first one, $\mathbf{x}$ denotes the generic point on the surface $\mathcal{S}_{\mathsf{B}}$. In this case, Eq. A.15 corresponds to an integral equation for φ on $\mathcal{S}_{\mathsf{B}}$. Once φ on $\mathcal{S}_{\mathsf{B}}$ has been evaluated, we consider the second step, that which yields φ in the field: now, $\mathbf{x}$ denotes a specific point in the field, and Eq. A.15 corresponds to an integral representation for φ in $\mathcal{V}_{\mathsf{F}}$, in terms of $\partial\varphi/\partial n$ over $\mathcal{S}_{\mathsf{B}}$ and Θ in $\mathcal{W}$.

A.4 Transpiration velocity

An expression for Eq. A.15 that closely related to the Lighthill (1958) equivalent–source approach may be obtained through an integration by parts of the field integral. For simplicity, we address first the case in which there is no elongated wake, and then extend this to the case of elongated wake.

A.4.1 Formulation for flows without elongated wakes

For simplicity, consider first a steady flow around a doubly–symmetric convex body with zero angles of attack. In this case, the extension of the wake is somewhat limited, and we may assume the coordinate η to be in the direction of the normal to $\mathcal{S}_{\mathsf{B}}$ (see Eq. A.6).

Then, combining Eqs. A.12, A.15 and A.18, and integrating by parts the field term in Eq. A.15, yields

$$E(\mathbf{x})\varphi(\mathbf{x}) = \oint_{\mathcal{S}_{\mathsf{B}}} \left[(\chi + \sigma_{\mathsf{B}})\, G - \varphi \frac{\partial G}{\partial n} \right] \mathrm{d}\mathcal{S}(\mathbf{y}) + \int_{\mathcal{W}} \Theta' \frac{\partial G}{\partial \eta} \mathrm{d}\mathcal{V}(\mathbf{y}), \tag{A.17}$$

with

$$\Theta' = \frac{1}{\sqrt{a}} \int_{\eta}^{\infty} \sqrt{a}\Theta \mathrm{d}\breve{\eta}, \tag{A.18}$$

whereas (see Eq. A.11)

$$\sigma_{\mathsf{B}}(\xi^1,\xi^2) := \Theta'(\xi^1,\xi^2,0) = \frac{1}{\sqrt{a_0}}\int_0^\infty \sqrt{a}\Theta \mathrm{d}\eta = \frac{-1}{\sqrt{a_0}}\frac{\partial}{\partial \xi^\alpha}\int_0^\infty J w^\alpha \mathrm{d}\eta. \quad \text{(A.19)}$$

It may be worth noting that the above procedure is equivalent to 'extracting' the monopole–layer contribution from the volume integral. Indeed, if $\mathbf{x}$ is very distant from the region $\mathcal{W}$, in the volume integral in Eq. A.15 G may be assumed to be constant across the layer to yield

$$\int_{\mathcal{W}} \Theta\, G\, \mathrm{d}\mathcal{V}(\mathbf{y}) \approx \oint_{\mathcal{S}_{\mathsf{B}}} \sigma_{\mathsf{B}}\, G\, \mathrm{d}\mathcal{S}(\mathbf{y}), \quad \text{(A.20)}$$

with σ_{B} given by Eq. A.19. Stated in different terms, in Eq. A.17 the σ_{B}–term is a monopole layer, whereas the volume integral behaves like a dipole, specifically, it vanishes like $\|\mathbf{x}\|^{-2}$ at infinity.

It is apparent that, if we neglect the volume integral, the solution φ (and hence the velocity $\mathbf{v}$ in $\mathbb{R}^3\backslash\mathcal{W}$, that is, in the region where $\mathbf{w} = \mathbf{0}$) coincides with that of a potential flow with the boundary condition for a permeable surface has a flow velocity equal to σ_{B} (Eq. A.43). For this reason, the term σ_{B} will be referred to as the *transpiration velocity.* As shown in Morino *et al.* (1999), the expression for the transpiration velocity is very close to the equivalent source term of Lighthill (1958).

Again, the solution is obtained in two steps, as indicated at the end of Section A.3

A.4.2 Formulation for flows with elongated wakes

As already mentioned, above we have assumed that the extension of the wake is somewhat limited. However, in the typical flows of interest, the vorticity in the boundary layer is convected downstream by the flow, thereby generating a thin layer of vorticity emanating from the trailing edge, called the wake. For symmetric configurations, the vortical region of the wake is limited to about one chord length (thus, the formulation presented above is applicable in such cases). However, for

three-dimensional lifting problems it is known that, for steady flows, after a few chord-lengths, the vortices are essentially aligned with the flow and extend to infinity (in the limit, as the thickness goes to zero, one recovers the formulation for quasi–potential flows (that is, flows that are potential everywhere, except for a surface of discontinuity which emanates from the trailing edge and is called the potential wake; for a relatively recent review, the reader is referred to Morino (2003); for the sake of completeness, the methodology is briefly outlined in Section A.7). It is apparent that, for very thin wakes, the flow outside the rotational layer is approximated by the quasi–potential solution. Thus, it is impossible to find a continuation, $\mathbf{v}_{\mathsf{C}}$, of the outer–flow velocity that is potential and solenoidal everywhere;[3] the best we can hope for is that $\mathbf{v}_{\mathsf{C}}$ be quasi-potential. In this section, we discuss the extension of the above formulation to the analysis of attached or slightly separated high–Reynolds–number flows around lifting bodies (e.g. a wing).

In order to analyze these types of problems, let the surface $\eta = 0$ coincide with limiting case of a surface that surrounds body and wake (that is, the union of $\mathcal{S}_{\mathsf{B}}$ and of the two sides of the wake mid-surface, $\mathcal{S}_{\mathsf{W}}$). In this case, one obtains that, in general, using Eq. A.5 yields a vortical velocity $\mathbf{w}$ that has a tangential discontinuity across $\mathcal{S}_{\mathsf{W}}$. This discontinuity does not exist in the actual velocity field, since $\mathbf{v}$ is continuous at $\mathcal{S}_{\mathsf{W}}$. Recalling Eq. A.1, one may infer that the tangential discontinuity of $\mathbf{w}$ must be compensated for by a discontinuity of φ (these discontinuities correspond to two equal and opposite layers of vorticity).

Thus, we have to take into account that $\mathcal{S}_{\mathsf{W}}$ is a surface of discontinuity for both $\mathbf{w}$ and φ. In order to avoid having to deal with the vortex layer due to the discontinuity of $\mathbf{w}$, it is convenient to write the boundary integral representation for a closed surface that is infinitesimally close to the body and the wake surface,

[3]Note that, even in unsteady two–dimensional flows, the analytic extension of the outer potential–flow solution into the vortical region (boundary layer and wake) yields different solutions for $\nabla\varphi$ if we approach the wake mid–surface $\mathcal{S}_{\mathsf{W}}$ from the two opposite sides.

$\mathcal{S}_{\mathsf{W}}$. This yields

$$
\begin{aligned}
E(\mathbf{x})\varphi(\mathbf{x}) &= \oint_{\mathcal{S}_{\mathsf{B}}} \left(\chi G - \varphi \frac{\partial G}{\partial n}\right) \mathrm{d}\mathcal{S}(\mathbf{y}) - \int_{\mathcal{S}_{\mathsf{W}}} \Delta\varphi \frac{\partial G}{\partial n} \mathrm{d}\mathcal{S}(\mathbf{y}) \\
&+ \int_{\mathcal{V}} \Theta G \mathrm{d}\mathcal{V}(\mathbf{y}), \qquad \text{(A.21)}
\end{aligned}
$$

where $\Delta\varphi$ denotes the discontinuity of φ across $\mathcal{S}_{\mathsf{W}}$ (if $\Delta\varphi := \varphi_2 - \varphi_1$, the unit normal to $\mathcal{S}_{\mathsf{W}}$ points from side 1 to side 2 of $\mathcal{S}_{\mathsf{W}}$).

Proceeding as in the preceding subsection (that is, integrating by parts the volume integral) yields

$$
\begin{aligned}
E(\mathbf{x})\varphi(\mathbf{x}) &= \oint_{\mathcal{S}_{\mathsf{B}}} \left((\chi + \sigma_{\mathsf{B}})\, G - \varphi \frac{\partial G}{\partial n}\right) \mathrm{d}\mathcal{S}(\mathbf{y}) \\
&+ \int_{\mathcal{S}_{\mathsf{W}}} \left(\sigma_{\mathsf{W}}\, G - \Delta\varphi \frac{\partial G}{\partial n}\right) \mathrm{d}\mathcal{S}(\mathbf{y}) \\
&+ \int_{\mathcal{V}} \Theta' \frac{\partial G}{\partial \eta} \mathrm{d}\mathcal{V}(\mathbf{y}), \qquad \text{(A.22)}
\end{aligned}
$$

with $\sigma_{\mathsf{W}} := \sigma_1 + \sigma_2$, where σ_1 and σ_2 are given, individually, by Eq. A.19.[4]

In addition, in order to relate $\Delta\varphi$ to φ on the body, one may use the quasi–potential flow conditions, on the wake (Eq. A.48) and trailing edge (Eq. A.49).

As in the preceding case, the solution is obtained in two steps, as indicated at the end of Section A.3

A.5 Numerical formulation

In order to show how the present formulation may be used to evaluate the power spectral density of the pressure at a given point from the power spectral density of the transpiration velocity σ_{B}, it is convenient to discretize the problem.

Consider Eq. A.22. For the sake of simplicity, we neglect the contribution of the volume integral in Eq. A.22. Let $\mathcal{S}_{\mathsf{B}}$ be divided into N_{B} surface elements,

[4]Recalling the geometry used, we see that $\eta \in (0, \infty)$ represents either the region above the wake or that below, of course for different values of ξ^{α}).

$\mathcal{S}_j$ $(j = 1, \ldots, N_{\mathsf{B}})$, and $\mathcal{S}_{\mathsf{W}}$ into N_{W} surface elements, $\mathcal{S}_n$ $(n = 1, \ldots, N_{\mathsf{B}})$. Next, introduce a piece–wise constant approximation for $\varphi(\mathbf{x})$: $\varphi(\mathbf{x}) = \varphi_j$, for $\mathbf{x} \in \mathcal{S}_j$. A similar approximation is used for χ, σ_{B}, σ_{W}, and $\Delta\varphi$. This yields

$$\begin{aligned} E(\mathbf{x})\,\varphi(\mathbf{x}) &= \sum_{j=1}^{N_{\mathsf{B}}} B_j^{\mathsf{B}}(\mathbf{x})\left(\chi_j + \sigma_j^{\mathsf{B}}\right) + \sum_{j=1}^{N_{\mathsf{B}}} C_j^{\mathsf{B}}(\mathbf{x})\,\varphi_j \\ &+ \sum_{n=1}^{N_{\mathsf{W}}} B_n^{\mathsf{W}}(\mathbf{x})\,\sigma_n^{\mathsf{W}} + \sum_{n=1}^{N_{\mathsf{W}}} C_n^{\mathsf{W}}(\mathbf{x})\,\Delta\varphi_n, \end{aligned} \tag{A.23}$$

where

$$\begin{aligned} B_j^{\mathsf{B}}(\mathbf{x}) &= \int_{\mathcal{S}_j^{\mathsf{B}}} G \mathrm{d}\mathcal{S}(\mathbf{y}), & C_j^{\mathsf{B}}(\mathbf{x}) &= -\int_{\mathcal{S}_j^{\mathsf{B}}} \frac{\partial G}{\partial n} \mathrm{d}\mathcal{S}(\mathbf{y}), \\ B_n^{\mathsf{W}}(\mathbf{x}) &= \int_{\mathcal{S}_n^{\mathsf{W}}} G \mathrm{d}\mathcal{S}(\mathbf{y}), & C_n^{\mathsf{W}}(\mathbf{x}) &= -\int_{\mathcal{S}_n^{\mathsf{W}}} \frac{\partial G}{\partial n} \mathrm{d}\mathcal{S}(\mathbf{y}). \end{aligned} \tag{A.24}$$

Also (see Eq. A.48),

$$\Delta\varphi_n(t) = \Delta\varphi_n^{\mathsf{TE}}(t - \theta_n^{\mathsf{c}}), \tag{A.25}$$

where θ_n^{c} is the convection time required for a wake point to be convected from the trailing edge point $\mathbf{x}_n^{\mathsf{TE}}$ to the wake point $\mathbf{x}_n^{\mathsf{W}}$. In addition,

$$\Delta\varphi_n^{\mathsf{TE}}(t) = \sum_{j=1}^{N_{\mathsf{B}}} S_{nj}\,\varphi_j(t), \tag{A.26}$$

where S_{nj} is suitable matrix, introduced to implement the trailing–edge condition, Eq. A.49.

In the following, we consider a wing in uniform translation. Then, χ is time independent. Hence, we separate the steady–state and the unsteady–state problem. Then, taking the Fourier transform of the unsteady portion of Eq. A.23, one obtains

$$E_k\hat{\varphi}_k = \sum_{j=1}^{N_{\mathsf{B}}} B_{kj}^{\mathsf{B}}\,\hat{\sigma}_j^{\mathsf{B}} + \sum_{j=1}^{N_{\mathsf{B}}} C_{kj}^{\mathsf{B}}\,\hat{\varphi}_j + \sum_{n=1}^{N_{\mathsf{W}}} B_{kn}^{\mathsf{W}}\,\hat{\sigma}_n^{\mathsf{W}} + \sum_{n=1}^{N_{\mathsf{W}}} C_{kn}^{\mathsf{W}}\,\Delta\hat{\varphi}_n, \tag{A.27}$$

where, for instance $B^{\mathsf{B}}_{kj} = B^{\mathsf{B}}_{j}(\mathbf{x}_k)$, whereas, for instance, $\hat{\varphi}_k$ denote the Fourier transform of the unsteady portion of φ_k:

$$\hat{\varphi}_k = \mathfrak{F}\left(\varphi_k|_{\mathsf{unsteady}}\right) \tag{A.28}$$

In addition, combining Eqs. A.25 and A.26, and taking the Fourier transform, one obtains

$$\Delta\hat{\varphi}_n = e^{-\imath\omega\theta^{\mathsf{C}}_n}\,\Delta\hat{\varphi}^{\mathsf{TE}}_n = e^{-\imath\omega\theta^{\mathsf{C}}_n}\sum_{j=1}^{N_{\mathsf{B}}} S_{nj}\hat{\varphi}_j \tag{A.29}$$

Next, recall that – as pointed out at the end of Section A.3 – the solution for φ in the field, with χ and Θ prescribed, is obtained in two steps. In the first one, $\mathbf{x}$ denotes the generic point on the surface $\mathcal{S}_{\mathsf{B}}$; in this case, Eq. A.15 corresponds to an integral equation for φ on $\mathcal{S}_{\mathsf{B}}$. In the second step, $\mathbf{x}$ denotes a specific point in the field, and Eq. A.15 corresponds to an integral representation for φ in $\mathcal{V}_{\mathsf{F}}$.

Consider the first step (integral equation). In this case, the collocation points $\mathbf{x}_k$ are located on the surface $\mathcal{S}_{\mathsf{B}}$: $\mathbf{x}_k \in \mathcal{S}_{\mathsf{B}}$ $(k = 1, \ldots, N_{\mathsf{B}})$. Thus, φ on the left hand side is evaluated on $\mathcal{S}_{\mathsf{B}}$, whereas $E_k = 1/2$. Then, Eq. A.27 yields

$$\left[\frac{1}{2}\mathsf{I} - \mathsf{C}_{\mathsf{BB}} - \mathsf{C}_{\mathsf{BW}}\mathsf{DS}\right]\hat{\boldsymbol{\varphi}}_{\mathsf{B}} = \mathsf{B}_{\mathsf{BB}}\hat{\boldsymbol{\sigma}}_{\mathsf{B}} + \mathsf{B}_{\mathsf{BW}}\hat{\boldsymbol{\sigma}}_{\mathsf{W}} \tag{A.30}$$

where, for instance, the elements of the matrix C_{BB} are given by $C^{\mathsf{B}}_{kj} = C^{\mathsf{B}}_{j}(\mathbf{x}_k)$ $(k = 1, \ldots, N_{\mathsf{B}})$, where $\mathbf{x}_k$ is located on $\mathcal{S}_{\mathsf{B}}$. In addition, the delay matrix D is given by

$$\mathsf{D} = \mathrm{Diag}\left[e^{-\imath\omega\theta^{\mathsf{C}}_n}\right] \tag{A.31}$$

Next, consider the second step (integral representation). In this case, the collocation points $\mathbf{x}_k$ are located in the fluid volume, $\mathcal{V}_{\mathsf{F}}$: $\mathbf{x}_k \in \mathcal{V}_{\mathsf{F}}$ $(k = 1, \ldots, N_{\mathsf{F}}$, with N_{F} arbitrary). Thus, φ on the left hand side is evaluated in $\mathcal{V}_{\mathsf{F}}$, and $E_k = 1$. Then, Eq. A.27 yields

$$\hat{\boldsymbol{\varphi}}_{\mathsf{F}} = \left(\mathsf{C}_{\mathsf{FB}} + \mathsf{C}_{\mathsf{FW}}\mathsf{DS}\right)\hat{\boldsymbol{\varphi}}_{\mathsf{B}} + \mathsf{B}_{\mathsf{FB}}\hat{\boldsymbol{\sigma}}_{\mathsf{B}} + \mathsf{B}_{\mathsf{FW}}\hat{\boldsymbol{\sigma}}_{\mathsf{W}} \tag{A.32}$$

with apparent definition of the symbols: for instance, the elements of the matrix C_{FB} are given by $C^{\mathsf{B}}_{kj} = C^{\mathsf{B}}_j(\mathbf{x}_k)$ $(k = 1, \ldots, N_{\mathsf{F}})$, where $\mathbf{x}_k$ is located in $\mathcal{V}_{\mathsf{F}}$.

Next, consider the pressure in the region $\mathbb{R}^3 \backslash \mathcal{W}$, where $\mathbf{w} = \mathbf{0}$. In this case $\mathbf{v} = \nabla\varphi$, and then the Bernoulli theorem for potential flows, Eq. A.40, applies. This may be linearized to yield, $p - p_\infty = -\rho\dot{\varphi}$, or, in the body frame of reference, $p - p_\infty = -\rho(\dot{\varphi} + U_\infty \partial\varphi/\partial x)$. Thus, we have, taking the Fourier transform

$$\hat{\mathsf{p}} = \imath\omega\rho\hat{\boldsymbol{\varphi}}_{\mathsf{F}} + \rho U_\infty \left(\mathsf{C}'_{\mathsf{FB}} + \mathsf{C}'_{\mathsf{FW}}\mathsf{DS}\right)\hat{\boldsymbol{\varphi}}_{\mathsf{B}} + \rho U_\infty \left(\mathsf{B}'_{\mathsf{FB}}\hat{\boldsymbol{\sigma}}_{\mathsf{B}} + \mathsf{B}'_{\mathsf{FW}}\hat{\boldsymbol{\sigma}}_{\mathsf{W}}\right), \tag{A.33}$$

where, for instance,

$$\mathsf{C}'_{\mathsf{FB}} = \left[\frac{\partial}{\partial x} C^{\mathsf{B}}_j(\mathbf{x})\right]_{\mathbf{x}=\mathbf{x}_k} \tag{A.34}$$

with $\mathbf{x}_k \in \mathbb{R}^3 \backslash \mathcal{W}$.

It is apparent that using Eqs. A.30 and A.32 to express $\hat{\boldsymbol{\varphi}}_{\mathsf{B}}$ and $\hat{\boldsymbol{\varphi}}_{\mathsf{F}}$ in terms of $\hat{\boldsymbol{\sigma}}_{\mathsf{B}}$ and $\hat{\boldsymbol{\sigma}}_{\mathsf{W}}$, and substituting into Eq. A.33, one obtains an equation relating $\hat{\mathsf{p}}$ to $\hat{\boldsymbol{\sigma}}_{\mathsf{B}}$ and $\hat{\boldsymbol{\sigma}}_{\mathsf{W}}$, as

$$\hat{\mathsf{p}} = \mathsf{H}_{\mathsf{B}}\hat{\boldsymbol{\sigma}}_{\mathsf{B}} + \mathsf{H}_{\mathsf{W}}\hat{\boldsymbol{\sigma}}_{\mathsf{W}} = \mathsf{H}\hat{\boldsymbol{\sigma}} \tag{A.35}$$

where, using partitioned matrix notations, $\mathsf{H} = [\mathsf{H}_{\mathsf{B}}|\mathsf{H}_{\mathsf{W}}]$ and $\hat{\boldsymbol{\sigma}}^{\mathsf{T}} = [\hat{\boldsymbol{\sigma}}^{\mathsf{T}}_{\mathsf{B}}|\hat{\boldsymbol{\sigma}}^{\mathsf{T}}_{\mathsf{W}}]$.

A.6 Power–spectral–density analysis

In this section, we use the fact that, for the Wiener-Khintchine theorem, the power spectral density S_u of a function $u(t)$ may be expressed as

$$\mathsf{S}_u = \lim_{T\to\infty} |\hat{u}_T|^2 \tag{A.36}$$

where $\hat{u}_T$ denotes the Fourier transform of $u_T(t)$, where $u_T(t) = u(t)$ for $t \in (-T, T)$ and $u(t) = 0$ otherwise:

$$\hat{u}_T(\omega) := \mathfrak{F}[u_T(t)] := \int_{-T}^{T} u(t)e^{-\imath\omega t}\mathrm{d}t \tag{A.37}$$

For a vector function $\mathsf{v}(t)$, the power spectral density S_v is a matrix, which may be expressed as (still for the Wiener-Khintchine theorem)

$$\mathsf{S}_\mathsf{v} = \lim_{T\to\infty} \hat{\mathsf{v}}_T^* \hat{\mathsf{v}}_T^\mathsf{T} \tag{A.38}$$

where * denotes complex conjugate.

Using Eq. A.35, we have

$$\mathsf{S}_\mathsf{p} = \mathsf{H}^* \mathsf{S}_\sigma \mathsf{H}^\mathsf{T} \tag{A.39}$$

which is the desired relationship between the power spectral density S_p of the pressure at N_v arbitrary points in the region $\mathbb{R}^3 \backslash \mathcal{W}$ and the power spectral density matrix, S_σ, of the transpiration velocity at N_B points on $\mathcal{S}_\mathsf{B}$.

Equation A.39 is the desired relationship relating the power spectral density of the pressure at N_F arbitrary points in the field to the power spectral density of σ_B and σ_W at the center of the elements on $\mathcal{S}_\mathsf{B}$ and $\mathcal{S}_\mathsf{W}$.

A.7 Quasi–potential flows

For the sake of completeness, in this section, we summarize the theory and boundary integral formulation of incompressible quasi–potential flows (that is, flows in the presence of a zero–thickness vortex layer; for details and for the extension to compressible flows (see Morino, 2003)).

In order to facilitate the discussion for bodies in arbitrary motion, we use a frame of reference rigidly connected with the undisturbed air. The flow is assumed to be incompressible, inviscid, and initially irrotational. Then, applying the Kelvin theorem yields that the flow is at all times quasi–potential, that is, by definition, potential at all points, with the possible exception of the points emanating from the trailing edge (*wake*), since – for these – the Kelvin theorem is not applicable. Hence, except for the wake points, we have $\mathbf{v} = \nabla\phi$. Then, the Euler equation admits a first integral, namely the Bernoulli theorem

$$\dot{\phi} + \frac{1}{2}v^2 + p/\rho = p_\infty/\rho \tag{A.40}$$

Also, combining $\mathbf{v} = \nabla\phi$ with the continuity equation for incompressible flows, $\nabla \cdot \mathbf{v} = 0$, yields

$$\nabla^2\phi = 0 \qquad (\mathbf{x} \ \text{ outside } \ \mathcal{S}_{\mathsf{BW}}), \tag{A.41}$$

where $\mathcal{S}_{\mathsf{BW}}$ denotes a surface that surrounds the volume $\mathcal{V}_{\mathsf{B}}$ of the body as well as a thin layer $\mathcal{V}_{\mathsf{W}}$ that includes the wake surface $\mathcal{S}_{\mathsf{W}}$.

Next, consider the boundary condition on the body. If the surface is impermeable, the boundary condition is $(\mathbf{v} - \mathbf{v}_{\mathsf{B}}) \cdot \mathbf{n} = 0$, and yields

$$\frac{\partial\phi}{\partial n} = \chi \qquad (\mathbf{x} \in \mathcal{S}_{\mathsf{B}}), \tag{A.42}$$

where $\chi = \mathbf{v}_{\mathsf{B}} \cdot \mathbf{n}$. On the other hand, if the surface is permeable (such as a nacelle inlet), the boundary condition is $(\mathbf{v} - \mathbf{v}_{\mathsf{B}}) \cdot \mathbf{n} = \sigma_B$ (where σ_B is the velocity of the flow through $\mathcal{S}_B$), and the boundary condition becomes

$$\frac{\partial\phi}{\partial n} = \chi + \sigma_B \qquad (\mathbf{x} \in \mathcal{S}_{\mathsf{B}}), \tag{A.43}$$

In addition, in the air frame of reference used here, at infinity we have $\mathbf{v} = \mathcal{O}(\|\mathbf{x}\|^{-2})$, or

$$\phi = \mathcal{O}(\|\mathbf{x}\|^{-1}) \qquad \text{at infinity.} \tag{A.44}$$

Moreover, the boundary conditions on the wake are [from the principles of conservation of mass and momentum (see Morino, 2003; Morino & Bernardini, 2002, for details)]: $\mathbf{v} \cdot \mathbf{n} = \mathbf{v}_{\mathsf{W}} \cdot \mathbf{n}$ and $\Delta p = 0$. The first yields

$$\Delta\left(\frac{\partial\phi}{\partial n}\right) = 0 \qquad (\mathbf{x} \in \mathcal{S}_{\mathsf{W}}), \tag{A.45}$$

whereas from the second one, using the Bernoulli theorem, Eq. A.40, one obtains

$$\frac{D_{\mathsf{W}}}{Dt}\Delta\phi = 0 \qquad (\mathbf{x} \in \mathcal{S}_{\mathsf{W}}), \tag{A.46}$$

where $\Delta\phi = \phi_2 - \phi_1$ (with 1 and 2 denoting the two sides of $\mathcal{S}_{\mathsf{W}}$), whereas

$$\frac{D_{\mathsf{W}}}{Dt} = \frac{\partial}{\partial t} + \mathbf{v}_{\mathsf{W}} \cdot \nabla, \tag{A.47}$$

with $\mathbf{v}_{\mathsf{W}} = \frac{1}{2}(\mathbf{v}_1 + \mathbf{v}_2)$. Note that D_{W}/Dt is the substantial derivative following a wake point, $\mathbf{x}_{\mathsf{W}}$, which by definition is a point having velocity $\mathbf{v}_{\mathsf{W}}$. Thus, Eq. A.46 implies that $\Delta\phi$ remains constant following a wake point $\mathbf{x}_{\mathsf{W}}$, and equals the value it had when $\mathbf{x}_{\mathsf{W}}$ left the trailing edge, or

$$\Delta\phi(\mathbf{x}_{\mathsf{W}}, t) = \Delta\phi(\mathbf{x}_{\mathsf{TE}}, t - \theta_{\mathsf{C}}), \tag{A.48}$$

where $\mathbf{x}_{\mathsf{TE}}$ is the trailing–edge point from which $\mathbf{x}_{\mathsf{W}}$ originates, whereas $\theta_{\mathsf{C}} = \theta_{\mathsf{C}}(\mathbf{x}_{\mathsf{W}}, t)$ is the convection time from $\mathbf{x}_{\mathsf{TE}}$ to $\mathbf{x}_{\mathsf{W}}$ (typically, one uses the approximation $\theta_{\mathsf{C}} = (x_{\mathsf{W}} - x_{\mathsf{TE}})/U_\infty$).

Finally, one needs a boundary condition at the trailing edge. The value of $\Delta\phi$ at the trailing edge is obtained by imposing the trailing–edge condition that no vortex filament exists at the trailing edge (Joukowski hypothesis); this implies that the value of $\Delta\phi$ on the wake and the value of $\Delta\phi$ on the body are equal at the trailing edge[5]

$$\lim_{\mathbf{x}_{\mathsf{W}} \to \mathbf{x}_{\mathsf{TE}}} \Delta\phi(\mathbf{x}_{\mathsf{W}}) = \lim_{\mathbf{x}_2 \to \mathbf{x}_{\mathsf{TE}}} \phi(\mathbf{x}_2) - \lim_{\mathbf{x}_1 \to \mathbf{x}_{\mathsf{TE}}} \phi(\mathbf{x}_1), \tag{A.49}$$

where 1 and 2 here denote the sides of the wing surface corresponding to the sides 1 and 2 of the wake, respectively.

Next, consider the boundary integral representation for ϕ in the region outside the surface $\mathcal{S}_{\mathsf{BW}}$ (introduced in Eq. A.41). This is given by (see, e.g. Kress, 1989))

$$\phi(\mathbf{x}) = \oint_{\mathcal{S}_{\mathsf{BW}}} \left(\frac{\partial \phi}{\partial n} G - \phi \frac{\partial G}{\partial n} \right) \mathrm{d}\mathcal{S}(\mathbf{y}), \tag{A.50}$$

where $G = 1/4\pi\|\mathbf{y} - \mathbf{x}\|$ denotes the three–dimensional fundamental solution for the Laplace equation and the normal $\mathbf{n}$ is outwardly directed.

Next, let the (closed) surface $\mathcal{S}'_{\mathsf{W}}$ that surrounds the wake become infinitesimally close to the (open) surface of the wake, $\mathcal{S}_{\mathsf{W}}$. In this process, the closed surface $\mathcal{S}'_{\mathsf{W}}$ surrounding the wake is replaced by the two sides of the wake surface, $\mathcal{S}_{\mathsf{W}}$. Let $\mathbf{n}$

[5]The trailing edge boundary condition is quite subtle and the reader is referred to Morino & Bernardini (2002), where these issues are explored in details.

on $\mathcal{S}_{\mathsf{W}}$ denote the normal pointing from side 1 to side 2 of $\mathcal{S}_{\mathsf{W}}$. In the limit, one obtains, using Eq. A.45,

$$\phi(\mathbf{x}) = \oint_{\mathcal{S}_{\mathsf{B}}} \left(\frac{\partial \phi}{\partial n} G - \phi \frac{\partial G}{\partial n} \right) \mathrm{d}\mathcal{S}(\mathbf{y}) - \int_{\mathcal{S}_{\mathsf{W}}} \Delta\phi \, \frac{\partial G}{\partial n} \, \mathrm{d}\mathcal{S}(\mathbf{y}), \tag{A.51}$$

where $\Delta\phi = \phi_2 - \phi_1$, whereas $\mathcal{S}_{\mathsf{B}}$ is the (closed) surface of the body and $\mathcal{S}_{\mathsf{W}}$ is the (open) surface of the wake (with the normal pointed from side 1 to side 2).

A.8 Compressible flows

Combining the Navier–Stokes equations with $\mathrm{d}h = \vartheta \mathrm{d}S + \mathrm{d}p/\rho$, and $D\mathbf{v}/Dt = \partial\mathbf{v}/\partial t + \frac{1}{2}\mathrm{grad}v^2 + \boldsymbol{\zeta} \times \mathbf{v}$, one obtains

$$\frac{\partial \mathbf{v}}{\partial t} + \mathrm{grad}\frac{v^2}{2} + \boldsymbol{\zeta} \times \mathbf{v} = -\mathrm{grad}h + \vartheta \mathrm{grad}S + \frac{1}{\rho}\mathrm{Div}\mathbf{V}, \tag{A.52}$$

Combining Eqs. (A.1) and (A.52), and setting

$$\mathbf{d} = \frac{\partial \mathbf{w}}{\partial t} + \boldsymbol{\zeta} \times \mathbf{v} - \vartheta \mathrm{grad}S - \frac{1}{\rho}\mathrm{Div}\mathbf{V}, \tag{A.53}$$

yields $\mathrm{grad}(\dot{\varphi} + \frac{v^2}{2} + h) + \mathbf{d} = 0$. This implies $\mathrm{curl}\mathbf{d} = 0$. Hence, there exists $\varpi(\mathbf{x}) = \int_{\infty}^{\mathbf{x}} \mathbf{d}(\mathbf{y}) \cdot \mathrm{d}\mathbf{y}$ (with path–independent integral), such that $\mathbf{d} = \mathrm{grad}\varpi$. Combining the above equations [$\mathrm{grad}(\dot{\varphi} + \frac{v^2}{2} + h) + \mathbf{d} = 0$ and $\mathbf{d} = \mathrm{grad}\varpi$] yields, in the air frame, a generalized Bernoullian theorem,

$$\dot{\varphi} + \frac{v^2}{2} + h + \varpi = h_\infty, \tag{A.54}$$

an extension of those considered in Serrin (1959) (pp. 153, 168, 260, 261). Combining this equation with the non–conservative form of the continuity equation, and using the equation of state $\rho = \rho(h, S)$, as well as $a^2 := \partial p/\partial\rho|_S = \rho\partial h/\partial\rho|_S$ (isentropic speed of sound), and noting that for ideal gases $D\rho/DS|_h = -\rho/R$ (Morino, 1985, p. 4.9, Eq. 4.A.19), one obtains

$$\begin{aligned} \nabla^2\varphi + \mathrm{div}\mathbf{w} &= -\frac{1}{\rho}\frac{D\rho}{Dt} = -\frac{1}{a^2}\frac{Dh}{Dt} + \frac{1}{R}\frac{DS}{Dt} \\ &= \frac{1}{a^2}\frac{D}{Dt}\left(\dot{\varphi} + \frac{v^2}{2} + \varpi\right) + \frac{1}{R}\frac{DS}{Dt}. \end{aligned} \tag{A.55}$$

In order to identify the relevant terms at infinity (i.e. the linear terms in φ, since $\mathbf{w}$ vanishes exponentially at infinity), note that $\mathrm{Div}\mathbf{V} = (\lambda + 2\mu)\nabla^2 \mathrm{grad}\varphi + h.o.t.$, where $h.o.t.$ denotes higher order terms. Therefore, $\varpi = -\vartheta_\infty S - \nu_1 \nabla^2 \varphi + h.o.t.$, where $\nu_1 = (\lambda + 2\mu)/\rho_\infty$ (note that $\nu_1 = \frac{4}{3}\nu$ if the bulk viscosity coefficient vanishes, i.e. if $3\lambda + 2\mu = 0$). Hence, $h = h_\infty - \partial\varphi/\partial t + \vartheta_\infty S + \nu_1 \nabla^2 \varphi + h.o.t.$ In addition (recalling $h = c_p \vartheta$), $\rho_\infty \vartheta_\infty \partial S/\partial t = -\mathrm{div}\mathbf{q} + h.o.t. = \kappa \nabla^2 h/c_p + h.o.t.$. Next, we assume that $Pr = 1/(2 + \lambda/\mu)$ [for zero bulk viscosity, this means $Pr = 3/4$, which is the diatomic–gas value, Serrin (1959), p. 239]. Eliminating S between Bernoulli's theorem and the entropy equation and integrating yields $h = h_\infty - \partial\varphi/\partial t + h.o.t.$. Combining and recalling that $a^2 = \gamma R \vartheta$, one obtains

$$\nabla^2 \varphi - \frac{1}{c^2}\frac{\partial^2 \varphi}{\partial t^2} = \Theta, \tag{A.56}$$

where $c = a_\infty$, $\nu_2 = \gamma \nu_1/2$, whereas σ comprises all the so–called source terms (including the linear term $2\nu_2 \nabla^2 \dot{\varphi}$, which in aeroacoustics is typically included in the source terms).

In a body frame of reference (that is, a frame that moves with velocity $-U_\infty \mathbf{i}$ with respect to the undisturbed air), we have

$$\nabla^2 \varphi - \frac{1}{c^2}\left(\frac{\partial}{\partial t} + U_\infty \frac{\partial}{\partial t}\right)\varphi = \Theta, \tag{A.57}$$

The boundary integral representation in this case is

$$E(\check{\mathbf{x}})\varphi(\check{\mathbf{x}}, t) = \oint_{\check{\mathcal{S}}_{\mathsf{B}}} \left[\frac{\partial \varphi}{\partial \check{n}}\check{G} - \varphi \frac{\partial \check{G}}{\partial \check{n}} + \dot{\varphi}\check{G}\frac{\partial \hat{\theta}}{\partial \check{n}}\right]^{\check{\theta}} \mathrm{d}\check{\mathcal{S}}(\check{\mathbf{y}}) + \int_{\check{\mathcal{V}}_{\mathsf{F}}} \left[\check{G}\Theta\right]^{\check{\theta}} \mathrm{d}\check{\mathcal{V}}(\check{\mathbf{y}}) \tag{A.58}$$

where $\check{}$ denotes the Prandtl–Glauert space, having coordinates $\check{x}_1 = x_1/\beta$, $\check{x}_2 = x_2$ and $\check{x}_3 = x_3$; in addition, $\check{G} = -1/4\pi\check{r}$, with $\check{r} = \|\check{\mathbf{x}} - \check{\mathbf{y}}\|$, and $[...]^{\check{\theta}} = [...]_{\tau = t - \check{\theta}}$, where $\check{\theta} = [M(\check{y}_1 - \check{x}_1) + \check{r}]/\beta c$, whereas $\hat{\theta} = [M(\check{x}_1 - \check{y}_1) + \check{r}]/\beta c$.

This formulation may be treated akin to that for incompressible flows. In particular, the approximation used in Eq. A.20 may be used to approximate the volume with a surface integral, thereby defining the transpiration velocity for unsteady compressible flows. The extension of the formulation to include elongated

wakes is conceptually identical to that for incompressible flows. The numerical formulation is also conceptually identical.

Appendix B

Collection of the main pubblications

Tip Leakage Experiment - Part One: Aerodynamic And Acoustic Measurements

Julien Grilliat* and Marc C. Jacob†

Centre Acoustique du LMFA, UMR CNRS 5509,

Ecole Centrale de Lyon - University Claude-Bernard Lyon I, F-69134 Ecully Cedex, France

Roberto Camussi‡ and Giovanni Caputi - Gennaro§

Mechanical and Industrial Engineering Dept. (DIMI),

University 'Roma 3', Rome, I-00146, Italy.

An aeroacoustic characterisation of Low Mach number (~ 0.2) tip leakage flows is carried out at the anechoic wind tunnel facility of the Ecole Centrale de Lyon. Results suggest that the pressure fluctuations induced on the airfoil by the tip leakage vortex are scattered into sound at the trailing edge whereas another high frequency source seems to be related to the jet-like leakage flow impinging the main flow on the suction side. These features are evidenced by PIV, unsteady wall and far field pressure measurements as well two points PIV-PIV, PIV-pressure, HWA-Pressure and pressure-pressure cross-statistics in the gap region. The experiment is carried out on a single airfoil located in the potential core of a flanged jet in a medium at rest. The leakage flow is obtained by loading the high camber foil and a parametric study of the angle of attack, the gap size and the flow velocity shows that the two former have a significant impact onto the flow structure whereas the velocity mainly sets the magnitudes of the unsteady flow patterns.

Nomenclature

(O, x, y, z)	Airfoil-based coordinate system
h	Gap size [mm]
c	Chord [mm]
d	wire-to-probe distance [mm]
e	Airfoil maximum thickness [mm]
f	Frequency [Hz] or [kHz]
R_{uu}, R_{uv}, R_{vu}, R_{vv}	two-point correlations between velocity fluctuation components
U_0	Inflow velocity [m/s]
U	Mean velocity component in the x direction referred to as *chordwise* [m/s]
V	Mean velocity component in the y direction referred to as *cross-stream* [m/s]
W	Mean velocity component in the z direction referred to as *spanwise* [m/s]
Uc	Chordwise convection velocity [m/s]
U_0	Inflow velocity [m/s]
u', v'	Chordwise and cross-stream rms value of the velocity fluctuations [m/s]
α	Angle of attack [deg]
γ^2	Coherence between two signals
η	Physical spacing for spanwise correlations [mm]
ϕ	Phase angle [deg] or [rad]

*PhD Student, Centre Acoustique du LMFA - UMR CNRS 5509, Ecole Centrale de Lyon, Ecully Cedex, F- 69134, France.

†Assistant Professor, Centre Acoustique du LMFA - UMR CNRS 5509, also at University Claude-Bernard Lyon I, Villeurbanne Cedex, F- 69622, France.

‡Associate Professor,(DIMI), University 'Roma 3', Via de la Vasca Navale 79, Rome I- 00146, Italy.

§PhD Student,(DIMI),University 'Roma 3',Via de la Vasca Navale 79, Rome, I- 00146, Italy.

I. Introduction

In the current context of turbomachinery noise reduction efforts, the fan-OGV is one of the main regions of interest. The contribution of broadband noise to the overall noise level is certain, especially during the landing phase where it accounts for as much as 50 %. Among other broadband noise sources, rotor self noise is compose of two major components, the noise generated when the blade boundary layer disturbances interact with the trailing edge and the noise generated by the tip leakage flow interacting with the geometrical singularities of the blade tip. The former is quite well known, documented and modelled (*e.g.* Rozenberg *et al.*[1]) whereas the latter remains quite unexplored as far as the noise radiation is concerned and the tip clearance noise is not clearly ranked among other broadband sources in the secondary flow. Nevertheless, its influence on thrust losses is not questionable. Therefore, over the past years, many aerodynamic studies have been devoted to tip leakage flows. Bindon,[2] Storer and Cumpsty[3] showed that the tip leakage flow consists in a quasi cross-stream jet-like flow from the pressure side to the suction side, that rolls up into a Tip Leakage Vortex (TLV) when interacting with the inflow at the suction side. Recent experimental studies conducted on a compressor cascade by Muthanna,[4] Tang[5] and Intaratep[6] showed that the circulation of the TLV increases while traveling down the suction side edge, until the vortex detaches from the edge and starts moving away from the suction side toward the pressure side of the next blade. After detaching, the circulation stops increasing and the vortex slowly disappears when interacting with the blades wakes. As the gap size increases, the position of the vortex detachment moves downstream (Intaratep[6] showed that this evolution is linear) and the circulation of the vortex increases.

From the acoustic standpoint, there are several candidate sources in this flow:

- the jet-like clearance flow could generate sound when leaving the clearance region either directly or by interacting with the blade tip edge(s);
- the TLV feeds unsteady perturbations into the blade wall pressure field that could become sound sources as they are scattered by the tip edge and/or the trailing edge corner;
- to these pure self noise sources, one could add possible interaction noise sources due to ingestion of incoming disturbances by the tip clearance flow.

Until recent years, tip clearance noise was not very well documented in literature and besides the work of Dunne & Howe,[7] modeling efforts remained quite sparse for this difficult problem. As a result, a hierarchy of these possible source mechanisms was not found in literature and even the overall contribution of tip clearance noise remains unclear. In many attempts to address this question, the tip clearance self noise could not clearly be distinguished from interaction noise between the tip flow and the OGV.

Among the experiments concerned with tip clearance noise, the careful study of Ganz & al[8] indicated fan tip noise is not a significant sound source although their study also illustrated that it is quite difficult to identify the role of tip clearance noise among others noise sources on a representative fan rig. Other studies on rotating rigs led to different conclusions as to the magnitude of tip clearance noise (Fukano & Takamatsu,[9] Fukano & Jang[10]) and some even tackled to problem of tip flow control (Khourrami & Choudari,[11] Corsini *et al.*[12]).

In the present study, both aerodynamic and acoustic results of a single airfoil experiment are discussed. Unlike in the aforementioned cascade experiments, no relative motion between the airfoil and the tip-facing wall was achieved since the airfoil was mounted between two plates. However a significant clearance flow was obtained by selecting a highly cambered airfoil and loading it. Far field measurements could also be carried out since the flow was surrounded by a medium at rest. The outline of the present paper is described hereafter. The experimental set-up and measurement techniques are described in Section II. The main results about are shown in Section III whereas correlations are discussed in Section IV. Conclusions are drawn in Section V.

II. Experimental set-up

The experiment is carried out in the anechoic open jet-facility of the Ecole Centrale de Lyon. The test rig is mounted into the potential core of a low Mach number high speed jet in a large anechoic room($10\times8\times8\text{m}^3$). The jet flow is fed by an anechoic subsonic wind tunnel with a $450\times200\text{mm}^2$ rectangular nozzle. Two wooden plates are mounted at the top and the bottom of the nozzle exit with a turnable wooden disk on each plate in order to allow angle of attack modifications. The experimental set-up is sketched on fig. 1. The blade is a 200 mm chord and 200 mm span NACA 5510 airfoil (5% camber, 10% thickness) which is attached to the top disk. The tip clearance gap can tuned by varying the distance between the airfoil's tip and the bottom plate while the distance between the two plates is kept equal to 200 mm.

In the present study the Mach number is kept below 0.3 and is about 0.2 in the reference configuration, that is, a flow velocity $U_0 = 70\text{m/s}$ and the corresponding chord based Reynolds number is $\text{Re}_c \approx 960000$. The turbulence level at the nozzle exit is $u'/U_0 \approx 0.7$. Furthermore, the reference configuration is characterised by a 15 deg angle of attack and an $h = 10$ mm gap.

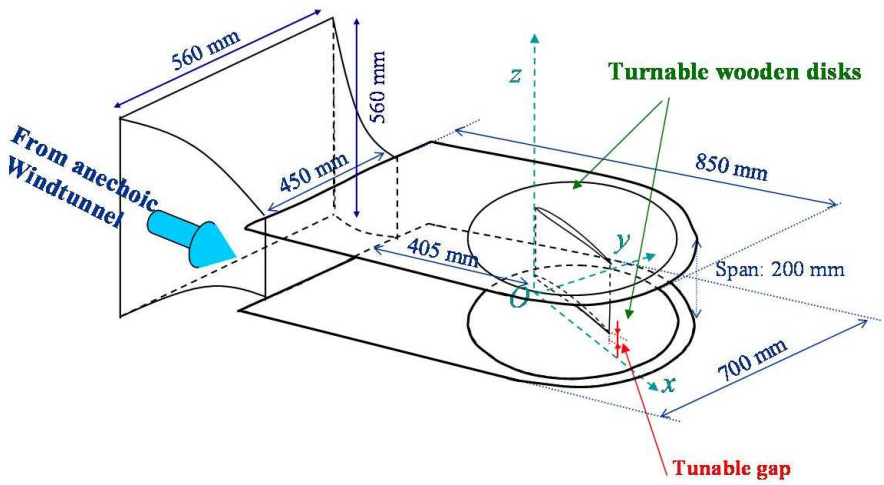

Figure 1. Experimental set-up.

Starting from this reference configuration, the inflow velocity, the angle of attack and the tip clearance gap are varied between $U_0 = 20$ and 90 m/s, $\alpha = 0$ and 18 deg, $h = 0$ and 25 mm respectively. The $h = 0$ mm, which corresponds to a configurations without gap, gives a comparison point for the non-zero gap configurations.

The coordinate system is based upon the airfoil chord: the x-axis is aligned with the chord and directed from the leading to the trailing edge, the y-axis corresponds to the cross-stream normal-to chord direction and is oriented from the pressure to the suction side whereas the z-axis is parallel to the span and directed from the bottom to the top plate as shown on fig. 1. The origin O is the projection of the airfoil leading edge onto the bottom plate.

A. Aerodynamic measurements

The aerodynamic data are acquired using Particle Intensity Velocimetry (PIV), LASER Doppler Anemometry (LDA) and single and cross Hot Wire Anemometry (HWA). Most of the results shown in this paper are obtained *via* PIV. Only velocity-pressure cross-correlations discussed in Section IV and upstream velocity profiles rely on single wire anemometry.

The PIV measurements are performed in planes parallel to the plates, at different z locations. Two CCD cameras with 35 mm lenses controlled by the *LaVision* software *Davis* are placed next to each other, beneath the bottom disk (equipped with a glass window). Each camera has a 1280×1024 pixels resolution and the velocity fields are computed using a 32×32 pixels interrogating window and 50% overlap that corresponds to a $1.6\times1.5\text{ mm}^2$ area. The overall measurement field is a $250\times105\text{ mm}^2$ rectangle that is not aligned with

the airfoil chord. The time delay between two images is kept between 5 and 40 μm because of the high 3D structure of the flow that results in a strong cross-plane flow motion, especially in the gap region. The Laser is mounted on the airfoil sides about 1 m away from the flow in order to shed light over the whole airfoil. Heated paraffin is used as seeding material and is injected upstream of the wind tunnel.

In order to cross-validate the PIV data, to compute velocity-pressure cross-coherence, to determine the incoming flow far upstream of the airfoil and to obtain spectral information about the flow field, LDA and HWA measurements are carried out at various positions in the gap region, the midspan plane and in the upstream boundary layer. LDA results are not further discussed in this paper.

The HWA measurements are carried out using a *Dantec* anemometer with a *Dantec* 55P11 single wire. The sampling frequency is about 10 kHz for mean velocity measurements and 45 kHz to 64 kHz for spectral analysis. HWA measurements are performed by moving the probe normal to the chord when measuring in the gap of wake region, and normal to the airfoil surface elsewhere.

B. Pressure measurements

The airfoil and the bottom plate are equipped with wall pressure probes at locations sketched on fig. 2. Probes 19 to 29 are located about 1.5 mm above the suction side tip edge at $x/c = 0.25; 0.5; 0.775; 0.9; 0.955$ and 0.975 respectively. Probes 26 to 28 are located at $x/c = 0.975$ and distributed spanwise at $\eta = 14.5; 4.5$ and 1.5 mm from probe 29 respectively. Probes 49 to 53 are located on the bottom plate at $x/c = 0.975$ and distributed in the cross-stream direction at $y/c = -0.1; 0; 0.05; 0.1$ and 0.25, respectively, that is, $y = -20; 0; 10; 20; 50$ mm. Probes 22 and 24 are at the same spanwise location as probe 26 and at the same cross-stream locations as probes 21 and 23 respectively. Probes A and B are on the tip in the middle of the gap at $x/c = 0.03$ and $x/c = 0.775$ respectively. Probe 56 is on the bottom plate facing probe B in the gap. Probe 46 which not shown here, is located near the pressure side tip at $x/c = 0.775$ whereas probe 41 which not shown here either, is located on the pressure side near the trailing edge at midspan. The probes are remote microphone probes described by Roger & Perennes.[13] *Bruel & Kjaer* 4935 ICP microphones were used for remote unsteady pressure measurements. These microphones are pre-amplified using a *PXI* system. The calibration method used here was described by Arguillat.[14] It allows to obtaining relevant spectra up to 6-8 kHz. The same pinholes as those used for the remote probes can also be connected to a *Furness* manometer for steady pressure measurements.

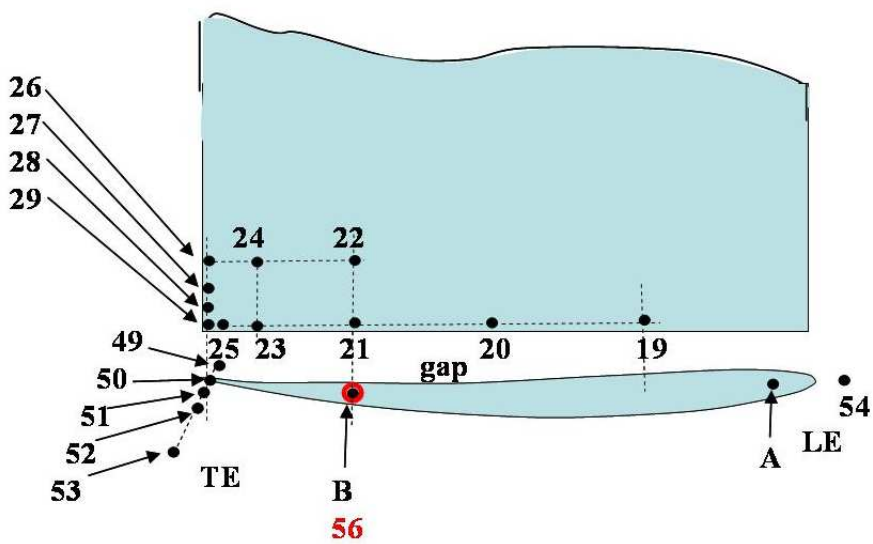

Figure 2. Position of the wall pressure probes

Directivity measurements are also performed using two half-inch 4191 B&K microphones mounted at 1.7 m from a rotating axis parallel to the z axis, located on the x axis 15 mm upstream form the leading edge. The

measurement angle with respect to the chord ranges from ±50 deg to ±130 deg (negative angles correspond to the pressure side). Measurements are also carried out without the airfoil at different inflow velocities in order to measure the background noise of the experimental set-up.

III. Main results

A. Reference configuration

The inflow velocity half a chord upstream of the airfoil is uniform within 5%. The inflow turbulence level is found to be $u'/U_0 \approx 0.7$ % in the potential core of the jet (see fig. 3), whereas it reaches 8% in the upstream bottom boundary layer (about half a chord upstream). The boundary layer thickness reaches δ= 18 mm and the displacement thickness δ^*= 1.4 mm.

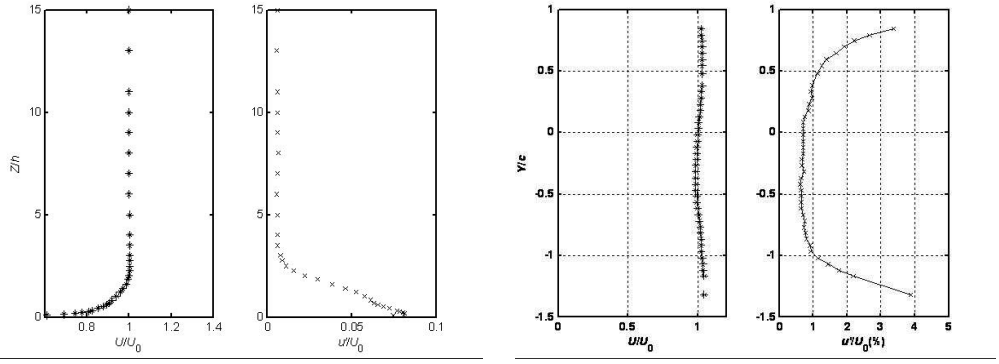

Figure 3. Inflow characterisation: boundary layer profile (left) at x/c= - 0.5 and inflow velocity measurement at midspan, x/c= - 1.5.

Fig. 4 shows the chordwise and cross-stream mean and rms fluctuating velocity fields in the midgap plane of the reference configuration. The white area as well as the isolated spots are due to light reflections by the airfoil pressure side and by dust particles on the glass window respectively. From this figure it is obvious that most of the flow physics occur on the suction side and in the gap region whereas the flow remains quiet on the pressure side of the airfoil. The suction side fields can be divided in two areas, the upstream and the downstream half of the airfoil respectively. In the upstream area, two driving forces of the gap flow can be observed on the cross-stream velocity component (top right plot):

- the tip leakage flow is due to fluid pushed from the pressure the suction side through the gap and forms a jet-like flow that leaves the tip clearance near mid-chord;
- the tip leakage jet is deflected by the outer flow.

It can be observed on the bottom plots that the rms-velocity remains very low under the airfoil and around its upstream part.

The downstream region starts approximately where the cross-stream jet reaches its maximum speed, V_{max} = 1.45.U_0, slightly downstream of the half chord $x/c \sim 55\%$, the TLV develops on the suction side of the airfoil and the rms velocity starts to grow as soon as the TLV develops on the suction side.

The present figure is typical because it also shows that two high rms velocity regions develop in what is likely to be the sides of the TLV: the velocity fluctuations result from the shear between the vortical flow of the almost chordwise oriented TLV (inducing a cross-stream motion) and the outer chordwise oriented flow. The external highly fluctuating flow strip is oriented away from the airfoil toward the outer flow. The turbulence levels in this region are very high: u'/U_0 and v'/U_0 reach about 22%. The second region with high turbulence levels is found between this strip and the airfoil, in the downstream part of the airfoil. Here the turbulence levels are very high as well: they range up to 20%.

Typical wall pressure spectra obtained in the reference configuration are plotted on fig. 5: the top plot shows the pressure spectra obtained along the suction side tip whereas the bottom plot shows the pressure spectra across the gap at x/c=77.5% as illustrated respectively on the right plots of this figure.

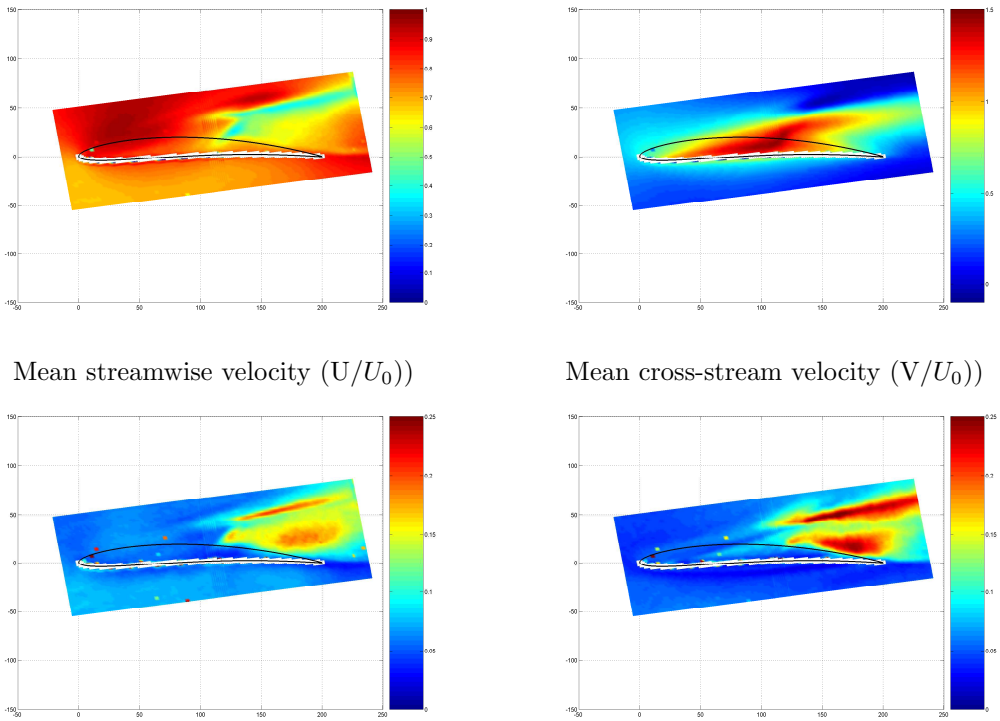

Mean streamwise velocity (U/U_0))

Mean cross-stream velocity (V/U_0))

Rms streamwise turbulence rate (u'/U_0))

Rms cross-stream turbulence rate (v'/U_0))

Figure 4. Mean (top) and rms (bottom) fluctuating velocity fields at $z = 5$ mm in the reference configuration. On the left: chordwise component. On the right: cross-stream component.

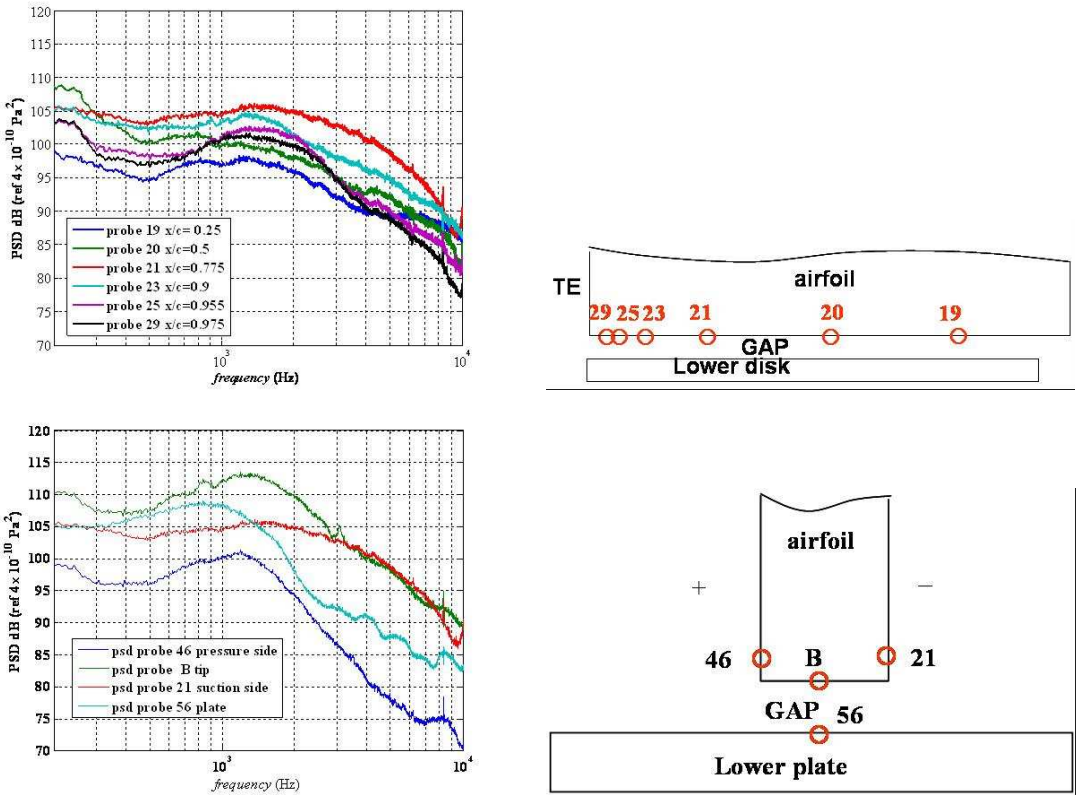

Figure 5. Wall pressure spectra : spectra (left) on the suction side tip edge (top) and in the gap at x/c=77.5% (bottom). Sketch of corresponding probe locations (right: top and bottom respectively).

Several conclusions can be drawn from these plots. Concerning the overall levels, a significant fluctuation increase can be noticed near the rear part of the suction side tip edge: a maximum seems to be reached in the region of probes 21 and 23, that is, 75 to 90 % chord approximatly. Downstream and upstream of this region the suction side pressure fluctuations decrease gradually. As shown on plot (b), levels are even lower on the pressure side except near tip. Among the pressure side tip probes, probe 46 whose spectrum is shown on plot (b) is located at the same chordwise location as probe 21. Concerning the spectral content of the wall pressure fluctuations, a large pressure level increase between 0.5 and 3 kHz is found in the gap. Although this rise affects most probes in the gap region it is particularly pronounced in part of the gap scrutinised on the center plot of fig. 5. This hump is not observed away from the tip clearance (e.g. pressure side mid-span wall-pressure spectrum of fig. 11 (a)). Therefore it can be concluded that this is an effect of the tip clearance flow. Moreover the fact that it is most pronounced in the gap seems to indicate that is due to a strong flow unsteadiness of the flow across the gap, probably a flow separation at the pressure side tip edge.

The far field spectra for the reference configuration are plotted with respect to the observation angle and the frequency, as shown on fig. 6(a). In order to highlight the frequency ranges where the tip noise has a major impact on the sound level, spectral differences are computed by substracting the spectra measured in the h= 0 mm case from those measured with a non zero gap. The result for the reference configuration is plotted on fig. 6(b).

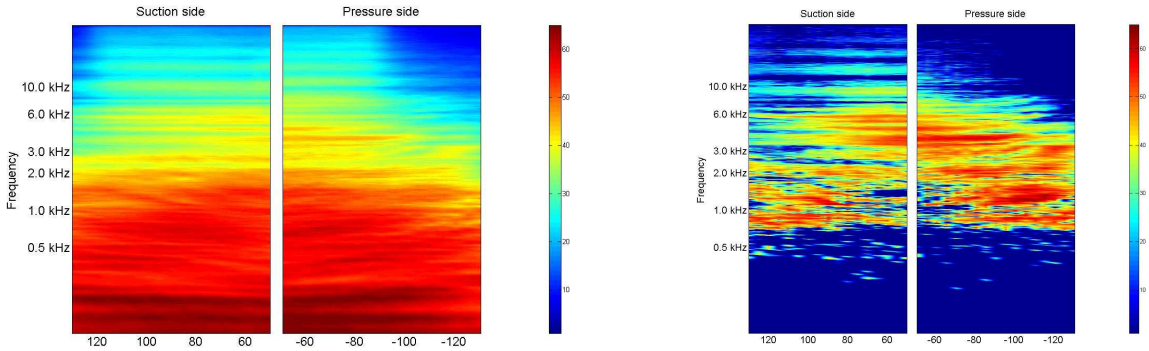

Figure 6. Far field directivity maps: total field(left) and estimated tip noise contribution(right); the observation angle is defined as the angle between the x axis and the probe position in the midgap plane; the negative values of the observation angle correspond to the pressure side and the positive values to the suction side.

Two main domains can be distinguished on these charts: the first one lies in a 'low' frequency range between 0.7 Hz and 3 kHz. It corresponds to an upstream radiation. The second one lies in the 'high' frequency range 4 to 7 kHz and corresponds rather to a downstream radiation. This latter is referred to as the high frequency area. The low frequency radiation is particularly interesting, since it reaches the highest sound levels. Moreover its frequency range corresponds to that of the gap pressure fluctuations discussed in the previous paragraph. Thus, the low frequency upstream radiation can be related to gap pressure fluctuations. Its upstream directivity is consistent with classical trailing edge noise theory, which would lead to the conclusion that the tip clearance fluctuations are convected past the trailing edge corner and start to radiate efficiently as they are scattered by it.

As far as the the high frequency radiation is concerned, a candidate source mechanism should be sought in the dynamics of the small scales. Additional information is required to draw a more precise conclusion.

B. Influence of the angle of attack

The angle of attack is found to have a strong influence onto the flow. Since the jet width is of the order of 2 chords, it is deviated by the loaded airfoil, which explains that no stall is found at the highest angles of attack. In fact a slight leading edge separation is found at the smallest angle of attack (5 deg) on the pressure side near the leading edge. As shown on fig. 7, the position where the TLV detaches from the suction side moves upstream as the angle of attack increases. The TLV grows and the turbulence levels increase along with the angle of attack.

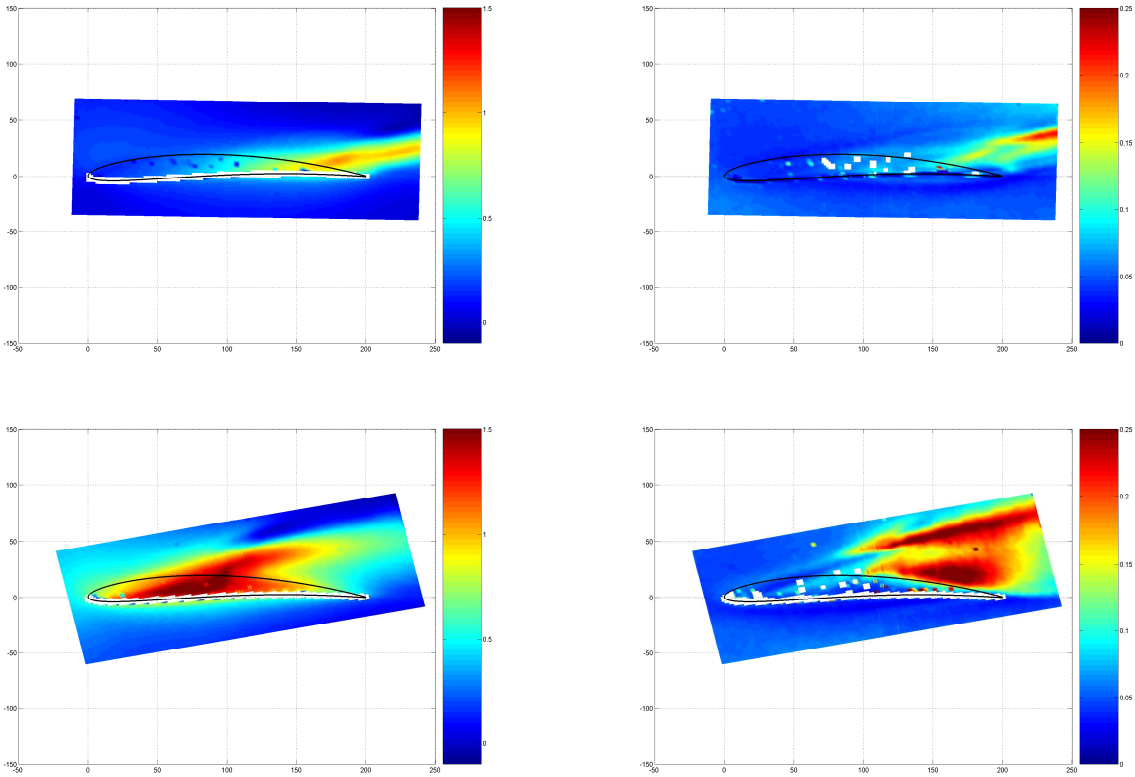

V/U_0 v'/U_0

Figure 7. Influence of the angle of attack. Mean cross-stream component (left) and cross-stream turbulence rate (right) at α=5 deg (top) and α=18 deg (bottom).

C. Influence of the inflow velocity

The inflow velocity has no impact onto the flow when it is varied between 40 and 90 m/s: fig. 8 shows the that the non-dimensional cross-stream velocity V/U_0 and its rms level v'/U_0 are very similar to those obtained for a 70 m/s flow (see fig. 4. Similar observations are made for a 90 m/s flow).

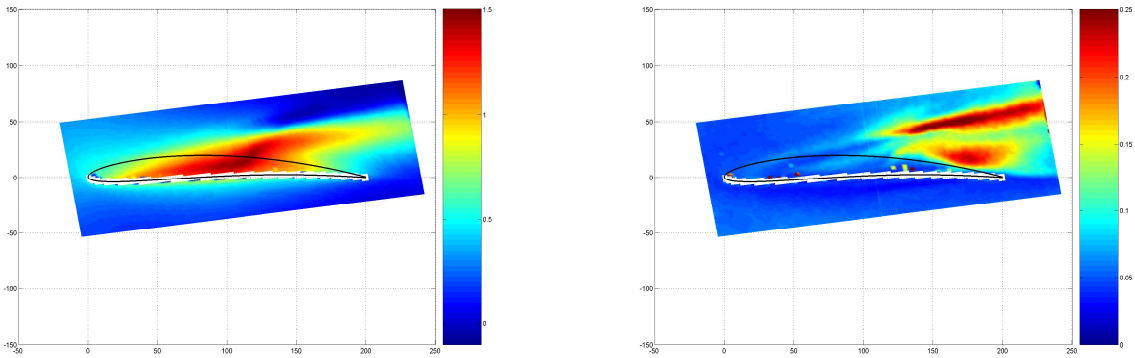

V/U_0 v'/U_0

Figure 8. Influence of the inflow velocity: PIV results. Mean chordwise component (left) and cross-stream turbulence rate (right) at U_0=40 m/s.To compare with the fig. 4 (right)

On fig. 9, the spectrum obtained from a probe located near the gap-trailing edge corner, probe 25, is plotted for velocities ranging from 20 to 90 m/s: the PSD is divided by U_0^3 and the frequency is made non-dimensional by the chord based Strouhal number $St = fc/U_0$: subsequently the spectra merge almost exactly. Thus the unsteady blade response in the gap region is proportional to the inflow power. Moreover this non-dimensional representation shows that the $0.5 - 3$ kHz hump observed on fig. 5 is found for all velocities to range from $St = 0.2 - 8$. The hump maximum observed at 1400 Hz in the 70 m/s case is reached at a $St \sim 4$. When based on the gap size h and the maximum velocity in the jet (about $\sim 1.5U_0$), the Strouhal number of the maximum is 0.13, which is nearly the value $St = 0.1$ observed by Vallette[15] for a jet deviated by a crossflow.

The velocity dependence of the directivity maps provides interesting information. The frequency domain where the tip noise is dominant increases with the inflow velocity. The excess noise spectra of the tip flow are integrated to provide an estimate of the overall sound power generated by the tip clearance flow at various velocities. It is found that the sound power increases with U_0^5. Although the velocity dependence was tested at many flow velocities in the reference configuration that are not sketched here, this dependence is partly shown on fig. 12, where the level of the sound power divided by U_0^5 and integration constants is plotted against the thickness-to-gap ratio e/h. It can be seen that although the sound power has a complex gap dependence, its velocity dependence is consistent with U_0^3 power law for intermediate gap values $h = 5; 7; 10$ mm. Another result not shown here is the separate velocity dependence of the two possible source mechanisms: while a U_0^5 velocity dependence is found for the 'low' frequency source confirming the possible role of trailing edge scattering in the underlying source mechanism, the 'high' frequency source has a U_0^7 to U_0^8 velocity dependence indicating a possible volume source radiation that might be related to the leakage jet flow.

D. Influence of the gap size

The gap size is a major parameter of this flow, that is why its influence has been investigated in a large gap range. However, the Laser sheet thickness and the reflections problems mentioned in section III, prevented from carrying out measurements at gaps lower than 5 mm. The cross-stream mean velocity and turbulence level in the reference configuration for gaps $h = 5$ and 15 mm and $z = 3$ and 7.5 mm are presented on respectively on the top and bottom plots of fig. 10. Two trends can be observed as the gap is increased:

- the gap jet moves toward the trailing edge.
- the turbulence rates in the TLV region increase.

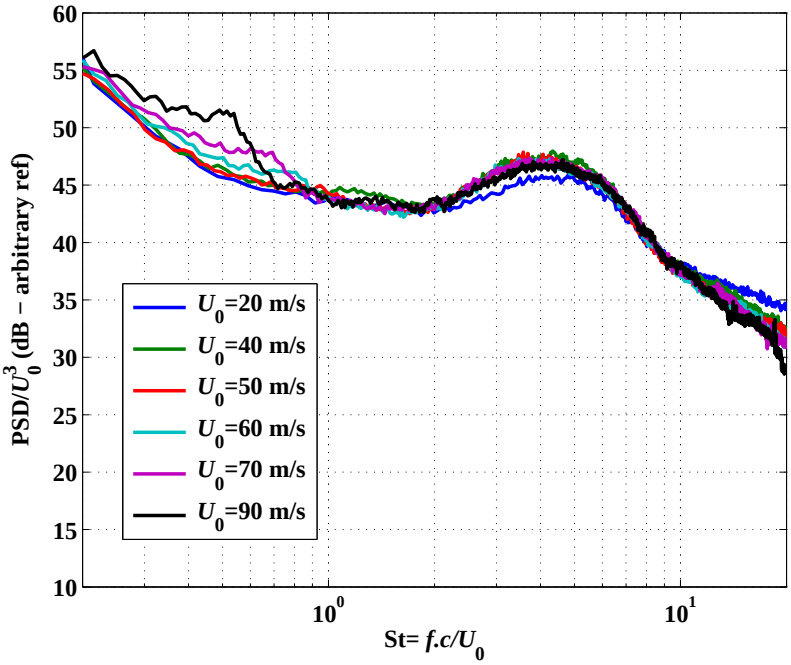

Figure 9. Influence of the inflow velocity: wall pressure spectra for inflow velocities ranging from 20 to 90 m/s. The spectra are plotted against chord based Strouhal number$St = fc/U_0$ and scaled with U_0^3

Indeed, the TLV detachment position which is the chordwise location where the maximum cross-stream velocity is reached, moves from $x/c = 0.3$ to 0.7 for $h = 5$ to 15 mm. The maximum cross-stream velocity remains constant, at $V/U_0 \approx 1.45$. The maximum cross-stream turbulence rates in the TLV-Inflow interaction region also increase from $v'/U_0 = 23\%$ to $v'/U_0 = 29\%$. Moreover, when the gap increases the TLV grows - *i.e.* the TLV section increases - over a shorter distance. These results are in agreement with those found by Tang[5] and Intaratep,[6] even if no particular linear trend was found as in Intaratep's results.

The smaller gaps could only be investigated with help of wall pressure and far field directivity measurements. Fig. 11 shows spectra for gap $h = 0$ to 10 mm at $x/c = 77.5\%$, on the suction side edge (probe 21), under the blade tip (probe B) and at the pressure side edge (probe 46). Probe 41 is on the pressure side at midspan near the Trailing Edge. The following conclusions can be drawn:

- the gap size has no influence on the wall pressure at midspan, as shown on fig. 11(a).

- there seem to be two flow regimes, depending on the gap size.

This second result is particularly interesting: there is no $St = 4$ hump on the suction side spectra for gaps up to 5 mm, whereas in the vicinity of the gap on the pressure side (probe 46), the hump can be distinguished for the $h = 5$ mm gap. On probe B, the hump is even found in the $h = 3$ mm case. A possible explanation is that the hump corresponds to a flow separation occurring as the flow penetrates the clearance: according this scenario, for narrow gaps, the flow would not detach at the gap entrance: this could explain that no hump is found for $h = 1$ and 2 mm. For large gaps, the flow would detach at the gap entrance and not reattach; thus the resulting pressure fluctuations would even be felt by probes located on the suction side and in the TLV forming at the suction side. Finally, for intermediate values, the separation bubble would be long enough and turbulent fluctuations would be strong enough to be felt on probe B ($h = 3$ mm) or even on probe B and 46 ($h = 5$ mm) but would still reattach before leaving the clearance. This scenario has actually been reported in literature. Indeed, Denton[16] showed that the flow reattaches for blade thickness-to-gap ratios greater than 2.5, whereas Storer and Barton[17] showed that there is no reattachment when this ratio is lower than 1.5. As discussed in the Part 2 of this study, the aerodynamic perturbations felt by probe B originate from the half chord region, where the thickness is of the order of 14 mm. The corresponding

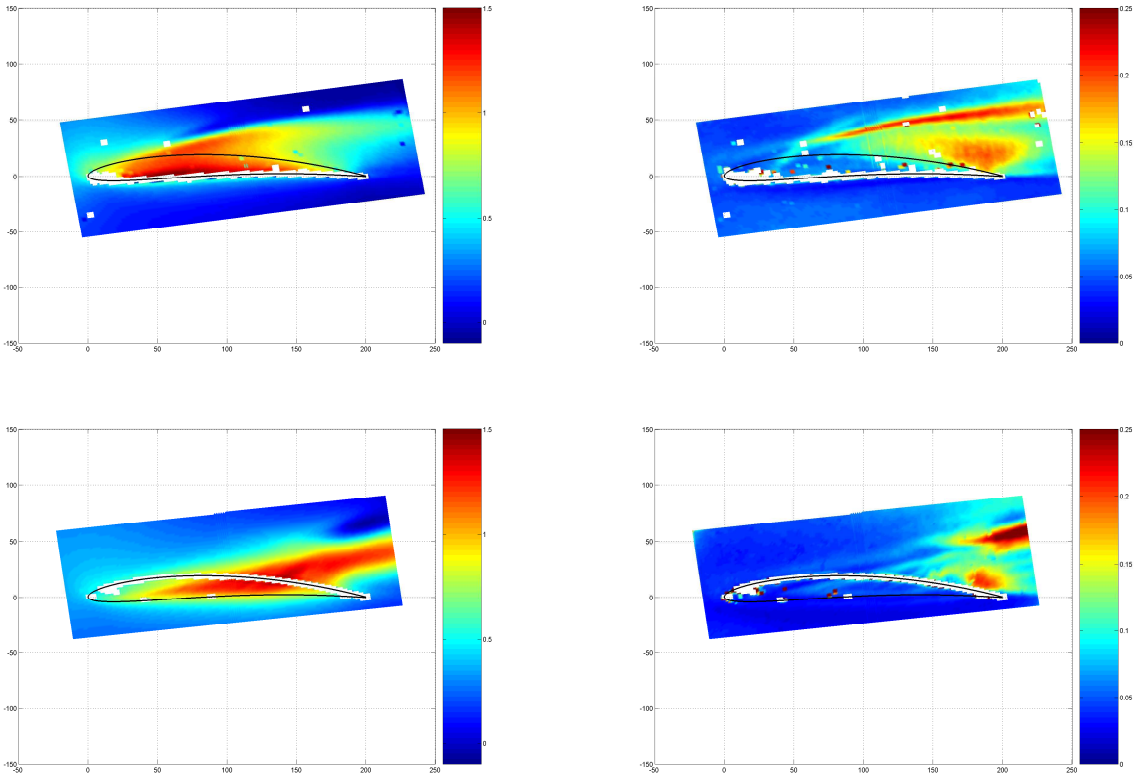

V/U_0 v'/U_0

Figure 10. Influence of the gap size. Mean chordwise component (left) and cross-stream turbulence rate (right) in the mid-gap plane for: $h/c = 2.5\%$ (top) and $h/c = 7.5\%$ (bottom).

ratios are 14, 7, 4.6, 2.8 and 1.4 for gap size $h = 1$, 2, 3, 5 and 10 mm respectively. As expected, the flow reattaches for gap sizes up to $h = 3$ mm, does not reattach for $h = 10$ mm and is in the transition domain for $h = 5$ mm. In other words the clearance flow behaviour is ruled by the influence of the wall: when the wall is far enough, its influence is not significant and the flow around the tip behaves almost as a free flow. In other cases, the wall has an influence onto the tip flow and governs the reattachment of the separation occurring at the pressure side edge: for a range of distances, the flow separates but reattaches before leaving the gap. Finally it does not separate at all if the wall is sufficiently close to the the airfoil tip. This is a very interesting result, because the noise source mechanisms discussed in section A could thus be strongly affected by the thickness-to-gap ratio.

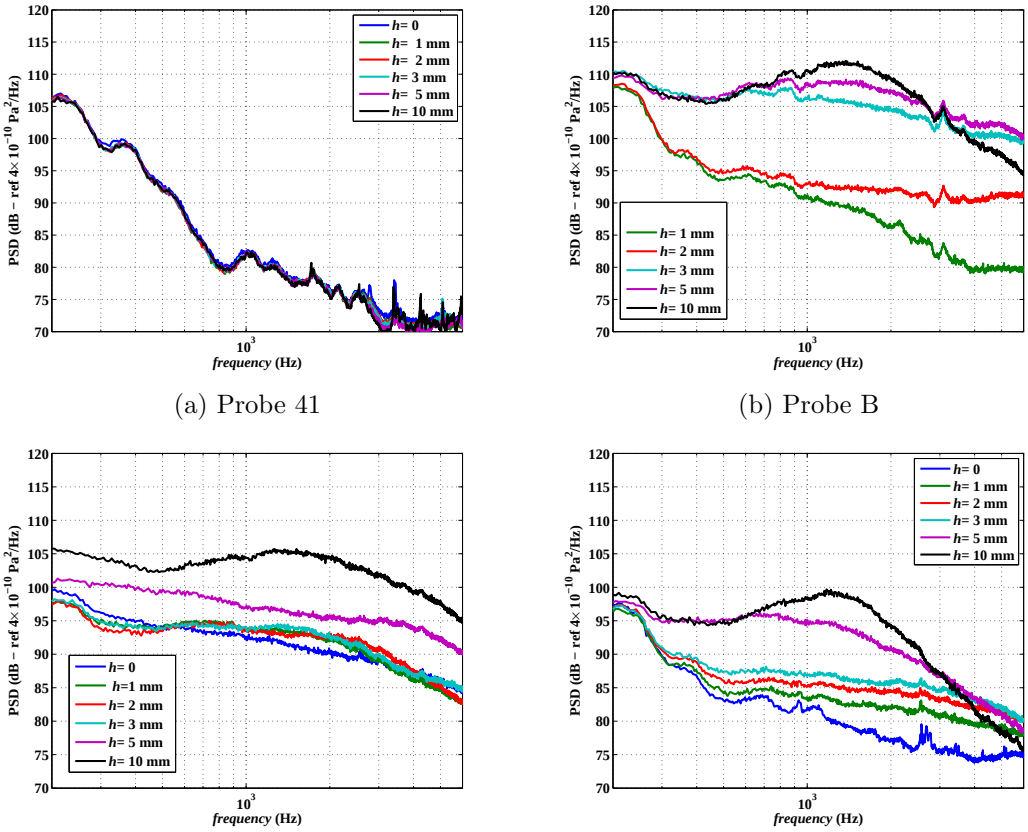

(a) Probe 41

(b) Probe B

(c) Probe 21

(d) Probe 46

Figure 11. Influence of the gap size onto the wall pressure spectra felt at $\sim 3/4$ chord by probes 21 (suction side tip edge), 46 (pressure side tip edge), B (tip) and near trailing edge by probe 41 (midspan pressure side). $\alpha = 15$ deg, $U_0 = 70$ m/s $h = 0$, 1, 2, 3, 5 and 10 mm.

The latter result is consistent with the far field directivity measurements, as shown on fig. 12. Two gap size explorations are carried out, one at U_0=40 m/s and the other at U_0=70 m/s. The overall sound power level is estimated by integrating the spectra with respect to the frequency and the observation angle. The results are plotted on fig. 12 with respect to the thickness-to-gap ratio, e/h, (e being the maximum thickness of the airfoil) and divided by U_0^5. The evolution is steep between $h = 3$ and 10 mm and much slower outside of this range.

Another interesting result is that there is no major sound level increase between $h = 10$ and $h = 25$ mm. This supports the idea that the wall does not influence anymore the tip flow and the resulting TLV formation for large gaps. At the other end, the fact that the ground value of the sound power for very small gaps is independent of the gap size (provided this size is small enough), supports the assumption that the TLV formation is not governed anymore by the tip clearance turbulence: thus for small gaps, the tip clearance

flow only feeds the TLV with a cross-stream momentum whereas the turbulence is now generated only by the TLV and its boundaries.

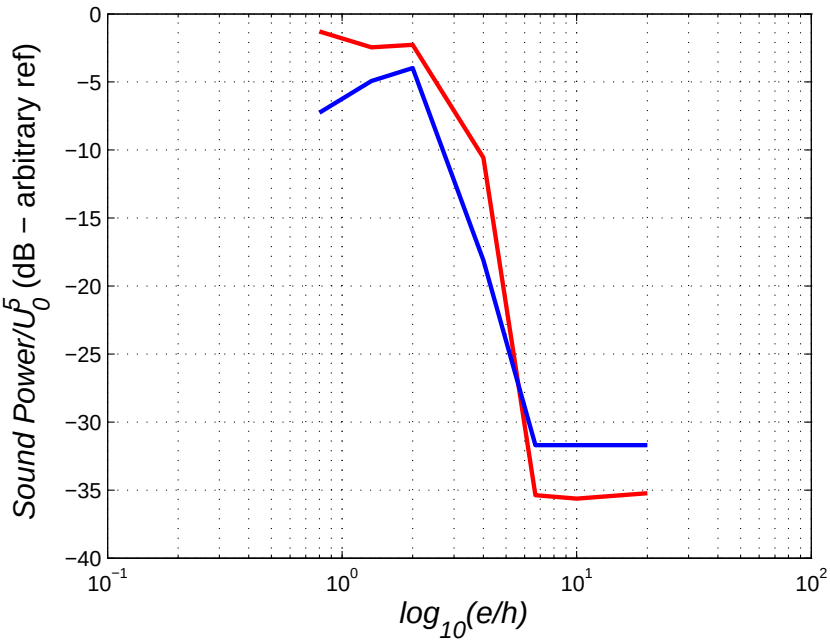

Figure 12. Influence of the gap size onto sound power. Sound power is divided by U_0^5, by integration constants and plotted against e/h: U_0=40 m/s (blue); U_0=70 m/s (red)

IV. Correlations

All results shown in this section are obtained in the reference configuration, that is, $U_0 = 70$ m/s, $\alpha = 15$ deg and $h = 10$ mm.

A. Pressure-pressure correlations

The top plot of fig. 13 shows the spanwise coherence obtained from a set of span-wise distributed probes near the trailing edge in the lower corner of the airfoil suction side (probes 26 to 29 shown on fig. 2). The time signals of the associated set of pressure probes provide coherence functions for a set of spacings η comprised between 1.5 and 14.5 mm. The coherence functions are characterised by two dominant frequency bands. One is a rather narrow peak with high coherence levels in the very low frequencies ($\leq$ 300 Hz) whose frequency range does not depend on the main flow velocity. The other frequency domain with a high coherence is distributed over a wide range of frequencies comprised between 0.7 and 3 - 4 kHz in the reference configuration: its frequency range corresponds to that of the pressure hump observed on the wall pressure spectra and depends on the flow velocity in a similar way as the wall pressure spectra do. From these functions, the spanwise coherence length is obtained at a given frequency by integrating the square root of the coherence with respect to the spacing. The results are given for various velocities, gap sizes and frequencies on the two bottom plots of fig. 13. In the reference configuration, the coherence length is about 8 mm at 1.5 kHz and falls down to $\sim$ 2 mm at 4 kHz. As shown on the left bottom plot where the coherence length is plotted against the inverse of the Strouhal number $St = fc/U_0$, the coherence length grows linearly with the inflow velocity for a given frequency between 1 and 4 kHz and is proportional to the inverse of the frequency for a given velocity within the range of values of U_0 examined. This result is interesting for modeling purposes since the coherence length appears to be predictable. On the right bottom plot of this figure, the coherence length is plotted against frequency for various gap sizes h at $U_0 = 70$ m/s. No clear tendency arises from this plot: this is because the gap flow undergoes several regimes between 0 and 10 mm as discussed in earlier sections.

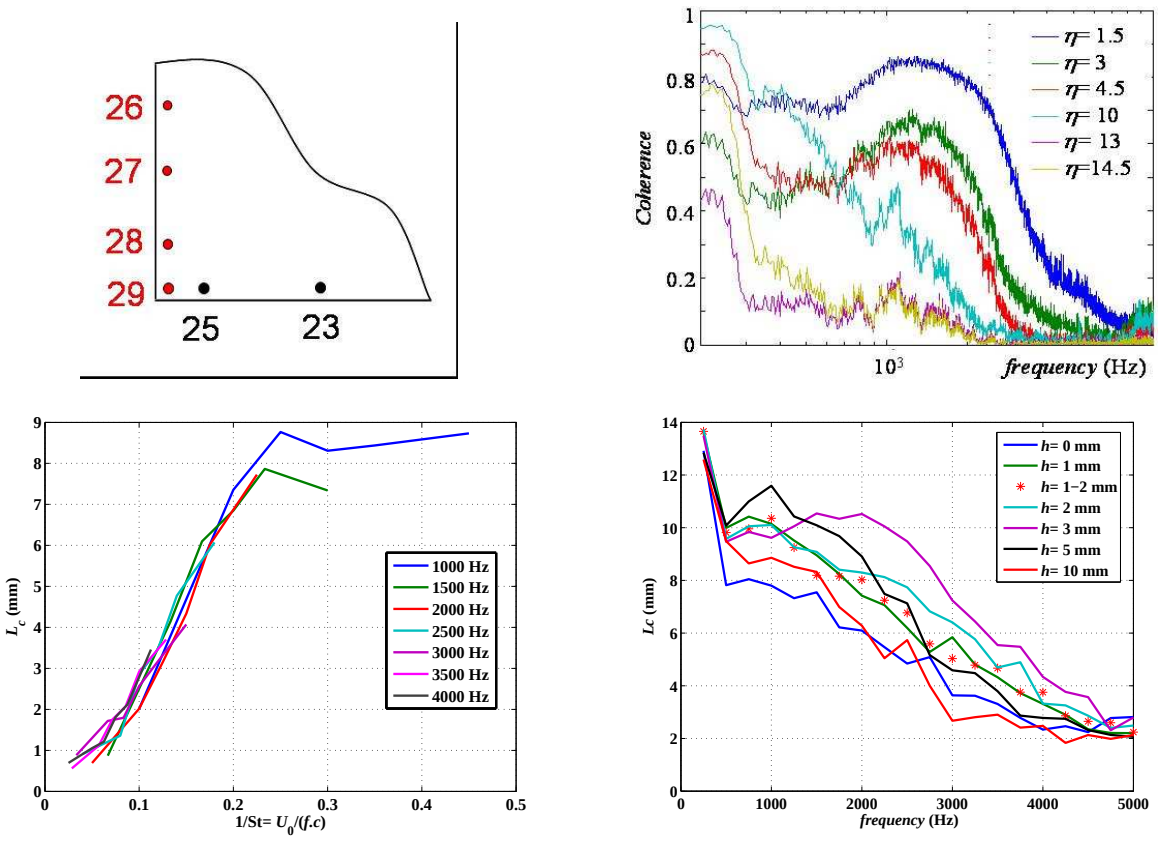

Figure 13. Spanwise coherence: Coherence γ^2 against frequency for various spacings in the reference configuration, η = 1.5 to 14.5 mm (top right), corresponding probe locations in red (top left), coherence lengths L_c versus the inverse of the Strouhal number (bottom left) and coherence lengths versus frequency for various gaps in the reference configuration (bottom right).

The convection velocity of the turbulent structures is another important quantity for aerodynamic models based on gust theories. It is computed by measuring the phase difference between two pressure probes (see the top plot of fig. 14) that are aligned in the stream-wise direction. In the case illustrated on fig. 14 the probes are number 23 and 25 (see fig. 2). They are located 11 mm from each other each other, 1.5 mm above the suction side tip edge at $x/c = 0.9$ and $x/c = 0.955$ respectively. The convection velocity is averaged on 500 Hz bands and the velocity is plotted for the center frequency of each band. Additional smoothing is obtained by averaging this value over 10 neighboring frequencies. Thus the frequency dependent convection velocity $Uc(f)$ is obtained in the 0.35 - 5 kHz range and plotted on the bottom of fig. 14. 3 parts can be identified on this curve. The first part is the lower end, say below 0.6 or 0.7 kHz, where quite high (up to 130 m/s) convection velocities are measured. The part of the flow facing probes 23 and 25 is still located in the high speed tip clearance flow. This could explain the fact that large structure are embarqued at such high speeds. However, this value seems extremely high and therefore a potential interaction of the fluid between the two probes seems likely to occur. This would be in agreement with the velocity independent low frequency part of the coherence functions shown on fig. 13. The second and most relevant part of the convection velocity curve, is the part comprised between 0.7 and ~ 1.9 kHz, where the convection velocity oscillates between 30 and 45 m/s and reaches a local maximum near 1.4 kHz. This part of the curve corresponds to the the broad band hump found on the wall pressure spectra and the coherence functions: it is the part that seems relevant for broadband noise models. In the third part of the curve, the convection velocity can not be estimated since the phase becomes random above 2.2 kHz. Similar observations are made for the set of probes 25 and 29 that are even nearer of the trailing edge and only 4 mm apart. In this case, the values of the second part of the curve are higher but the trend is the same.

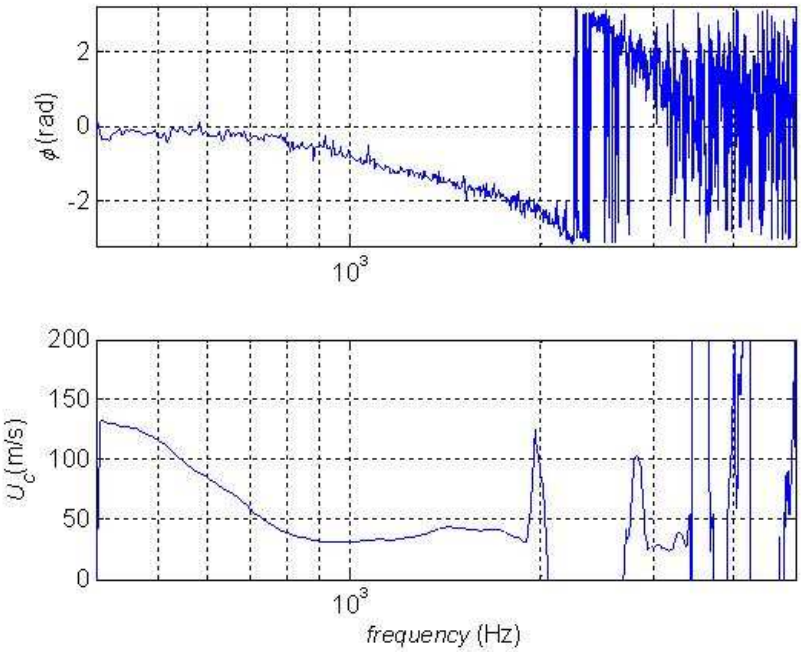

Figure 14. Convection velocity. Phase lag between Probes 23 and 25 (top) and convection velocity Uc between probes 23 and 25 (bottom).

B. Velocity-velocity correlations

Spatial correlations are computed from the PIV fields. An example is given on fig. 15: the reference point is located at $x/c = 59.5\%$ and $y/c = 11.5\%$, which is closely upstream of the TLV detachment position and faces the suction side gap. The measurements are carried out in the reference configuration, at $z = 5$ mm. The correlation fields are referred to as R_{uu}, R_{uv} , R_{vu} and R_{vv} and correspond respectively to chordwise/chordwise, chordwise/cross-stream, cross-stream/chordwise and cross-stream/cross-stream correlations.

Several features can be observed:

- the turbulence is highly anisotropic: R_{uu}, R_{uv} and R_{vu} clearly show a main direction, which is to compare with the TLV axis. Moreover R_{uu} spreads over a much larger region than R_{vv}. It is also interesting to note that R_{uu} is positive over a large region upstream of the correlation point whereas it becomes neutral to negative downstream of it. The oblique border line between the negatively and the positively correlated regions may be regarded as an unsteady sink/source, that is, a region where strong spanwise fluctuations occur. Such fluctuations are expected on the sides of the TLV;

- the cross-correlation fields R_{uv} and R_{vu} are not clearly symmetric, but are both separated into a positively and a negatively correlated region by the same line as R_{uu};

- all correlations involving the cross-stream component, and in particular R_{vu} and R_{vv} are weaker and limited to a smaller region (a few mm large spot in the case of R_{vv}).

So far, only a few correlation points have been explored and further computations are to be run in order to study the influence of the correlation point and to find out velocity projections that are tailored to the local flow physics.

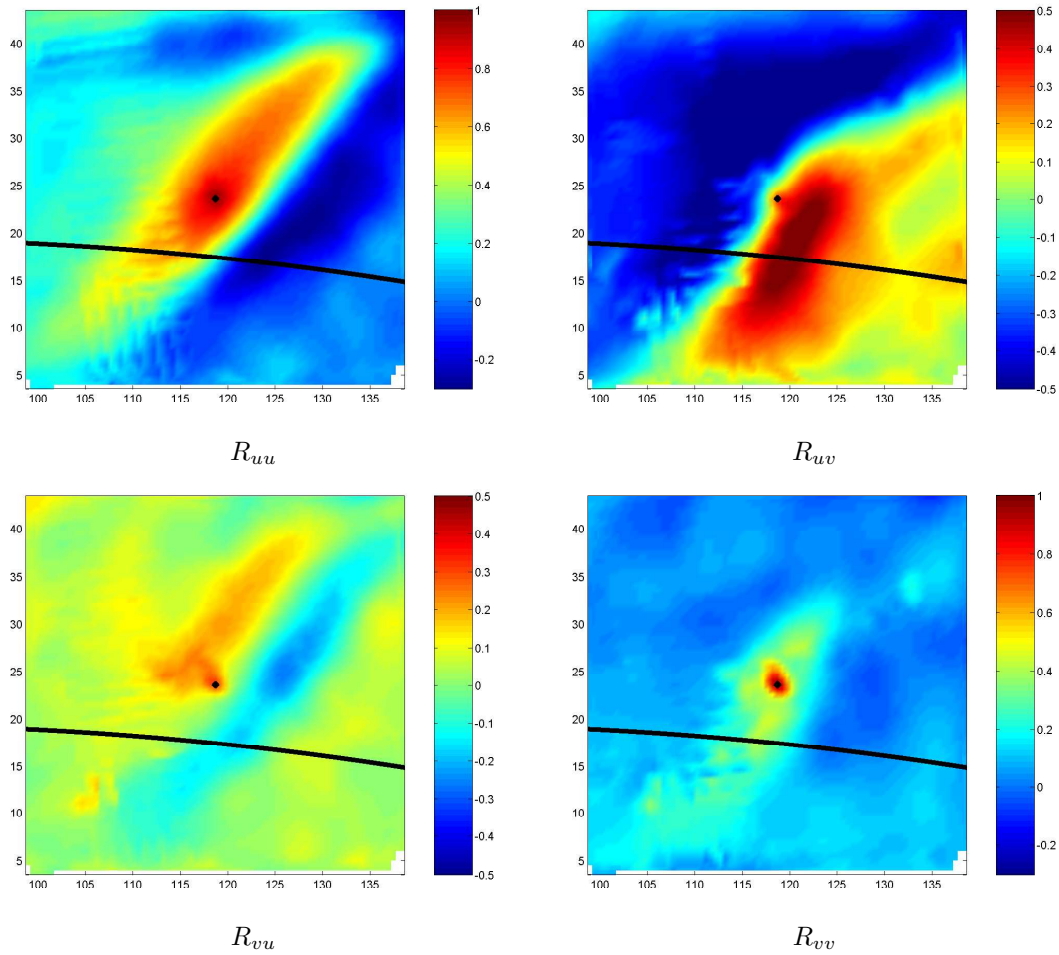

Figure 15. Correlations close upstream from TLV detachment in the reference configuration: (R_{uu}, top left), (R_{uv}, top right), (R_{vu}, bottom left) and (R_{vv}, bottom right). The circle symbolizes the reference point.

C. Joint pressure-velocity measurements

Some joint pressure-velocity measurements have been carried out as well:

- joint pressure-single HWA (sampling: 64 kHz): results are shown in this section using classical statistic approaches and in part 2 of this study using cross-wavelet techniques;

- one case with joint pressure-PIV for a cross-wavelet analysis (pressure sampled at 16 kHz; PIV at 10 Hz). 10 time series are measured and synchronised with altogether 600 PIV snapshots. Each time series lasts for 60 s. Results are analysed and discussed in part 2 of this study.

The coherence functions between a hot wire located near the T.E. facing probe 29 ($x/c = 0.95$,$z = 10$ mm) at 1 mm from the wall and pressure probes distributed along the suction side tip edge (probes 19 to 29) are plotted on on the top left plot of fig. 16 whereas the corresponding probe locations are sketched on the top right plot of this figure. Significant coherence levels are found from probe 29 up to probe 21 that is already 1/4 chord upstream of the hot wire. Another interesting result is that the low frequency part of the spanwise coherence found for the spanwise pressure coherence, is not present in these results. Finally, it can be seen that the medium frequency hump that was also found in the spanwise coherence now splits into two peaks at 2 kHz, one at frequencies ranging from 0.5 to 2 kHz, the other from 2 to 4 kHz. The coherence functions between the hot wire almost located at the same position but slightly further off the wall (facing the microphone probe 51) and pressure probes implemented into the bottom plate in the same region (probes 49 to 53) as well an upstream (probe 56) are plotted on the left middle plot of fig. 16. The corresponding probe locations are sketched on the middle right plot of this figure. The upstream probe (no. 56) is located on the plate at x/c=0.775 in the middle of the gap. The span-wise coherence is high at low and medium frequencies (even for probes that are far from the wall) corresponding to the hump of the spectra shown earlier (e.g. in fig. 5). It is interesting to observe that this plot also contains two types of functions, some with a single medium frequency hump centered at 1 to 1.5 kHz ranging from 0.3 - 0.4 to 2 kHz, other with an additional hump at ~ 3 kHz ranging from 2 to 4 kHz similarly to those found in the top plot. This second maximum is particularly strong when both probes are close together near the T.E.-tip corner. There are two possible explanations for this: either the 3 kHz peak only exists in the vicinity if the T.E.-tip corner, or it has a much shorter correlation length than the other hump and therefore vanishes as soon as the probes separate. The interesting point about this second hump is that it is not observed on the pressure-pressure coherence in the same region and could therefore be related to a specific aerodynamic event that does not generate strong pressure fluctuations on the airfoil. The most surprising results come from the coherence measurements between the hotwire and the probe 19: probe 19 is located 1/4 chord downstream of the leading edge, at the beginning of the tip clearance jet, according to fig. 4. The hot wire is moved along an oblique downstream line oriented away from the airfoil. Its spanwise coordinate is $z \sim 12$ mm, slightly above the gap, but facing probe 19 when it is in its vicinity. Results are shown on the bottom left plot of fig. 16 and the probe locations are sketched on the bottom right plot: the distance d is the wire-to-probe distance. In a similar way as for the previous HW-pressure coherence results, 2 peaks are observed when the hotwire is in the vicinity of the pressure probe, one low frequency peak, centered at 1.2 kHz and ranging from 0.7 to 3 kHz and a high frequency peak centered at 6 kHz and ranging from 3 to 9-10 kHz. The high frequency peak is strongest when the distance is about 3.5 mm, suggesting that the high frequency flow perturbations originate from the gap (thus the hotwire feels them slightly less when it faces probe 19, because it is shielded by the airfoil). For higher values of d, only a low frequency peak remains that is centered at 0.8 kHz. The low frequency part has already been identified and discussed on other measurements. The new feature is the high frequency component, that corresponds to the high frequency noise component found in the far field. Thus the high frequency noise radiation is generated by small eddies advected by the tip clearance flow that probably radiate when they mix at the outlet of the gap. The behavior at $d = 10.5$ and $d = 20.5$ mm is less clear. All these observations about the high frequency component comfort the conclusions made about the directivity plot in section III.A. More generally, the coherence measurements confirm and to some extent complete the observations made throughout section III.

V. Conclusions

The tip leakage experiment described in this study provided a huge amount of data. A few major results from this data set have been reported and commented here. Three main goals were thus reached:

- the sound radiation of the tip leakage flow is now documented and related to the tip leakage flow features; hence candidate source mechanisms were proposed;

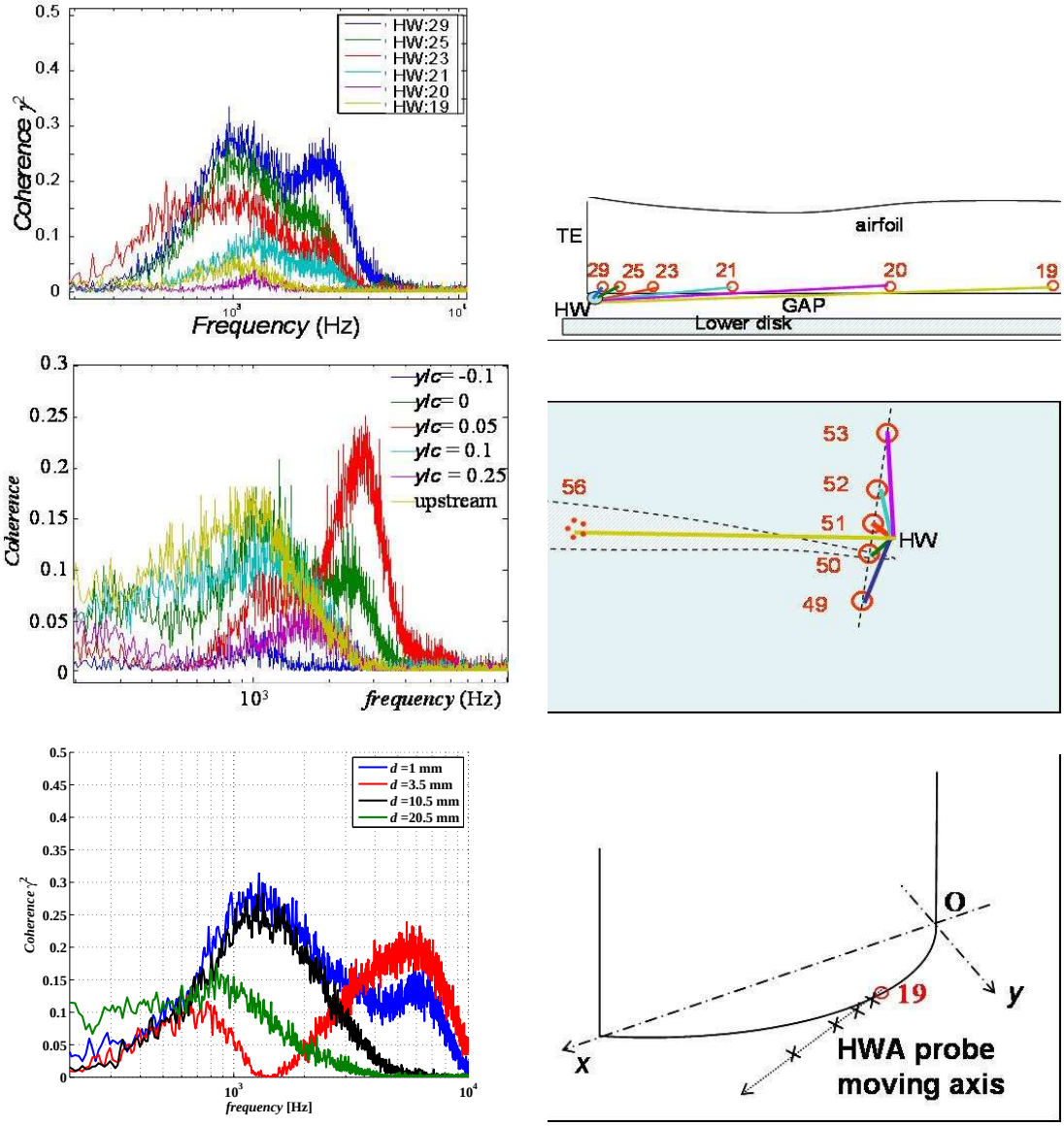

Figure 16. Pressure-velocity coherences: chordwise coherences for probes on the suction side edge at x/c = 25, 50, 77.5, 90, 95.5 and 97.5% (probe 19 to 29 respectively - top), cross-stream coherences for probes on the disk at x/c = 97.5% and y/c = -10, 0, 5, 10, 25% (probes 49 to 53 respectively, the coherence with the probe 56 located at x/c = 77.5% and y/c = 0% being referred to as upstream - center) and coherences along the TLV direction (bottom). The schemes on the right show the associated probe locations.

- a new light was shed on known results: wall pressure spectra could be related to the velocity field and to the far field;
- a database for tip clearance and trailing edge self-noise modelling as well as for CFD validation is now available.

More specifically, it was confirmed that the tip clearance flow generates a strong ($1.45U_0$) cross-flow that is deviated by the main flow when it leaves the gap in a similar way as a side-jet in a main flow, leading to the Tip Leakage Vortex (TLV) formation. In the conical mixing region between these two flows, high turbulence levels are reached. The flow fluctuations in the gap region are dominated by a large hump around $St = 4$ in the frequency domain. This hump is particularly pronounced in the gap but is correlated to the TLV. It is probably generated by a flow separation on the pressure side tip-edge and results into an upstream sound radiation. The U^5 dependence of this far field contribution as well as its directivity indicate that the flow perturbations might be scattered into sound as they are convected past the lower trailing edge corner. Additionally, high frequency oscillations occurring near the suction side tip-edge contribute to a rather jet-noise-like sound in the far field. Beside these aeroacoustic aspects, the parametric study led to following conclusions:

- with increasing angles of attack, the TLV starts to develop further upstream and its turbulent intensity grows as well;
- the non-dimensional aerodynamic fluctuations are velocity independent in the velocity range examined here;
- as established in the literature, the TLV is highly sensitive to the gap size since the flow structure itself depends on whether or not the flow separates inside the gap; the TLV formation region moves downstream as the gap increases and as a flow separation bubble grows from the gap entrance to the gap outlet;
- the spanwise coherence length in the lower trailing edge corner is proportional to the velocity and to the inverse of the frequency, but its dependence *vis-à-vis* the gap size is related to the flow separation in the gap.

In Part 2 of this study, a cross-wavelet analysis will be applied to joint pressure-velocity measurements and in particular to synchronised pressure-PIV measurements in order to track coherent structures in the gap flow.

Acknowledgments

This work has been funded by the European Community as part of the 6th Framework Project PROBAND n° AST4-CT-2005-012222.
The authors wish to thank E. Jondeau for his contribution to the measurements and data post-processing.

References

[1]Y. Rozenberg, M. Roger, A. Guédel & S. Moreau, Rotating Blade Self Noise: Experimental Validation of Analytical Models *AIAA-2007-3709, Proceedings of the 13th AIAA/CEAS Aeroacoustics Conference*, Rome, Italy, May 21–23, 2007.

[2]Bindon, J.P., The Measurement and Formation of Tip-Clearance Loss, *J. Turbomachinery*, Vol.111, pp. 257–263, 1989.

[3]Storer, J. A. & Cumpsty, N. A., Tip Leakage Flows in Axial Compressors, *Trans. ASME*, Vol.113, pp. 252–259, 1991.

[4]Muthanna C.,*Flowfield Downstream of a Compressor Cascade with Tip Leakage*, Ms Thesis, Faculty of the Virginia Polytechnic Insti- tute and State University, 1998.

[5]Tang, G., *Measurements of the Tip-gap Turbulent Flow Structure in a Low-speed Compressor Cascade*, Phd Thesis, Faculty of the Virginia Polytechnic Institute and State University, 2004.

[6]Intaratep, N.: *Formation and Development of the Tip Leakage Vortex in a Simulated Axial Compressor with Unsteady Inflow*, Phd Thesis, Faculty of the Virginia Polytechnic Institute and State University, 2006.

[7]Dunne, R.C. , Howe, M.S., Wall-bounded blade-tip vortex interaction noise, *Journal of Sound and Vibration*, Vol. 202, No.5, pp. 605–618, 1997.

[8]Ganz U.W., Patten T.J., Scharpf D.F., Joppa P.D.: *Boeing 18-inch fan rig broadband noise test*, NASA CR-1998-208704, 1998.

[9]Fukano, T., Takamatsu, Y., The effects of tip clearance on the noise of low-pressure axial and mixed flow fans, *J. Sound Vib.*, Vol. 105, pp. 291–308, 1986.

[10]Fukano, T., Jang, C., Tip clearance noise of axial flow fans operating at design and off-design condition, *J. Sound Vib.*, Vol. 275, pp. 1027–1050, 2004.

[11]Khourrami, M.R.,Choudari, M., A novel approach for reducing rotor tip-clearance induced noise in turbofan engines, *AIAA-paper No. 2001-2148*, 2001.

[12]Corsini, A.,Perugini, B., Rispoli, F. Sheard A.G., Kinghorn, I.R., Experimental and numerical investigation on passive devices for tip clearance induced noise reduction in axial flow fans, *7th European Conference on Turbomachinery - ECT-7, Athens, Greece*, March, 5–9, 2005.

[13]Roger M., Perennes S., Aerodynamic noise of a two-dimensional wing with high-lift devices, *AIAA paper No. 98-2338*, 1998.

[14]Arguillat B., *Etude experimentale et numerique de champs de pression parietale dans lespace des nombres donde, avec application aux vitrages automobiles*, Phd Thesis No. 2006 - 14, Ecole Centrale de Lyon, France, 2006.

[15]Vallette P. *Jet en ecoulement transversal : observations experimentales et numeriques*, Phd thesis - No. 98 - nan1 0277, 1988.

[16]Denton J.D. . Loss mechanisms in turbomachines, *Journal of Turbomachinery*, Vol. 115, pp. 621-656, 1993.

[17]Storer J. P. & Barton J. A., An investigation of the flow within the clearance space of a compressor blade tip, *ISABE 91-7013, Proceeding of the 10th International Symposium on Air Breathing Engines*, 1991.

EXPERIMENTAL STUDY OF A TIP LEAKAGE FLOW - PART TWO: WAVELET ANALYSIS OF WALL PRESSURE FLUCTUATIONS

Roberto Camussi* and Giovanni Caputi-Gennaro†
Mechanical and Industrial Engineering Dept. (DIMI), University 'Roma 3', Rome, I-00146, Italy

Marc C. Jacob‡ and Julien Grilliat§
Centre Acoustique du LMFA ,UMR CNRS 5509 – Ecole Centrale de Lyon – Université Claude-Bernard Lyon I, F-69134 Ecully Cedex, France

Advanced post-processing techniques based on the wavelet transform are applied to pressure signals measured at the surface of an instrumented airfoil installed within the anechoic wind tunnel available at the Laboratory of Fluid Mechanics and Acoustics of the Ecole Centrale de Lyon. Two flow configurations, with and without a variable gap at the airfoil tip, are investigated. The scope of the post-processing procedure is to extract the most energetic non-periodic contributions, localized in time and in space, and to detect the fluid dynamic structures which may act as noise sources. The events tracking method is based on the computation of time-frequency energy maps from which it is possible to select events, determine their time of appearance, and perform conditional averages. The conditioning procedure has shown that the amplitude of the oscillations of the averaged pressure signature becomes larger for increasing width of the gap, probably as an effect of a roll-up phenomenon occurring at the tip edge of the airfoil. In addition, the pressure-velocity cross analysis, including data obtained from PIV measurements, yielded the location of the major fluid dynamic structure statistically related to the largest pressure fluctuations at the wall.

Nomenclature

a	=	geometrical angle of attack
c	=	chord length
C_Ψ	=	dimensionless coefficient in the wavelet expansion
i	=	time index
f	=	frequency
p	=	pressure
r	=	resolution time scale
t	=	translation time
U_0	=	inflow speed
w	=	wavelet coefficients
x	=	distance from the leading edge (LE) in chord-wise direction
z	=	distance from the tip edge in span-wise direction
Ψ	=	mother wavelet function

I. Introduction

During the last decades, wavelet analysis has been extensively used to analyze random data obtained from both numerical simulations and experimental investigations conducted in turbulent flows. Comprehensive reviews

* Associate Professor, DIMI, University 'Roma 3', Via della Vasca Navale 79, Rome, I-00146, Italy.
† PhD Student, DIMI, University 'Roma 3', Via della Vasca Navale 79, Rome, I-00146, Italy.
‡ Assistent Professor, LMFA, Ecole Centrale de Lyon, 36 avenue Guy de Collongues, 69134 Ecully Cedex, France.
§PhD Student, LMFA, Ecole Centrale de Lyon, 36 avenue Guy de Collongues, 69134 Ecully Cedex, France.

about the wavelet theory and applications can be found in many reference papers or books (e.g. see among many ref. 1 and 2). Conditional sampling techniques based on the wavelet transform have been applied to turbulence data[3] and to pressure velocity measurements[4] in order to extract the most energetic contributions of the original signals. In the present work, a wavelet based post-processing methodology is applied to pressure and velocity data measured on an instrumented airfoil installed within the anechoic wind tunnel available at the Laboratory of Fluid Mechanics and Acoustics of the Ecole Centrale de Lyon. The purpose of the study is to investigate the physical nature of the cause of the largest pressure fluctuations on the airfoil surface for both a self noise configuration and a fan-tip with clearance configuration. To this aim, a convenient wavelet-based post-processing technique is applied to experimental data permitting us to extract the most energetic non-periodic contributions to the pressure fluctuations, localized in time and in space and hidden in the original chaotic signals.

A conditional average procedure based upon the wavelet analysis has been applied to both the wall-pressure and velocity data delivered by the experimental campaign, in order to recover the most probable shape of the most energetic pressure events detected over the airfoil surface and to obtain a statistical correlation between the flow dynamics (described by either single probe hot-wire anemometer and PIV measurements) and the largest wall pressure fluctuations (extracted from the wavelet treatment of single point pressure signals). A detailed description of the experimental apparatus, the measurements technique, the acquisition parameters and the flow conditions are given in part one of this paper (see Ref. 5). Here, we limit ourselves to describe the techniques adopted to analyze the experimental data and to present results which can be useful to better clarify physical mechanisms connected with the generation of the largest pressure fluctuations.

II. Experimental set-up

The experimental campaign was carried out in the anechoic tunnel of the Ecole Centrale de Lyon at a Mach number M ~ 0.2. Details on the experimental set up are given in Ref. 5 but, for the sake of clarity, the main features are briefly summarized in the following.

The airfoil was placed into an open-jet flow, which was limited in the span-wise direction by two flat plates. The gap between the lower plate and the airfoil tip was adjustable. A 5% camber thick (10%) airfoil was used in the experiment, that is a NACA 5510, with a 15° geometrical angle of attack as reference value. The chord was 200 mm and the span increased from 190 to 200 as the gap decreased from 10 to 0 mm.

The influence of various governing parameters was investigated in Ref. 5 by varying their values: the flow speed was increased from 20 to 90 m/s, the gap between the tip and the plate was varied from 0 to 10 mm and the angle of attack was varied between 0 and 18°. However here we concentrate mainly on two *reference configurations.* The former is a self-noise configuration (gap = 0) with the inflow speed U_0 and the angle of attack α set to 70 m/s and 15° respectively. In the following, it is referred to as the *no gap reference configuration.* The latter is characterized by a 10 mm gap width, again with U_0 = 70 m/s and α = 15°. In the following, it is denoted the *reference gap configuration.*

Unsteady pressure measurements on the airfoil, both in the mid-span region and in the gap region were combined with far field and single probe hot-wire anemometer (HWA) measurements. A special care was given to placing the pressure probes on the tip of the airfoil, on the two tip edges and on the plate facing the tip. Moreover, two sets of pressure probes were installed in the mid-span region both chord-wise and span-wise near the trailing edge.

Simultaneous PIV and single point pressure measurements were carried out both around the airfoil and in the gap region. Of particular interest here are the PIV-pressure data measured on the reference gap configuration. In this case, the measurement plane was located in the mid-gap plane (5 mm away from the tip edge of the airfoil) and the laser source was placed on the pressure side. Two near field pressure probes were placed on the airfoil tip along the mean line of the profile, at 6 and 155 mm far from the leading edge. A third pressure probe was placed in the far field, about 1 m away from the airfoil centre, on the suction side in the mid-span plane.

The measurements were divided into 10 acquisition series. During each acquisition, 60 PIV snapshots were taken at a frequency of 1 Hz (which means 60 s per acquisition), while the pressure signals were sampled at 20 kHz. This yields a total of 600 PIV snapshots and 10 pressure series resulting from the experimental measurements.

III. Wavelet analysis and the auto-conditioning method

The post-processing procedure adopted therein is based on the wavelet transform of the wall pressure signals. The scope of the procedure is to extract the most energetic non-periodic contributions, localized in time and in space. The choice of the wavelet technique is motivated by the fact that the wavelet decomposition, in spite of the Fourier transform, permits to represent a generic signal simultaneously in terms of a translation time (t) and a

resolution time scale (r), whose inverse corresponds to the frequency (f). The wavelet decomposition is accomplished by projecting the acquired signal over basis of compact support functions $\Psi(t)$, i.e. localized both in the time domain and in the transformed space. We note that in the Fourier decomposition the projection is performed over trigonometric functions, so that the physical information is spread over a theoretically infinitely extended time domain. Localized events are therefore missed by the Fourier decomposition while they are correctly retrieved by the wavelet transform through the representation of the signal over a two dimensional map in the time-frequency domain.

Formally, the wavelet transform of the signal $p(t)$ at the resolution time scale r is given by the following expression.

$$w(r,t) = C_{\Psi}^{-1/2} r^{-1/2} \int_{\infty}^{\infty} \Psi^{*}\left(\frac{t-\tau}{r}\right) p(\tau) d\tau \tag{1}$$

where $C_{\Psi}^{-1/2}$ denotes a coefficient which accounts for the mean value of $\Psi(t)$, and the integral represents a convolution between $p(t)$ and the dilated and translated complex conjugate counterpart of $\Psi(t)$.

The events tracking method is based on the computation of the so called Local Intermittency Measure[2] defined as:

$$LIM(r,t) = \frac{w(r,t)^2}{\left\langle w(r,t)^2 \right\rangle_t} \tag{2}$$

where the symbol $\left\langle \bullet \right\rangle_t$ denotes a time average. Fig. 1 shows an example of LIM distribution computed for a portion of pressure signal recorded at the wall. It is worth noting that the numerator of eq. (2), i.e. square of the wavelet coefficients, represents the localized counterpart of the standard Fourier spectrum that can be recovered by simple time integration. An example of the Fourier spectrum recovered from the square of the wavelet coefficients plotted against the standard Power spectrum is reported in Fig. 2a while Fig. 2b reports similar results obtained with different wavelet kernels, demonstrating that the choice of the wavelet type does not influence the achieved results. It has been also checked that the results are independent from the use of orthonormal discrete or continuous complex wavelets. Examples elucidating these comparisons are not presented here for the sake of brevity. In the following analyses, except for the case of PIV/pressure data, an orthogonal discrete wavelet expansion is performed on the pressure signals by using a Fast-Wavelet-Transform algorithm with the Battle-Lemarie Mother wavelet $\Psi(t)$.

Peaks of LIM represent large contribution of pressure variations to the overall SPL. Therefore the LIM amplitude at a selected scale r, can be thresholded in order to select events responsible for the largest pressure fluctuations and to determine how their appearance is distributed in time (see Fig. 3). Once the pressure events have been selected and well localized in the time domain, one may perform a conditional average of the original pressure signal. This auto-conditioning procedure leads to an ensemble averaged time signature of the fluctuating pressure, which represents the most probable shape of the most energetic structures which are hidden in the original chaotic signal. The wavelet transform is indeed needed to recover the phase of the events responsible for the largest pressure fluctuations at the wall. The phase is a random non-periodic and strongly non-Gaussian variable and the averaged pressure signature, whenever it is non-zero, helps to clarify the fluid dynamic origin of the selected events. The original method was introduced in Ref. 3 and successively applied to pressure signals and validated in Ref. 4 while applications to wall pressure data were presented in Ref. 6.

IV. Averaged cross-conditioned structures

As clarified in section II, velocity measurements using a single probe HWA have been conducted simultaneously to the wall pressure measurements in several configurations. Simultaneous PIV/pressure measurements have also been performed, in particular on the reference gap configuration. These experimental investigations provided useful data to perform a statistical analysis, which gives further clarifications on the physical nature of the fluid dynamic structures in the noise generation phenomenon. The conditioning method explained above has been applied to both the HWA/wall-pressure data and to the PIV/wall-pressure data, in order to extract aerodynamic events correlated to large localized pressure peaks at the wall of the airfoil.

In particular, once the pressure events have been selected and well localized in the time domain, the conditional average can be performed either on the single point velocity time series (HWA signals) or on the set of PIV snapshots available, provided that the velocity measurements are acquired simultaneously with the pressure signal analyzed. As a result, the outcome of the cross-conditional procedure analysis should be an averaged signature of velocity, representing the most probable fluid dynamic structure correlated to the pressure fluctuations at the wall of the airfoil.

V. Results

A. Auto-processing

The auto-conditioning method provides the wall-pressure averaged signatures in several position over the airfoil surface. In the no gap reference configuration, significant results are obtained only with the probes placed in the mid-span region. As clarified below, in this region the effect of the chord-wise position seems to be relevant.

An overall summary of results obtained considering probes located at mid-span (z = 0) for the no gap configuration is given in Fig. 4. It is shown that the shape of the averaged signatures significantly changes with the x/c parameter. The behavior obtained close to the leading edge seems to indicate that acoustic effects are dominant with respect to hydrodynamic perturbations. This is an expected result since in the LE region the boundary layer is very thin and not yet developed so that acoustic perturbations, generated by the impact of the incoming unsteady flow against the airfoil surface, are the main sources of noise.

When we move towards the trailing edge (TE), a different behavior is observed, as shown in the x/c=0.25 case of Fig. 4. Here a pressure drop is observed thus suggesting that, in a statistical sense, the pressure fluctuations are generated mostly by vortical structures passing close to the pressure probe position.

In the region close to the TE no significant results are obtained as an effect of the back-ground disturbance and the signal-to-noise ratio of the averaged pressure signatures is too low for any physical interpretations to be addressed.

No significant results are obtained also in the pressure side confirming that being the boundary layer very thin, the hydrodynamic perturbations induced by vortical structures are very weak and, from a statistical viewpoint, are uncoherent. An example of results obtained on the pressure side for the no gap reference configuration is given in Fig. 5.

The presence of a gap leads to pressure oscillations in the averaged signatures, as evidenced in Figs. 6-8 for the reference gap configuration. In Figs. 6 and 7 one may note that the oscillations are more pronounced close to the TE and at the edge of the airfoil in correspondence of the gap. Fig. 8 shows that the amplitude of the oscillating averaged pressure signature becomes larger for increasing width of the gap, with both the angle of attack and the inflow speed kept fixed at their reference values.

The observed behavior is due, probably, to vortex shedding from the side edge of the airfoil but, being such an effect not evident in the pressure power spectra, it has to be attributed to intermittent unsteady events which are not revealed when the signal is projected onto the Fourier basis. The physical nature of the observed phenomenon could be found into the mechanism of roll up of the vortical structures shed from the lower side of the airfoil and further insights would be inferred from the cross-analysis of the next sections.

B. Pointwise velocity/Pressure conditional statistics

As discussed in section II, simultaneous velocity/pressure measurements have been performed by placing a single hot wire probe close to the airfoil trailing edge at a mid-span location. The results obtained from the cross-conditioning procedure for both the reference configurations are presented. In Figs. 9 and 10 the averaged velocity signatures for the no gap reference configuration are depicted: the HWA signal has been conditioned by extracting the pressure events in several location along the trailing edge and in the mid-span region. A relevant pressure velocity correlation can be evidenced only close to the trailing edge at the mid-span location (x/c = 0.975; z = 0).

Then, considering the reference gap configuration, it is evident from Figs. 11 and 12 that no relevant gap effects occur in the mid-span region, whereas along the tip the presence of the gap increases considerably the pressure/velocity correlation and the shape of the velocity signature completely changes with respect to the one occurring in the mid-span region. The achieved results for the gap reference configuration are reported in Fig. 13 for different pressure probe positions. It is shown that moving along the tip, the phase of the signature changes. The non-zero time delay indicates that the fluid dynamic events (hot wire) associated to the emission of noise (pressure events) is not located spatially at the same position as the pressure probe. The location of the major fluid dynamic structure (which may act as a sound source) is upstream of the pressure taps. In fact, the phase delay increases as the distance between the pressure probe and the hot wire probe decreases. In account of the mean velocity and the

velocity of sound, the phase shift of the signatures can be converted into a spatial delay and the resulting position of the noise source, even though qualitatively, can be determined. The result reported in Fig. 14 show that such a location is upstream of the trailing edge at about x = 140 mm from the leading edge.

C. PIV/pressure conditional statistics

The joint analysis of PIV measurements (discussed in section II) and of single point pressure measurements is performed only for the reference gap configuration. On the basis of the HWA/pressure analysis presented above, we may expect the pressure signals recorded by the probe placed at x/c = 0.75 to provide the most useful data for the conditional PIV/pressure analyses. Thus, in the present investigation we concentrate primarily on this pressure signal that, once treated with the wavelet method, provides the set of instants from which the corresponding PIV velocity fields are selected.

Contrary to the previous cases, in the present analyses, the pressure signal is processed by using a continuous complex wavelets expansion, so as to achieve a more accurate time frequency resolution. Once the pressure events are extracted at the wall, the conditional analysis has been carried out by averaging together the PIV snapshots corresponding to the selected timing of the wall pressure events. The LIM threshold criterion can be restricted to specific frequency bands in order to select wavelets of a given scale. Examples are shown in Figs. 15 and 16 for both low and high frequency containing events. The corresponding flow patterns are identified with the method described above.

As stated in section II, 60 PIV snapshot are available from each 60 sec acquisition series. This represents a basic constraint to take into account, as it is evident that only some of the instantaneous velocity fields captured by these 60 snapshots could be selected. It should be noted that the analyzed pressure segments are centered on the time instants corresponding to the PIV acquisitions timing (see e.g. Figs. 15 and 16). Therefore, the selection of a PIV field occurs only when the LIM peak is located in correspondence of the origin of the time axis which results in a very small number of selected events.

The set of selected velocity fields are eventually averaged together leading to a non-zero averaged tip-flow structure which, should it exist, evidences the most probable fluid dynamic event responsible for the observed large pressure peaks. The selection procedure, applied to all the 10 acquisition series, provided a total of 119 pressure events. Furthermore, as shown on Figs. 15 and 16, the LIM peak frequency localization can vary from one case to another. Therefore a distinction has been also considered according to the frequency content of the pressure events (low or high frequencies). Among the 119 events selected, 18 presented a low-frequency behavior, whereas 75 were prevalently associated to high-frequency fluctuations. The remaining 31 fields evidenced events with a broadband frequency content.

The achieved ensemble averaged field corresponding to high frequency events is shown in Fig. 17. No relevant differences have been evidenced neither when no distinction between high and low frequency events is performed nor when the low-frequency events are considered. In the latter case a lower signal-to-noise ratio is documented due the limited number of samples selected. In any case, in the region upstream of the pressure probe position, thus very close to the region where the source was supposed to act, a non-zero fluid dynamic structure is revealed

The robustness of the results has been verified by the application of the averaging procedure considering the other pressure probe located in the upstream region of the airfoil (see section II). An example of the achieved averaged field is reported in Fig. 18 showing that the location of the resulting non-zero structure is consistent with the above presented results.

From the physical viewpoint, this event seems to consist of a motion of the fluid from the pressure side of the airfoil towards the suction side. Actually, since the PIV snapshots are taken in mid-gap plane the figure shows the corresponding 2D cut of the structure. One may assume such structure to be associated to a roll-up phenomenon occurring at the tip edge of the airfoil, but an exact interpretation can not be proposed unless a cross section analysis of the flow is performed.

VI. Conclusion

A detailed analysis of wall pressure and Hot Wire/PIV velocity data measured around an airfoil with and without a tip leakage, have been presented. The post-processing procedure was based on the application of the wavelet transform to the wall pressure data and the computation of conditional averages of both the pressure and the velocity data. In the self noise configurations, hydrodynamic wall pressure fluctuations have been shown to be mostly related

to the boundary layer separation on the suction side near the trailing edge. The presence of a gap leads to quite different behaviors since the most probable fluid dynamic event causing wall pressure peaks is found to be associated to a roll up phenomenon occurring around the tip at 50-60% the chord from the leading edge. The location of the source have been determined from the conditional analysis of the Hot Wire data leading to an averaged structure exhibiting a phase shift with respect to the pressure timing. This result has been definitely confirmed by the conditional analysis of the PIV fields providing a 2D view of the most probable wall pressure source.

Acknowledgments

This work has been funded by the European Community as part of the 6th Framework Project PROBAND n° AST4-CT-2005-012222. R.C. also acknowledge partial support from Italian Ministry of Education, University and Research under a grant PRIN (2005).

References

[1]Mallat, S., "A theory for multiresolution signal decomposition: the wavelet representation", *IEEE Trans.* PAMI 11, 1989, pp. 674,693.

[2]Farge, M., "Wavelet Transforms and their Applications to Turbulence," *Ann. Rev. Fluid Mech.*, Vol. 24, No. ??, 1992, pp. 395, 457.

[3]Camussi, R., Guj, G., "Orthonormal Wavelet Decomposition of Turbulent Flows: Intermittency and Coherent Structures," *Journal Fluid Mech.*, Vol. 348, 1997, pp. 177, 199.

[4]Guj, G., Carley, M., Camussi, R., Ragni, A., "Acoustic Identification of Coherent Structures in a Turbulent Jet," *Journal Sound Vibr.*, Vol. 259, 2003, pp. 1037, 1065.

[1]Jacob M. C., Grilliat, J., Camussi, R., Caputi-Gennaro, G., "Experimental study of a tip leakage flow – part one: aerodynamic and acoustic measurements", *AIAA paper submitted to 13th AIAA/CEAS Aeroacoustics Conference*, Rome, Italy, may 21-23, 2007.

[5]Camussi, R., Guj, G., Ragni, A., "Wall Pressure Fluctuations Induced by Turbulent Boundary Layers over Surface Discontinuities," *Journal Sound Vibr.*, Vol. 294, 2006, pp. 177, 204.

[6]Camussi, R., Guj, G., Di Marco, A., Ragni, A., "Propagation of Wall Pressure Perturbations in a Large Aspect-Ratio Shallow Cavity," *Exp. Fluids.*, Vol. 40, 2006, pp. 612, 620.

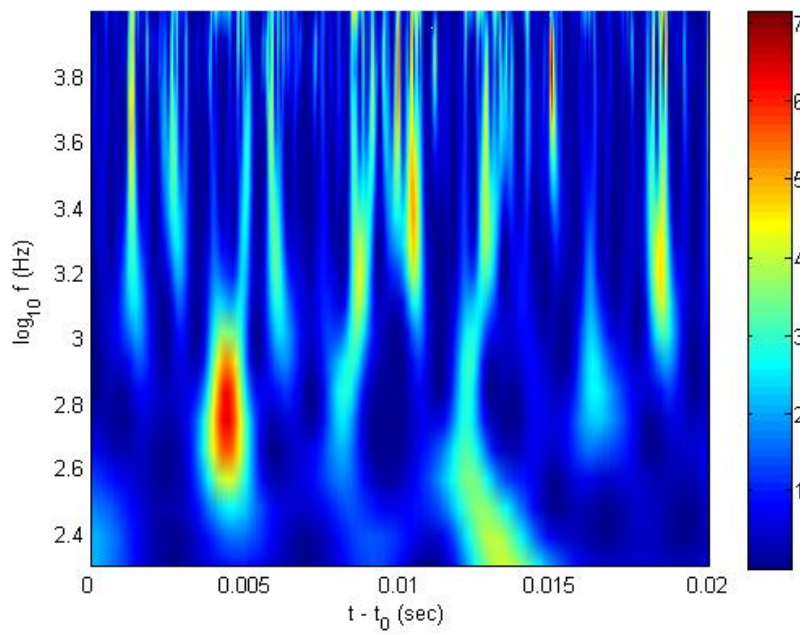

Figure 1. Example of LIM distribution computed for a portion of pressure signal recorded on the airfoil surface.

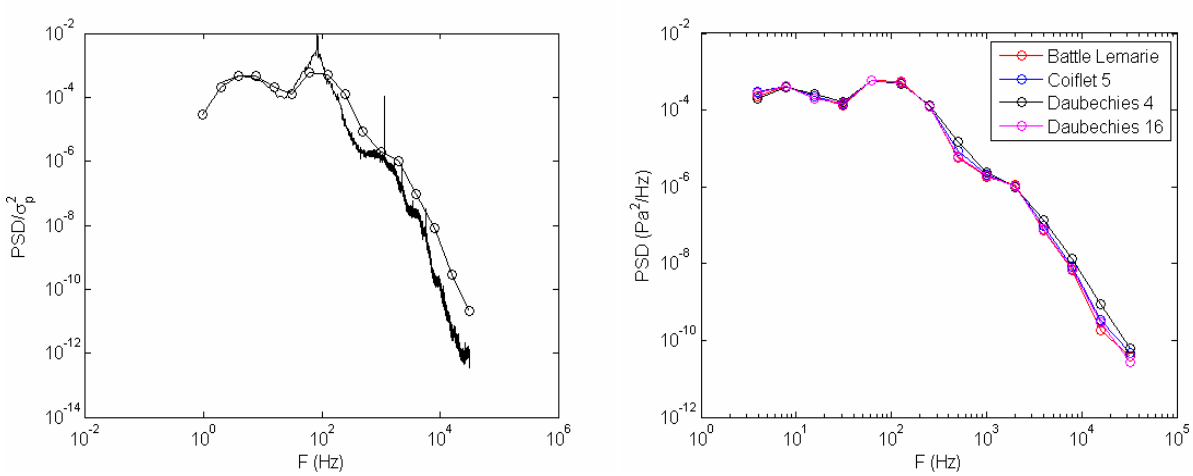

a) **b)**

Figure 2. Power spectrum obtained from the wavelet transform compared with a standard Fourier spectrum (a) and with results obtained adopting different types of mother wavelets (b).

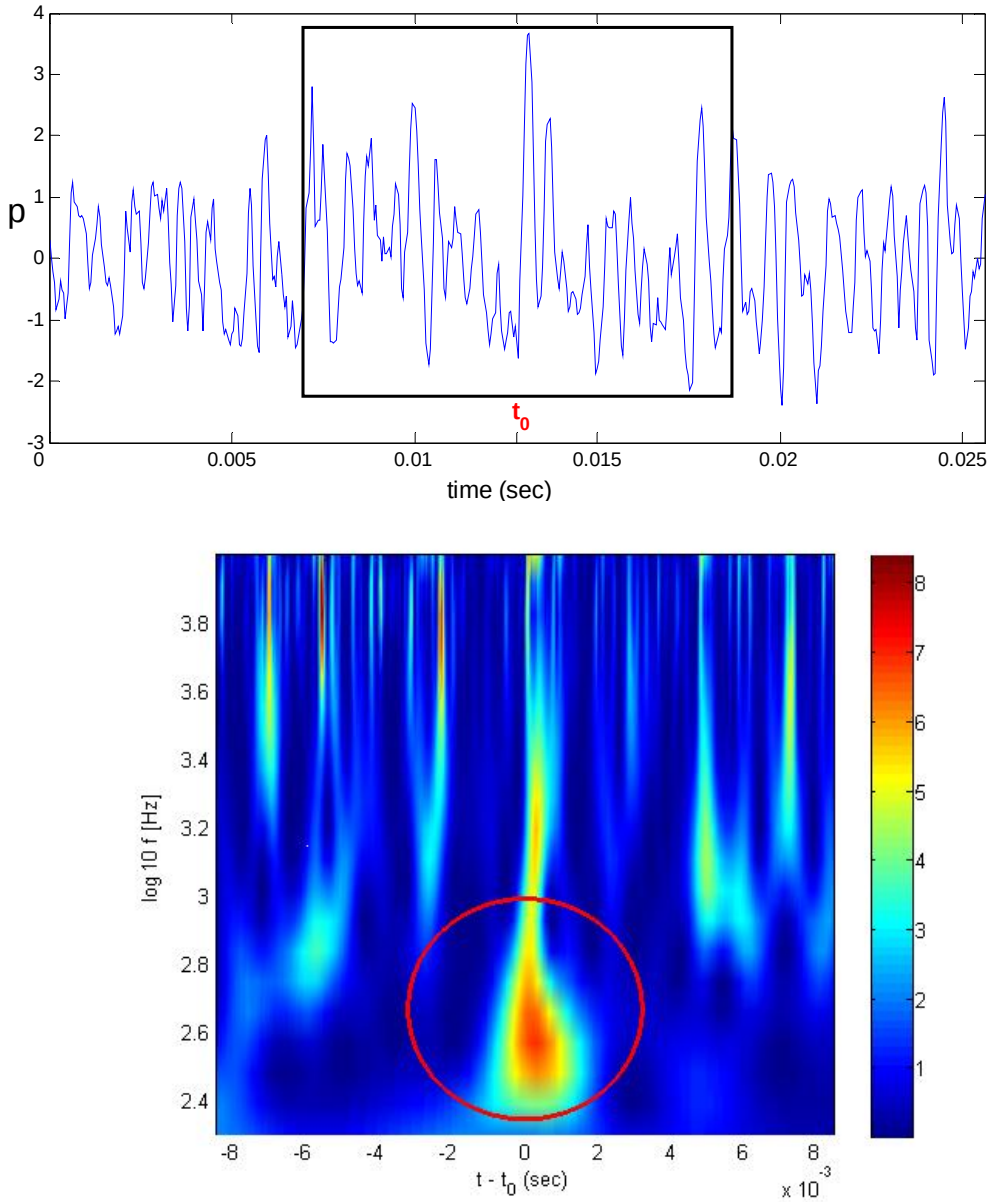

Figure 3. Selection procedure: the large value of LIM (red circle in the lower panel) indicates that an event occurs at the probe location in t = t0. Once the event is detected the portion of pressure signal centered in t0 is extracted to perform the conditional average.

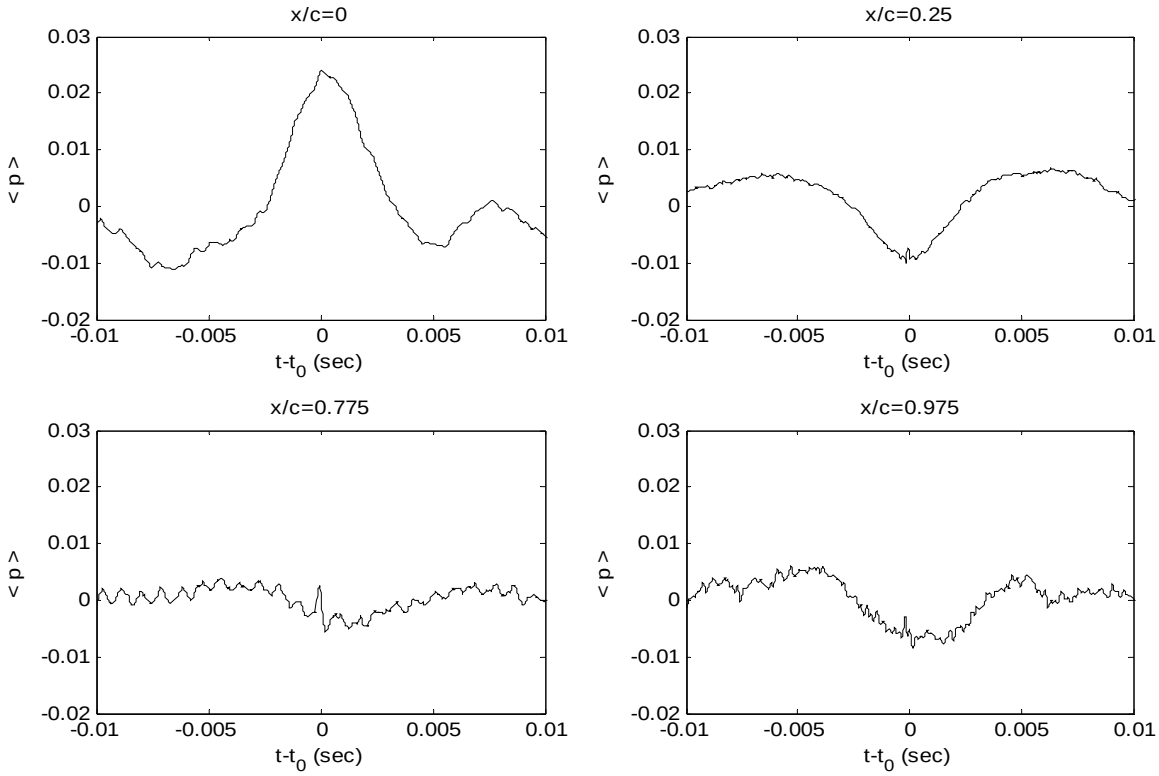

Figure 4. Averaged pressure time signatures obtained for several chord-wise positions at mid span for the no gap reference configuration.

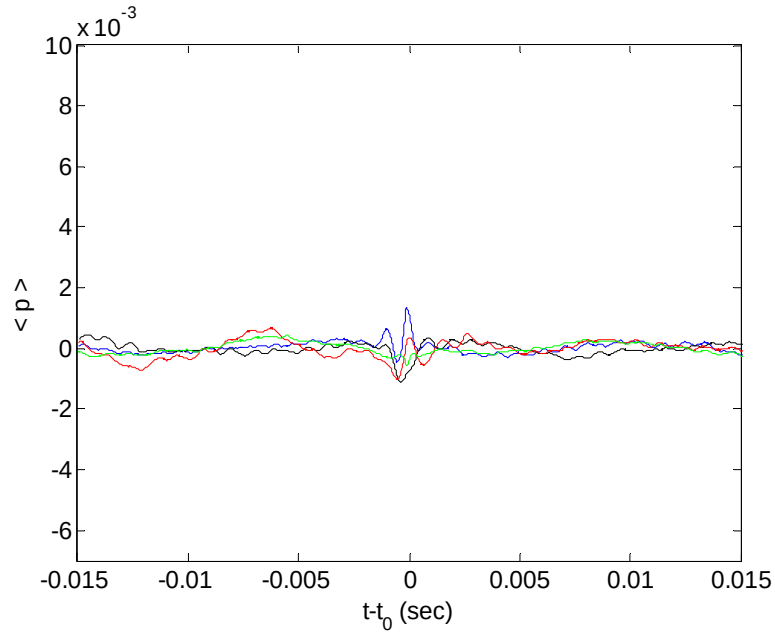

Figure 5. Examples of Averaged pressure time signatures obtained from several transducers in the pressure side of the airfoil for the no gap reference configuration.

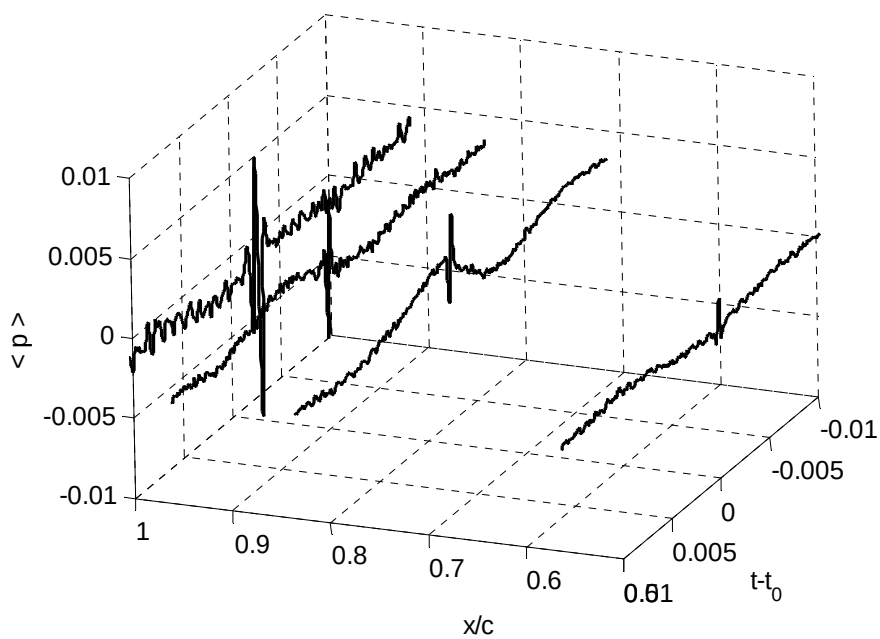

Figure 6. Averaged pressure time signatures obtained for several chord-wise positions in the tip region for the reference gap configuration.

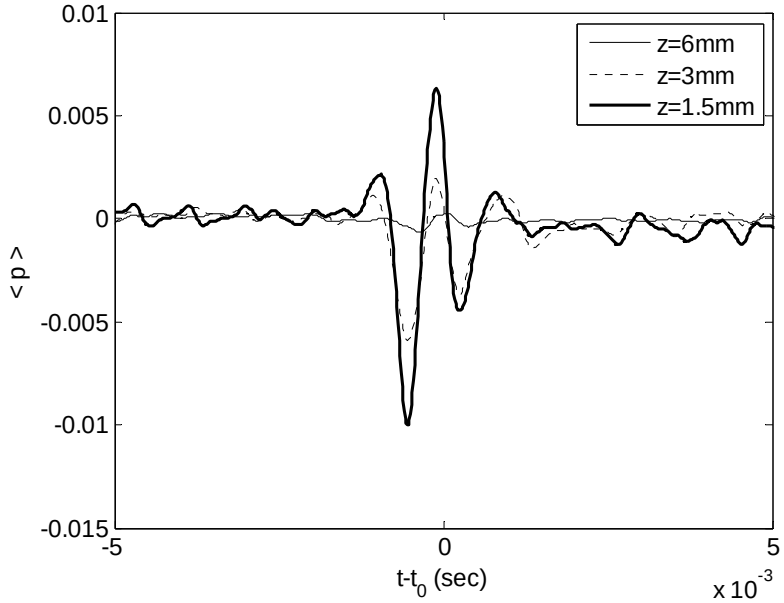

Figure 7. Averaged pressure time signatures obtained in the trailing edge region for the reference gap configuration: effect of the distance from the gap (z).

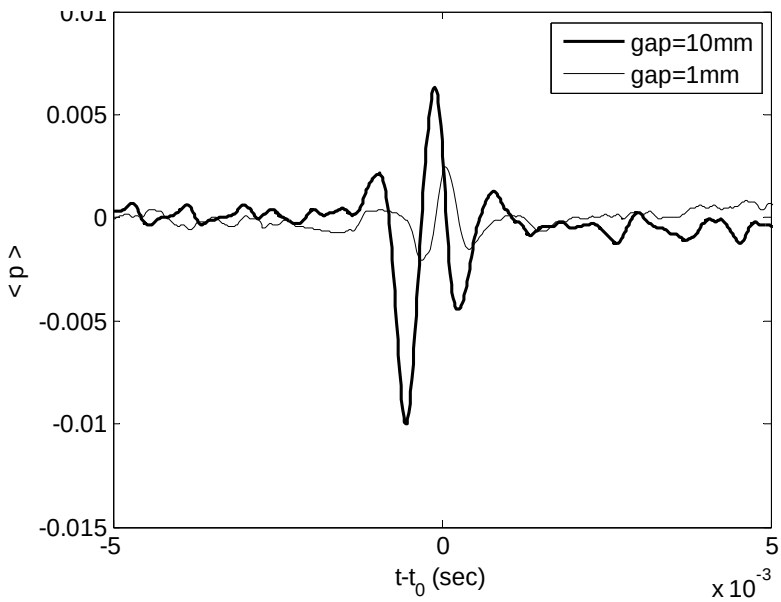

Figure 8. Averaged pressure time signatures obtained in the trailing edge region at the tip edge: effect of the gap width, with U_0 and α kept fixed at their reference values.

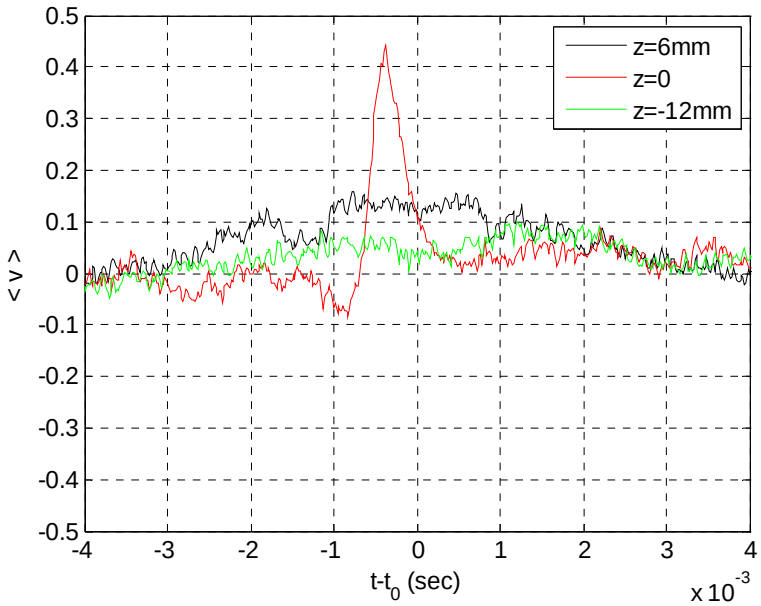

Figure 9. Pressure-velocity correlation in the trailing edge region for the no gap reference configuration.

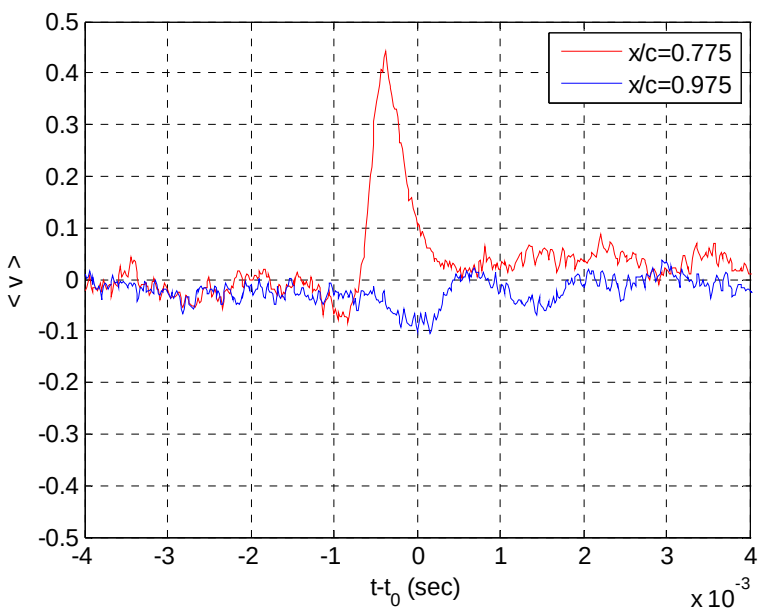

Figure 10. Pressure-velocity correlation in the mid-span region for the no gap reference configuration.

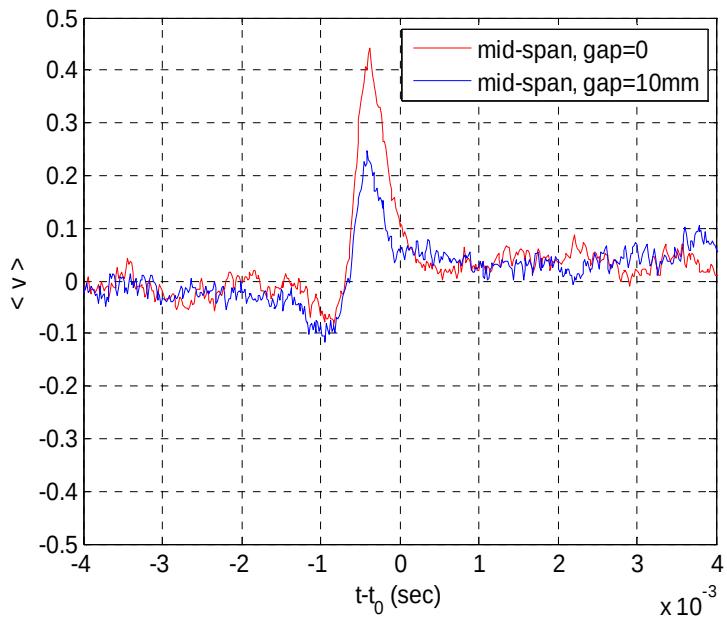

Figure 11. Pressure-velocity correlation in the mid-span region at the trailing edge (x/c = 0.975): effect of the gap.

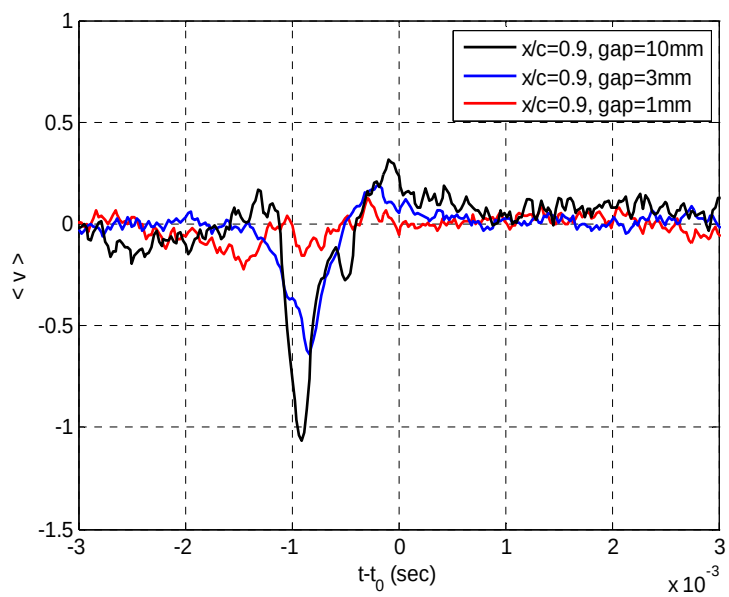

Figure 12.Pressure-velocity correlation in the tip edge region at the trailing edge (x/c = 0.975): effect of the gap.

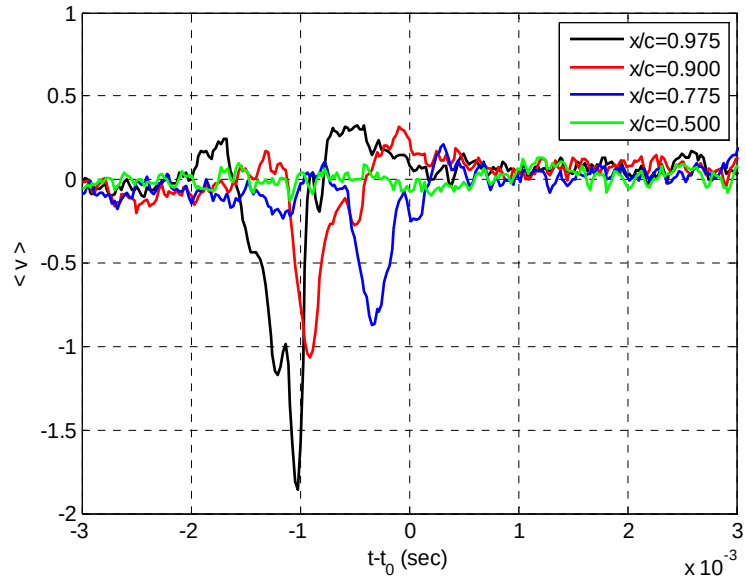

Figure 13. Pressure-velocity correlation in the tip edge region for the reference gap configuration.

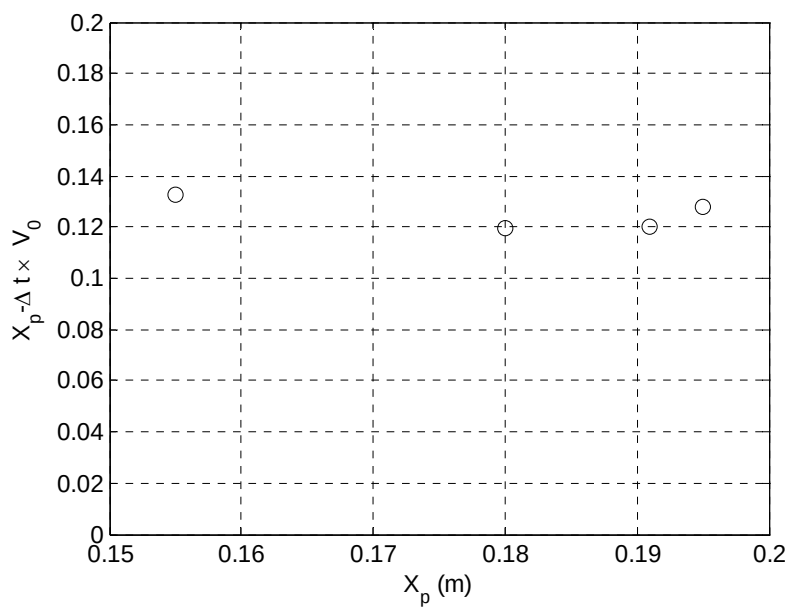

Figure 14. Reference gap configuration: spatial delay vs pressure tap position (Xp), computed by the time delay resulting from the pressure-velocity correlation in the tip region.

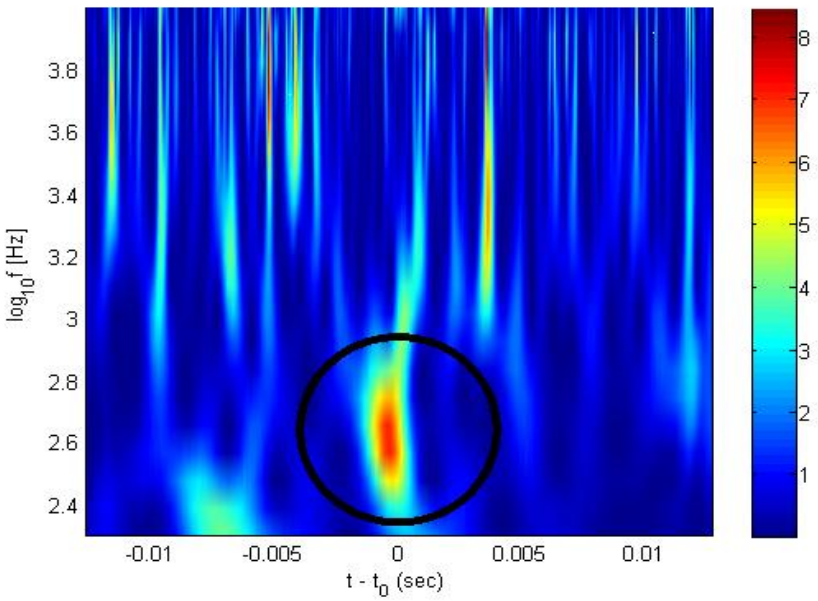

Figure 15. An example of a low-frequency pressure event (evidenced by the black circle) detected in the wavelet time-frequency domain from the pressure probe located at x/c = 0.75.

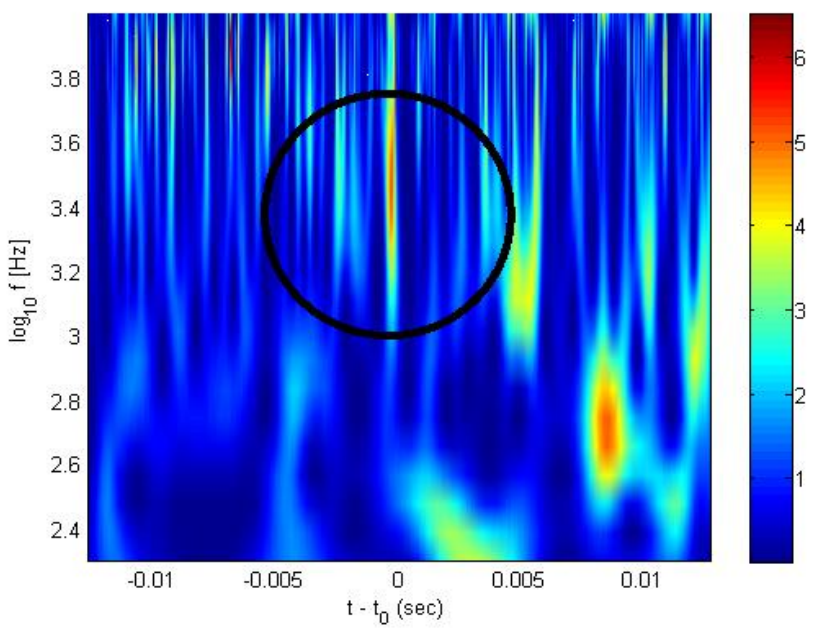

Figure 16. Same as previous plot but evidencing a high-frequency event.

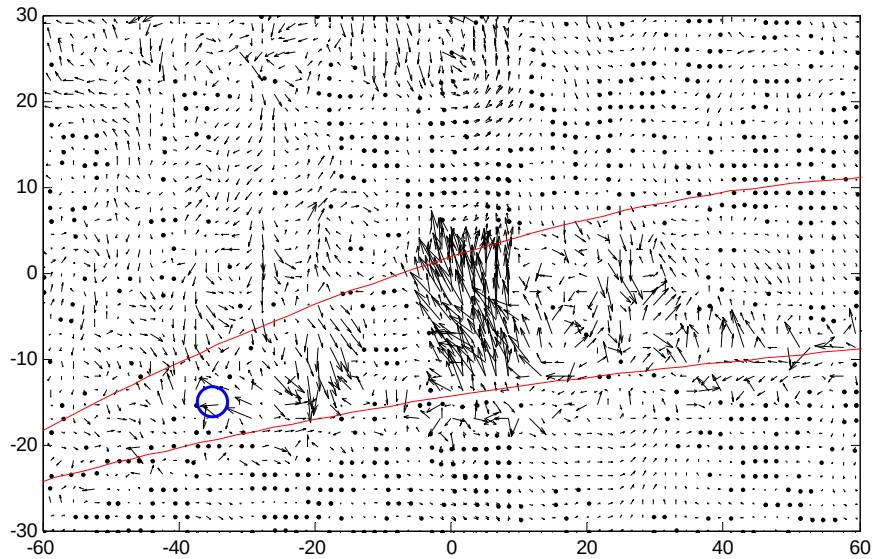

Figure 17. Averaged tip-flow field statistically related to the largest high-frequency pressure fluctuations on the wall. The blue circle denotes the pressure probe located at x/c = 0.75 and utilized in the conditioning procedure.

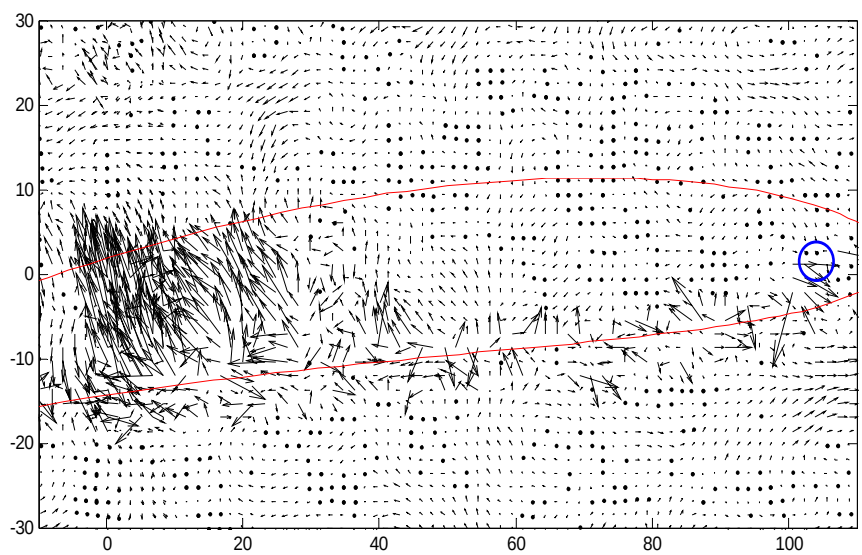

Figure 18. Same as previous plot but considering the wall pressure probe located at x/c = 0.075 (blue circle in the figure).

Bibliography

Abry, P., Fauve, S., Flandrin, P., Laroche, C. 1994 Analysis of pressure fluctuations in swirling turbulent flows. *Journal of Physics II* **4**, 725–733.

Amiet, R. K. 1976 Noise due to turbulent flow past a trailing edge. AIAA J., Vol. 38, pp. 2201-2209.

Arguillat, B. 2006 Etude expérimentale et numérique de champs de pression pariétale dans l'espace des nombres d'onde, avec application aux vitrages automobiles. Ph.D. thesis, Ecole Centrale de Lyon, Lyon

Batchelor, G. K. 1967 *An Introduction to Fluid Dynamics.* Cambridge University Press.

Benzi, R., Ciliberto, S., Tripiccione, R., Baudet, C., Massaioli, F., & Succi, S. 1993 Extended self-similarity in turbulent flows. *Phys. Rev.* E **48**, 29–32.

Bindon, J. P. 1989 The measurement and formation of tip–clearance loss. *J. Turbomachinery* **111**, 257–263.

Camussi, R. & Guj, G. 1997 Orthonormal wavelet decomposition of turbulent flows: intermittency and coherent structures. *J. Fluid Mech.* **348**, 177–199.

Camussi, R. & Verzicco, R. 2000 Anomalous scaling exponents and coherent structures in high Re uid turbulence. *Phys. Fluids* **12**, 676–687.

Camussi, R., Guj, G., Ragni, A. 2006 Wall pressure fluctuations induced by turbulent boundary layers over surface discontinuities. *J. Sound Vibr.* **294**, 177–204.

Caputi–Gennaro, G., Camussi, R., Iemma, U., & Morino, L. 2008 Power–spectral–density boundary–to–field transfer function. *14th AIAA/CEAS Aeroacoustic conference*, Vancouver, BC, Canada, AIAA 2008–3002.

Corsini, A., Perugini, B., Rispoli, F., Sheard A. G., & Kinghorn, I.R. 2005 Experimental and numerical investigation on passive devices for tip clearance induced noise reduction in axial ow fans. *7th European Conference on Turbomachinery*, Athens, Greece.

Douady, S., Couder, Y. & Brachet, P. 1991 Direct observation of the intermittency of intense vorticity filaments in turbulence. *Phys. Rev. Lett.* **67**, 983–986.

Dunne, R. C., Howe, M. S. 1997 Wall-bounded blade–tip vortex interaction noise. *J. Sound Vibr.* **202**, 605–618.

Farge, M. 1992 Wavelet transforms and their applications to turbulence. *Ann. Rev. Fluid Mech.* **24**, 395–457.

Ffowcs Williams, J. E., and Hall, L. H. 1970 Aerodynamic sound generation by turbulent flow in the vicinity of a scattering half-plane. J. Fluid Mechanics, Vol. 40, pp. 657-670.

Fukano, T. & Jang, C. M. 2004 Tip clearance noise of axial flow fans operating at design and off–design condition. *J. Sound Vibr.* **275**, 1027–1050.

Fukano, T., Takamatsu, Y. 1986 The effects of tip clearance on the noise of low–pressure axial and mixed flow fans. *J. Sound Vibr.* **105**, 291–308.

Ganz, U. W., Patten, T. J., Scharpf, D. F., Joppa, P. D. 1998 Boeing 18–inch fan rig broadband noise test. NASA CR–1998–208704.

Grilliat, J., Jondeau, E., Jacob, M. C. 2007 Aerodynamic and acoustic measurements of a tip leakage flow. *8th International Symposium on Experimental and Computational Aerothermodynamics of Internal Flows*, Lyon, France, ISAIF8–0086.

Guj, G., Carley, M., Camussi, R., Ragni, A. 2003 Acoustic identification of coherent structures in a turbulent jet. *J. Sound Vibr.* **259**, 1037–1065.

Intratep, N. 2006 Formation and development of the tip leakage vortex in a simulated axial compressor with unsteady inflow. Ph.D. thesis, Faculty of the Virginia Polytechnic Institute and State University, Blacksburg.

Jacob, M. C., Grilliat, J., Camussi, R., Caputi–Gennaro, G. 2007 Experimental study of a tip leakage flow — part one: aerodynamic and aeroacoustic measurements. *13th AIAA/CEAS Aeroacoustic conference*, Rome, Italy, AIAA 2007–3684.

Kambe, T. 1986 Acoustic emissions by vortex motions. *J. Fluid Mech.* **173**, 643–666.

Khourrami, M. R., Choudari, M. 2001 A novel approach for reducing rotor tip–clearance induced noise in turbofan engines. *7th AIAA/CEAS Aeroacoustic conference*, Maastrictht, Netherlands, AIAA 2001–2148.

Kress, R. 1989 *Linear Integral Equations.* Springer–Verlag, Berlin, Germany.

Lemmerman, L. A., and Sonnad, V. R. 1979 Three–Dimensional Viscous–Inviscid Coupling Using Surface Transpiration. J. Aircraft, Vol. 16, pp. 353-358.

Lighthill, M. J. 1952 On Sound Generated Aerodynamically. *Philosophical Transactions of the Royal Society*, London, Series A11, pp. 564–587.

Lighthill, M. J. 1958 On Displacement Thickness. J. Fluid Mechanics, Vol. 4, pp. 383-392.

Ma, R. 2003 Unsteady turbulence interaction in a tip leakage flow downstream of a simulated axial compressor rotor. Ph.D. thesis, Faculty of the Virginia Polytechnic Institute and State University, Blacksburg.

Mallat, S. 1989 A theory for multiresolution signal decomposition: the wavelet representation. *Trans. IEEE*: *PAMI* **11**, 674–693.

Wang, M., and Moin, P. 2000 Computation of trailing-edge flow and noise using large-eddy simulation. J. Sound and Vibration, Vol. 47, pp. 387- 393.

Morino, L. 1974 A General Theory of Compressible Potential Aerodynamics. NASA CR-2464.

Morino, L. 1985 Scalar/Vector–Potential Formulation for Compressible Viscous Unsteady Flows. NASA CR-3921.

Morino, L. 1986 Helmholtz Decomposition Revisited: Vorticity Generation and Trailing Edge Condition, Part 1: Incompressible Flows. Computational Mechanics, Vol. 1, No. 1, pp. 65-90.

Morino, L. 1990 Helmholtz and Poincaré Potential–Vorticity Decompositions for the Analysis of Unsteady Compressible Viscous Flows. In *P.K. Banerjee and L. Morino (Eds.)*, *Developments in Boundary Element Methods, Vol. 6: Boundary Element Methods in Nonlinear Fluid Dynamics*, Elsevier Applied Science Publishers, Barking, UK.

Morino, L. 2003 Is There a Difference Between Aeroacoustics and Aerodynamics? An Aeroelastician's Viewpoint. AIAA J., Vol. 41, No. 7, pp. 1209–1223.

Morino, L., and Bernardini, G. 2002 On the Vorticity Generated Sound for Moving Surfaces. Computational Mechanics, Vol. 28, No. 3–4, pp. 311–316.

Morino, L., Caputi Gennaro, G., Camussi, R., Iemma, U. 2007 On the vorticity generated sound: a transpiration-velocity/power-spectral-density approach. AIAA Paper 2007-3400, 13th AIAA/CEAS Aeroacoustics Conference, Roma, Italy, May 21–23, 2007.

Morino, L., Salvatore, F., and Gennaretti, M. 1999 A New Velocity Decomposition for Viscous Flows: Lighthill's Equivalent-Source Method Revisited," Computer Methods in Applied Mechanics and Engineering, Vol. 173, No. 3-4, pp. 317-336.

Muthanna, C. 1998 Flowfield downstream of a compressor cascade with tip leakage. M.S. thesis, Faculty of the Virginia Polytechnic Institute and State University, Blacksburg.

Powell, A. 1964 Theory of vortex sound. *Journal of the Acoustic Society of America* **36**, 177–195.

Roger, M., and Moreau, S. 2002 Trailing edge noise measurements and prediction for a subsonic loaded fan blade. AIAA–2022-2460.

Roger, M., Perennes, S. 1998 Aerodynamic noise of a two–dimensional wing with high–lift devices. *4th AIAA/CEAS Aeroacoustic Conference*, Toulouse, France, AIAA 1998–2338.

Rozenberg, Y., Roger, M., Guédel, A., Moreau, S. 2007 Rotating blade self noise: experimental validation of analytical models. *Proceedings of the 13th AIAA/CEAS Aeroacoustics Conference*, Rome, Italy, AIAA 2007–3709.

Saha, N. 1999 Gap size effect on low Reynolds number wind tunnel experiments. M.S. thesis, Faculty of the Virginia Polytechnic Institute and State University, Blacksburg.

Serrin, J. 1959 Mathematical Principles of Classical Fluid Mechanics. S. Flugge (Ed.), *Encyclopedia of Physics, VIII/1*, Springer–Verlag, Berlin, pp. 125-263.

She, Z. S., Jackson, E. & Orszag, S. A. 1991 Intermittent vortex structures in homogeneous isotropic turbulence. *Nature* **144**, 226–228.

Sokolnikoff, I. S. 1951 *Tensor Analysis: Theory and Applications*. Wiley, New York, NY.

Sokolnikoff, I. S., and Redheffer, R. M. 1966 *Mathematics of Physics and Modern Engineering*. II Ed., McGraw Hill, New York, NY.

Storer, J. A. & Cumpsty, N. A. 1991 Tip Leakage Flows in Axial Compressors. *Trans. ASME* **113**, 252–259.

Tang, G. 2004 Measurements of the tip–gap turbulent flow structure in a low–speed compressor cascade, Ph.D. thesis, Faculty of the Virginia Polytechnic Institute and State University, Blacksburg.

Vassilicos, J. C. 1996 Topological classification and identification of small-scale turbulence structures. In *Eddy Structure Identification* (ed. J. P. Bonnet), Springer.